Development of A 3D Bioprinted Model of Airway Smooth Muscle — A Novel Paradigm to Study Airway Mechanics in Asthma

By

Jeffery Osagie

A thesis submitted to the Faculty of Graduate Studies in partial fulfilment of the requirements of a degree in

MASTER OF SCIENCE

Department of Physiology & Pathophysiology

Rady Faculty of Health Sciences

University of Manitoba

To Patience Osagie…forever and always.

Table of Contents

List of Abbreviations iv

List of Figures vi

List of Tables viii

List of Equations viii

Acknowledgements ix

Originality Statement x

Abstract xi

Chapter one: Introduction ....

1.1 Literature review 1

1.2 Knowledge gap and Hypothesis 16

1.3 Specific objectives 17

Chapter two: Methodology ....

2.1 Cell culture 18

2.2 Alginate hydrogels 19

2.3 3D Bioprinting 20

2.4 Cell viability 24

2.5 Immunofluorescence 25

2.6 Contractile function 26

2.7 RNA isolation 28

2.8 Reverse transcription and gene amplification 30

2.9 Statistical analysis 32

Chapter three: Results — Optimization of bio-ink and 3D design ....

3.1 Cell selection 33
3.2 Alginate pre-screening and bio-ink optimization 34
3.3 Incorporating mechanical loads into 3D design 43

Chapter four: Results — Evaluating ASM contractile function in 3D ....

4.1 Baseline tension 53
4.2 Drug testing 55
4.3 Acellular load removal 58
4.4 RNA isolation 60
4.5 Phenotypic assessment 61

Chapter five: Discussions, Limitations and Conclusions ....

5.1 Discussion 65
5.2 Limitations and mitigations 70
5.2 Conclusions and significance 72

References 73
Appendix A: Statistical power analysis 98
Appendix B: RNA Isolation 99

List of Abbreviations

ACh	Acetylcholine
AHR	Airway Hyper-Responsiveness
ASM	Airway Smooth Muscle
CTAB	Cetyltrimethylammonium Bromide
Cyto D	Cytochalasin D
DCM	Decellularized Matrix
ECM	Extracellular Matrix
EDTA	Ethylenediaminetetraacetic Acid
FEV_1	Forced Expiratory Volume in 1 second
GAPDH	Glyceraldehyde 3-phosphate dehydrogenase
G	Guluronic acid subunit
HBSS	Hank's balanced salt solution
HEPES	4-(2-hydroxyethyl)-1-piperazineethanesulfonic acid
KCl	Potassium Chloride
LDH	Lactate Dehydrogenase
M	Mannuronic acid subunit
MW	Molecular weight
PBS	Phosphate buffered saline
RH	Relative Humidity
RGD	Arginine Glycine Aspartate
ROCK	Rho-Associated Protein Kinase
Sm-MHC	Smooth Muscle Myosin Heavy Chain

Sm-α-Actin	Smooth Muscle Alpha Actin
TGF-β	Transforming Growth Factor Beta
UBC	Ubiquitin C
YHWAZ	14-3-3 protein zeta/delta

List of Figures

Figure 1.01 Microfluidic printhead 14

Figure 2.01 Standard bio-ring design 21

Figure 2.02 Alginate dilution calculator 22

Figure 2.03 Representative image of ASM tissue at day 0 24

Figure 2.04 Alginate decrosslinking 28

Figure 3.01 Human ASM growth curves 33

Figure 3.02 Immunostaining of HASM cells seeded on thin AG-10 hydrogels 35

Figure 3.03 Immunostaining of HASM cells on thin alginates from Novamatrix 36

Figure 3.04 Microscopic features of HASM cells printed with AG-10 matrix 37

Figure 3.05 Macroscopic morphology of HASM printed using the AG-10 matrix 38

Figure 3.06 Acellular constructs printed using alginates from Novamatrix 39

Figure 3.07 Macroscopic morphology of HASM printed with 1% SLG-20 alginate 40

Figure 3.08 Microscopic features of HASM printed with 1% SLG-20 alginate 41

Figure 3.09 Temporal evolution of HASM printed with 0.75% alginate 42

Figure 3.10 Immunostaining of HASM printed with 0.75% alginate 43

Figure 3.11 HASM printed using the alternating ring design 44

Figure 3.12 Sandwich model 45

Figure 3.13 Temporal evolution of D12s in 3D sandwich 49

Figure 3.14 Cellular cytotoxicity 50

Figure 3.15 Cell viability 50

Figure 3.16 mRNA quantification of select genes in 3D vs 2D cultures 51

Figure 4.01 ASM tissues fabricated with varying acellular stiffnesses 54

Figure 4.02 Unstimulated contraction of constructs 55

Figure 4.03 Log concentration-response curve for acetylcholine 56

Figure 4.04 Contraction of day 6 ASM tissues 58

Figure 4.05 Acellular load removal.. 59

Figure 4.06 Summary of various RNA isolation techniques trialed 61

Figure 4.07 Comparison of relative mRNA abundance 64

List of Tables

Table 2.01 Characteristics of human airway smooth muscle cell lines used.................... 18

Table 2.02 Panel of alginates used... 20

Table 2.03 Approximate print pressures and speeds.. 23

Table 2.04 RNA isolation methods.. 29

Table 2.05 Primers used for qPCR gene expression analysis 31

Table 3.01 Cell doubling times 34

Table 3.02 Summary of various iterations of the 3D physical design 46

Table 3.03 Summary of tested cellular bio-ink components 47

Table 3.04 Summary of tested acellular bio-ink components 48

Table 4.01 Selection of housekeeping genes 62

List of Equations

Equation 2.01 Percent cytotoxicity 25

Equation 2.02 Lumen area reduction 26

Equation 2.03 Relative mRNA abundance... 31

Acknowledgements

First, I would like to extend my heartfelt gratitude to Dr. West, for taking a leap of faith and accepting to supervise a student with essentially no research experience from half-way across the world. Over the last four years, his indefatigable work ethic, seemingly boundless scientific knowledge, and top-notch mentorship has been nothing short of phenomenal. Thanks for your unwavering understanding, countless words of encouragement and the enormous freedom you granted me to flourish as an independent researcher and complete this project.

Next, I would like to thank members of the West lab; Emily, Sanjana, Xander and Neilloy, I will not be forgetting the genuine camaraderie and memories we created anytime soon — you guys are the best team members anyone could ask for. Special thanks to Emily, for her exceptional kindness and patience in teaching me essentially everything I know as a bench scientist. Words do no justice to how grateful I am for all the time and effort you put into this.

I would like to extend my appreciation to members of my thesis advisory committee for their expert insight and wise counsel right from the start. Thanks Dr. Keijzer for recommending that I read 'Made to Stick' by Chip and Dan Heath and that I take the Stanford 'Writing in the Sciences' course. Thanks to Dr. Mookherjee for her constructive feedback on my scientific knowledge and science communication skills, and to Dr. Halayko for all his mentorship advice and active contributions. These have undoubtedly made writing and completing this project somewhat less cumbersome and bringing me closer to achieving my dreams.

Thanks to Dr. Pascoe and members of the Biology of Breathing Research Trainee's hub at CHRIM for creating a fantastic support network and facilitating seminars and events that kept me informed on latest trends, while giving me a platform to practise my public speaking skills.

To my dear brother George, thanks a lot for being a shoulder I could lean on, all the advice on stoicism and helping me clear my head when I needed it most, I am sure mom would be proud.

Finally, thanks to all the funding agencies that contributed one way or another towards my completion of this degree. I would like to thank the University of Manitoba, Research Manitoba, the Manitoba Lung Association, the Canada Foundation for Innovation, the Natural Sciences and Engineering Research Council and Aspect Biosystems.

Originality Statement

This thesis is an original work. The following text, excluding references, was processed by the iThenticate plagiarism checking software with the following report results:

- 5% Similarity Index.
- 94 matches from 50 sources were detected.
- Each match contributed ≤1% similarity (7-178 words).

Abstract

Asthma is a chronic obstructive airway disease characterized by exaggerated contraction of airway smooth muscle (ASM) and structural changes that modify the mechanical properties of the airways. I hypothesized that 3D bioprinting technology can be used to construct a physiologically-relevant model, explicitly designed to simulate airway narrowing *in vitro*. Additionally, this model would be used to elucidate the consequences of altered mechanical loads on ASM contractile phenotype and function.

The ASM model consisted of a ring-shaped bundle of muscle constrained within a stiffness-modifiable acellular alginate support. ASM tissues bioprinted without acellular supports generated excessive baseline tension and rapidly lost structural integrity. The inclusion of acellular supports provided a mechanical preload that enabled baseline tone development, cellular organization, and muscle maturation. Contractility, assessed as a reduction in lumen area of constructs in response to various agonists, revealed differential contractile responses in ASM tissues fabricated across a stiffness range. Finally, although relative mRNA abundance of relevant contractile genes was modulated by structure, I was unable to detect statistically significant differences between the acellular stiffness groups tested.

These results suggest that a 3D bioprinted model of ASM represents a suitable platform to study changes in airway mechanics associated with asthma. The variable functional responses in ASM tissues fabricated with different acellular stiffnesses support that mechanical cues profoundly alter cellular function. Moving forward, the molecular effectors/mechanisms through which aberrant mechanical loads produce putative defects in ASM would be characterized, potentially unmasking novel therapeutic strategies to manage disease progression in asthma.

Chapter one: Introduction

1.1 Literature review

Pathophysiology of asthma

Asthma is the most common chronic obstructive respiratory disease and the leading cause of hospitalization in children and young adults in Canada (1). It affects an estimated 5 – 10% of the population in many developed countries and up to 300 million people worldwide (2,3). Asthma represents a large socio-economic burden, is associated with poor quality of life, and high risk of comorbidities and disability in affected people (4). Yet despite significant research, our understanding of the nature of asthma is still limited, with many researchers declaring it a syndrome rather than a disease. Patients often exhibit a range of phenotypes/endotypes, including differences in clinical markers and responses to therapy, such that it remains under-diagnosed and poorly treated in a significant amount of people (5–8). As the prevalence of asthma is currently increasing by up to 50% every decade (9), an improved understanding of the underlying causal mechanisms is essential to potentially personalize therapies and alleviate the associated burden.

The principal functional abnormality in asthma is an excessive, but partially reversible, closure of the airways in response to a wide range of irritants or contractile agonists, termed airway hyper-responsiveness (AHR) (10). AHR presents clinically as an increase in airway sensitivity and resistance, which causes the recurrent and variable symptomatic episodes of wheezing, dyspnea, chest tightness and coughing (11). AHR is most definitively diagnosed by PC_{20} testing, which involves measuring the concentration of an inhaled bronchoconstrictor required to reduce the forced expiratory volume in 1 second (FEV_1) by 20% (12). While AHR has been identified in other diseases including chronic obstructive bronchitis (13) and cystic fibrosis (14), PC_{20} is widely used as a conclusive diagnostic screener in patients with a high pre-test probability score for asthma. This is because PC_{20} inversely correlates with disease severity (15) and has a high negative predictive value for asthma (16). While the main effector of excessive airway narrowing is an abnormal contraction of airway smooth muscle (ASM), and most features of AHR could be brought about by alterations in normal muscle mechanics [manifesting either as an increase in force generation (17), shortening velocity (18) or contractile sensitivity (19)], the pathogenesis of AHR remains unclear. As the heterogenous nature of the disease suggests, it could potentially include complex interactions between genetic and environmental factors, as well as neural or inflammatory pathways and/or other components of airway tissue.

Early observations have suggested that exposure to pro-inflammatory agents, including allergens and other environmental stimuli, could trigger irreversible changes in airway structure and ultimately lead to development of AHR in patients with or without asthma (16–18). This led to the prevailing view that the disease is initiated as an allergic disorder. Chronic inflammation is believed to alter airway function by shifting the immune system towards a T helper type 2 (Th2) immune response, inducing the release and activation of several immune mediators including interleukins IL-3, IL-4, IL-5, and IL-13. These subsequently signal the production of immunoglobulins (specifically, IgE) from plasma cells, as well as perpetuating recruitment of eosinophils to the airways (20,21).

Although abnormal immune responses are indisputably a hallmark of asthma, a growing body of literature has identified interactions between multiple and complex pathogenic mechanisms that are not necessarily or uniquely related to airway inflammation (22). For instance, anti-IgE therapy has been shown to reduce inflammation without changing AHR in asthmatic patients (23). Evidence suggests most mild and moderate asthmatics do not have airway eosinophilic infiltration (24) and even when eosinophils are present, anti-IL-5 therapy can greatly diminish eosinophilic recruitment without altering AHR (25). Similarly, allergen-challenged $Cav1^{-/-}$ mice had an increase in AHR greater than their wild type counterparts, which was largely independent of lung inflammation (26). Further, while mouse models of allergic inflammation have identified several cytokines and their downstream targets as key mediators in the inflammatory process, drugs interfering with these pathways have yet to completely reverse AHR clinically in humans (27–29). Finally, the compressive mechanical forces resulting from repeated bronchoconstriction in asthmatic patients was sufficient to induce airway remodeling without additional inflammation (30). Subsequently, mathematical models have found spatial correlations in altered airway structure due to repeated cycles of bronchoconstriction (31). Such findings suggest that excessive airway narrowing associated with asthma may be initiated as a result of inflammatory-independent or synergistic mechanisms that become self-sustaining, even after the underlying immune dysfunction has been managed.

Interestingly, changes in airway structure persist significantly longer than inflammation and have been documented in all degrees of asthma severity in both large and small airways (32–34). These structural changes, which are collectively referred to as airway wall remodeling, include altered tight junction formation in airway epithelial cells (35), muco-ciliary dysfunction (36), angiogenesis in bronchial mucosa (37), hypertrophy and hyperplasia of ASM (38), and increased thickening of airway adventitia, lamina propria and subepithelial basement membrane layers (39), caused by an elevated deposition of extracellular matrix (ECM) proteins and proteoglycans (40,41). Intriguingly, there is strong evidence that these architectural changes originate during prenatal development (42) and precede clinical symptoms of the disease (43). While the complete pathophysiological consequences are still unclear, airway wall remodelling is associated with reduced lung compliance (44,45), which alone could result in the development of AHR by altering the balance of forces between the lung ECM and airways.

In vivo, airway calibre is regulated as a delicate balance between contractile forces generated by ASM to close the airway, the pressure differential across the airway wall, and non-muscle elements in the airways. Force generation and shortening of ASM, which circumferentially surrounds and comprises a significant portion of the airway wall, is considered the main effector of acute airway narrowing (46). *In vitro*, maximally stimulated ASM can shorten to less than 25% of its initial length if there is no opposing mechanical load (47). *In vivo*, an equivalent contraction would result in the complete occlusion of many large and small airways and a near complete loss of airflow, since the Hagen–Poiseuille equation shows airflow is inversely proportional to the fourth power of airway luminal radius (48). Non-muscle elements in the lungs that oppose ASM shortening, and airway closure include the bulk modulus (a measure of the elasticity of lung and airway tissues), tissues within the bounds of the muscle that becomes compressed, as well as the outward physical tethering of lung parenchymal elements through elastic fibres to the airways (49).

In the normal lung, physical tethering creates an effective pressure that acts against ASM narrowing and airway compression, by imposing a mechanical preload on the muscle and transmitting the elastic recoil of parenchymal elements to the airways. However, in asthmatic airways, based on the nature of airway remodeling-induced structural deformations, the elasticity of the airways and parenchymal tethering forces may be decreased (50,51). Since airway patency is so easily and dramatically affected by these non-muscle pulling forces, it was originally believed that stiffer airways would disrupt the balance of forces, allowing the muscle to shorten much more than normal (52,53). Nevertheless, several studies have argued that altered mechanical loads could be beneficial, and remodeled airways may protect against exaggerated ASM shortening (54,55), although a lack of consistent findings makes this hypothesis problematic (56). On the other hand, repeated force generation in the asthmatic ASM layer may also play a major role in altering airway mechanics with or without structural remodeling (57). Contractile activation of ASM increased the stiffness of sheep (58) and human airways (59), which subsequently blunted the beneficial effects of ASM strain on airway relaxation.

While there is still no consensus on the effects of specific structural alterations in the airways, it is clear that neither inflammation nor the bulk mechanical properties of the airways can explain all asthma endotypes/phenotypes and pathogenic mechanisms. Recent insights into ASM contractile activities using computational modelling reveal mechanical cues could induce changes in cellular signalling through 'exquisitely mechano-sensitive' pathways (60).

Cellular mechano-transduction

It has long been understood that soluble biochemical signals can affect cellular function. More recently, the notion that cells can sense and respond to physical forces and mechanical cues from their micro-environment, termed mechano-transduction, has been gaining an increasing amount of traction. Since the nature of mechanical forces and cellular responses can vary substantially between tissues, mechano-transduction is now largely viewed as a combination of two central paradigms: 1) passive or 'outside-in' signalling and 2) active or 'inside-out' signalling. Outside-in sensing involves cells responding to external forces including shear stress (61) and extension/compression (62), while inside-out sensing comprises the generation of internal traction forces that allow for a cell to evaluate the physical properties of the ECM, including geometry (63), ligand density (64) and stiffness gradients (65). Despite sometimes being viewed as separate processes, both outside-in and inside-out signalling operate through closely intertwined pathways involving sensing elements that physically couple the external physical environment with the underlying cytoskeleton.

The cytoskeleton is comprised of a network of actin filaments, microtubules and intermediate filaments (mostly vimentin, desmin, and lamin in ASM), which are the main loadbearing cellular structures involved in regulating bi-directional mechano-transduction signals (66,67). This highly dynamic filament network extends throughout the entire cell, acting as a physical link between organelles, which in turn are mechanically tethered to adhesion sites on the ECM. These ‘focal adhesions’ consist of clusters of transmembrane integrin receptors and clusters of adapter proteins (e.g., catenins, talin, paxillin, zyxin and vinculin) that link the intracellular and extracellular environment (68). The arrangement of these filaments is adaptive, such that changes in the mechanical milieu can cause dynamic assembly and/or disassembly of cytoskeletal elements, allowing the cytoskeleton to transit through different phases in the absence of a biochemical reaction (69). Given the high interconnectivity and plastic nature of the cytoskeletal filaments, any small rearrangement or deformation of the ECM will inevitably and rapidly lead to a morphologic change in nearly every aspect of the intracellular structure, which can in-turn regulate a diverse range of cellular processes. Pioneering work by Pelham and Wang using fibroblasts and kidney epithelial cells grown on collagen-coated polyacrylamide hydrogels allowed the mechanical micro-environment to be tuned while maintaining a constant chemical environment. These studies revealed a high propensity for cells grown on rigid substrates to develop high motility and lamellipodial activity, increasing cell spreading and adherence (70). Subsequent studies have highlighted vital roles played by physical forces in regulating a vast range of cellular activities, including altering enzyme kinetics (71), phosphorylation/unfolding of proteins (72) and arrangement of DNA within the nucleus (73). These impacts of the mechanical micro-environment on cell biology can be incredibly profound. Substrate stiffness and matrix porosity were found to drive differentiation of mesenchymal stem cells into different lineages (soft, neurogenic; moderately stiff, myogenic; stiff, osteogenic). Importantly, the mechanical signalling was capable of over-riding the effects of traditional soluble biochemical signalling pathways (74,75).

While disruptions to normal lung mechanics can profoundly alter the physiology of all lung cell types, airway myocytes show a particularly pronounced and complex mechanical responsiveness that has recently been identified as a potentially major player in the pathogenesis of asthma. Applying acute (within 2 hours) and chronic (within 11 days) mechanical stresses to ASM cells grown on collagen-coated flexible membranes revealed pro-contractile changes (76). In response to a single uniaxial stretch (3s), ASM cells cultured on an elastic silicone membrane showed a transient increase in intracellular calcium concentration that was largely independent of intracellular messenger production (77). Previous work by Dr. West and colleagues demonstrated an acute increase in substrate stiffness can elevate baseline ASM stiffness, while chronically high stiffness increased contractile protein content and contractile responses to potassium chloride (78). Similar studies revealed changes in ECM stiffness can alter cell-cell coupling (79), proliferative and secretory functions (80) in ASM tissue from the lungs of otherwise healthy participants. The concept of mechanical plasticity suggests the muscle responds to different mechanical loads by reorganizing its contractile and cytoskeletal machinery and/or differentially expressing a repertoire of contractile genes or proteins [including myosin heavy chain (MHC), alpha-actin (-α-actin) and desmin (81)]. This allows the force generating structures to adapt and contract with maximum force over a large length range (82).

These findings clearly demonstrate the crucial role mechanical signals play in regulating numerous aspects of ASM function. But such studies have yet to elucidate the specific molecular sensors or transducers through which the cascade of events from mechanical stimulation to cellular response occurs. For example, mathematical modelling of the airway wall as a nonlinear fibre-reinforced elastic cylinder (83), demonstrates a theoretical synergistic pathway between mechanical forces and biochemical signalling. Where this occurs, repeated ASM contractile activation increases mechanical stresses in the airway wall, which subsequently drives activation of latent pro-mitogenic and pro-contractile cytokines. Specifically, through transmembrane integrin receptors (especially α5β5), strain-induced reorganization of ASM cytoskeletal filaments results in the activation of latent transforming growth factor beta (TGF-β) complexes in the ECM. In turn, activated TGF-β can act as a contractile agonist (84), increase ASM proliferation [through phosphorylation of MAP kinases (85) as well as ERK, JNK and p38 (86)] or activate the small G protein $G_{\alpha q/11}$, RhoA and ROCK (87). These multiple signalling intermediates may augment force production and contractility in ASM by facilitating actin polymerization via N-WASP and $Arp_{2/3}$, as well as through ROCK, mDia1/profilin and calponin phosphorylation pathways. ROCK further promotes MLC_{20} phosphorylation, which maintains cycling of actomyosin cross-bridges. Collectively, this enhanced force production may contribute to a mechanically modulated positive feedback loop (57).

Such observations on ASM mechano-transduction have mostly been limited by the experimental techniques that are available to impose and measure mechanical stimulation at the single cell or tissue levels. Thus, inferences about the precise effects/effectors of varying mechanical cues rests in part on century-old studies and theoretical models that remain inadequately characterized. Discerning the specific effects of structural changes induced by airway remodeling requires reliable and high throughput models explicitly designed to study the mechanical properties of tissues, while simultaneously allowing for direct assessment of tension development in ASM (88). This is particularly relevant to asthma, where mechanical and contractile dysfunction are major contributors to disease pathogenesis.

Existing models for studying ASM in asthma

Due to ethical and logistic limitations only a handful of studies have assessed functional properties of ASM using viable human asthmatic tissue, and even fewer have investigated key mechano-transduction pathways (89,90). This has prompted researchers to turn to animal models, which have contributed substantially to our knowledge about some mechanisms underpinning ASM contractile dysfunction in asthmatic airways. While a variety of species have been used to study ASM in asthma, including rats, cats, dogs, guinea pigs, horses, and primates, by far the most used is the mouse model of allergic airway inflammation. This is mainly due to practical reasons including high reproductive rates, low maintenance costs and availability of tools to study disease pathogenesis and contractile mechanisms (91). In these models, mice are administered an inhaled allergen over acute (<2 weeks) or chronic time periods (>6 weeks) to induce an asthma like phenotype. This typically involves a Th2 immune response reminiscent of human allergic asthma and airway hyper-responsiveness to inhaled bronchoconstrictors. In chronic exposure models, mice display many signs of airway wall remodelling including ASM hyperplasia and hypertrophy, epithelial metaplasia, goblet cell hyperplasia and ECM deposition (92). However, due to genetic and physiologic differences between species, these models invariably lack elements that limit their ability to adequately replicate human disease. Aside from differences in lung size and respiratory rates, these models are only capable of simulating the allergic presentation of human asthma, which may be less relevant for other endotypes/phenotypes of the disease (93). This is further complicated by the fact that the observed airway dysfunction, including the inflammatory and structural aspects, typically begin to recover soon after the cessation of allergen exposure (94,95).

Two-dimensional (2D) culture models using ASM cells grown as monolayers on hard plastic or glass substrates are commonly used to study the molecular and cellular mechanisms modulating ASM contraction. The cells are usually isolated by enzymatic or mechanical digestion of freshly excised pulmonary tissues obtained from patients undergoing surgical procedures or from animal models. After isolation, cells can either be virally transfected to form stable cell lines or used directly as primary cultures (96,97). Several studies using flat 2D culture plastics coated with matrix proteins have reported that the ECM is capable of differentially regulating various aspects of ASM function, including maturation (98), contractility (99), proliferation and phenotypic modulation (100). However, the biological relevance of results obtained using an artificial 2D geometry are somewhat questionable, as cells *in vivo* exist as part of a complex three-dimensional (3D) network, receiving mechanical cues along three axes. By removing cells from the remodelled asthmatic airway, these physical cues are lost. To buttress the role of dimensionality and altered mechanical environment, numerous studies have demonstrated the crucial effects that micro-geometries exert on cellular function, including regulating cytoskeletal structure (101,102). Specifically, substrate geometry was shown to differentially modulate ASM proliferation and organization when seeded in high serum media (103). Finally, manipulating mechanical environments in 2D presents technical difficulties, as plastic substrates are extremely stiff, and tuning the stiffness to simulate healthy or diseased airways may be especially herculean.

Isolated ASM strips or rings attached to force transducers in an organ bath provide a way to measure muscle contraction and mechanics specifically in a 3D environment. ASM strips are typically prepared by removing the connective tissue and mucosa layers from the airways of ‘asthmatic’ animal models or naïve animals through microdissection (104). The key advantage of these models is that they provide a way to directly assess indices of ASM contraction without the modulating impact of confounding variables such as the interaction between multiple cell types and mediators. Remarkably, increased airway wall stiffening achieved by photo-crosslinking collagen fibres of freshly dissected bovine bronchial airway rings using riboflavin (vitamin B2) and Ultraviolet-A radiation, was sufficient to cause ASM to contract at a faster rate and to a greater degree when exposed to contractile agonists (105). However, the biological or disease relevance of ASM strips is still unclear. Since the ASM bundle has been uncoupled from mechanical elements in the normal airway wall, ASM strips fail to recreate vital features like parenchymal tethering, the bulk of the airway wall, and the integrated response between multiple cell types. Thomson *et al.*, were unable to detect any significant relationship between *in vivo* airway responsiveness and *in vitro* ASM sensitivity to methacholine, demonstrating an important role for non-muscle factors (106). Thus, the oversimplified mechanical environment provided by ASM strips might be insufficient to unmask vital disease mechanisms.

Precision Cut Lung Slices (PCLS) offer a potential solution to circumvent many of the constraints with 2D models and ASM strips, since they faithfully preserve cell type diversity, architecture, and mechanical microenvironment of native airways. In these models, lungs are gently inflated with a liquid agarose solution followed by precise transverse cutting (100 — 300 µm thick sections) to visualise airway lumens (107–109). Lung slices can be generated from human tissue or animal models and have been shown to retain viability and structural integrity for up to 14 days in culture (110). Meurs *et al.,* used PCLS isolated from guinea pigs and patients with COPD to demonstrate a reduction in parenchymal retraction forces and biomechanical changes in the airway wall could contribute to the development of AHR in small airways (111). In a related study, challenging mouse PCLS with methacholine revealed a variable increase in compressive circumferential strain in parenchyma areas adjacent to stimulated airways. These strain patterns may have profound implications on cellular function from a mechano-transduction perspective (112). Although the idea of studying ASM function in a realistic matrix environment might seem attractive, recapitulating asthmatic airway remodeling in PCLS may be somewhat challenging in practice. Aside from the low availability of human asthmatic tissue, several studies have shown that the method of animal death can affect the function and viability of PCLS. For example, the characteristic thick mucus secretion from the lungs of fatal asthmatics makes them extremely difficult to fill with agarose (113).

Ex vivo airway segments are somewhat similar to PCLS in the sense that they retain a realistic micro-environment and offer the opportunity to study integrated multicellular responses. These models are prepared by finely excising bronchial sections of whole airways and tightly ligating side branches of the airway segments to prevent leaking (114). A critical benefit of airway segments is they allow for invasive protocols that would be nearly impossible in an intact animal. Nevertheless, routine use in research has been hampered by their relatively short lifespan (<1 day), impeding long-term use for research on the chronic effects of airway remodeling on ASM function.

Tissue Engineering

Recently, a spotlight has been placed on tissue engineering techniques to develop custom-built *in vitro* models of human tissue. The goal of these models is to specifically recreate and study essential features linked to disease pathogenesis (115). The techniques used to create human tissue have been broadly divided into two groups, scaffold-based and liquid-based, each of which show potential for recreating the mechanical dysfunction seen in asthma. However, it should be noted that both methods do not preclude one another and can be combined depending on the target application. In scaffold-based models (e.g., electro-spun matrices, polyacrylamide hydrogels), cells are seeded and cultured on a specially configured polymer capable of mimicking the properties of natural ECM, and through cell proliferation/maturation and scaffold remodeling, an engineered tissue is formed (116–118). Liquid-based models (e.g., bulk collagen gels, microtissues, bioprinting) involve pre-mixing cells with one or several biomaterials and utilizing various fabrication techniques to construct neo-tissues with specific micro-architectural features. These neo-tissues are then directed into mature functional tissues by providing biophysical or biochemical growth cues in the cellular micro-environment (119,120).

Common materials used in scaffold-based models include purified isolated ECM components, decellularized matrices (DCM) and synthetic polymers. Scaffolds constructed out of biopolymers (including polypeptide/protein based e.g., collagen, fibrin, gelatin or polysaccharide based e.g., hyaluronic acid) are extremely appealing because they provide a realistic culture model containing a host of signalling molecules easily recognized by cells (121). This intrinsic structural resemblance to native ECM, in addition to their non-toxic products of biodegradation, have resulted in a widespread adoption of these models. For DCM, the decellularization is designed to remove all cellular components, allowing exploitation of all the components of natural ECM. Booth *et al.*, utilized decellularized lung matrices to show stiff lung tissue can drive myofibroblast differentiation via a TGF-β-independent mechanism (122,123). Examples of synthetic materials in scaffold-based tissue engineering, which may be classified as biodegradable and non-biodegradable, include the aliphatic polyesters [including poly (glycolic acid) (PGA) and poly (lactic acid) (PLA)], poly-phosphazenes and polyurethane (124). These materials are typically modified with biological signalling factors and can provide a well-defined, mechanically robust, and easy to reproduce model. Using a common scaffold fabrication technique called electrospinning, Morris *et al.*, created a novel model of ASM with the polymer polyethylene terephthalate (PET). ASM cells in this model demonstrated an elongated cell morphology with variable contractile protein levels and distribution (125). However, regardless of the type of material used, a major shortcoming with scaffold-based models is the inability to easily control the mechanical properties of the 3D micro-environment. Even though researchers have developed innovative techniques to tune the mechanical properties of some scaffolds (126), inherent technical limitations hinder the range of stiffness modification, which is a vital consideration in mechanobiology research. Another key consideration with these models is that heterogeneously seeding cells at tissue-like densities on to scaffolds can be extremely difficult. As a workaround, researchers typically start with low cellular densities and a non-uniform distribution of cells which, apart from requiring incredibly long wait times for proliferation and maturation, might also impact tissue function (127,128).

Liquid-based methods bypass some of these limitations and have been dominating current tissue engineering trends. A ubiquitous liquid-based technique is to infuse cells in free-floating bulk gels constructed out of native ECM proteins. By embedding ASM cells into a collagen gel and subsequently attaching them to cast plates, McParland *et al.* found an increased contractile response to histamine in ASM cells isolated from asthmatic patients compared with control cells (129). However, this method is typically characterized by poor cellular organization and densities. To improve this, as well as to achieve some degree of biomechanical control, some researchers have experimented with seeding bulk gels onto microfabricated platforms to create ‘microtissues’. For example, pre-mixing ASM cells in a collagen-1 gel, followed by seeding on to a microfabricated tissue gauge constructed out of a silicone-based substrate produced an innovative model that allowed for simultaneous contractile force measurement and tunability of the mechanical micro-environment (130). This technique demonstrated that tissue stiffening by increasing cantilever stiffness and matrix crosslinking, enhances ASM contractile responses to acetylcholine and potassium chloride. Nevertheless, this model is heavily reliant on cellular activity to produce a final tissue, and it is highly susceptible to enzymatic degradation, limiting its use in long-term research on airway remodeling. These drawbacks highlight a pressing need for a technique that blends the mechanical robustness of scaffold-based models with the ease of cellular seeding of liquid-based models. Such approaches would potentially satisfy a broad range of applications, including direct assessment of tension development in ASM, as well as mechanical modifications that are especially pertinent to mechano-transduction research.

3D Bioprinting

Additive manufacturing, usually referred to as 3D printing, is a technological advancement that is currently pushing the boundaries of manufacturing possibilities. This is due to its superior ability to mass-produce individually customized products versus traditional manufacturing techniques (131). A 3D printer creates a model structure by depositing materials in a layer-by-layer manner, using a three-axis (X, Y, Z) mechanical platform that precisely follows inputs from a computer design file (132). The most common type of 3D printers function by micro-extrusion, which involves using pneumatic or mechanical pressure to extrude small strands of materials in two dimensions, with each deposited layer serving as a foundation for the next (133). Additive manufacturing with biological materials, biochemical factors and living cells is called 3D bioprinting. In bioengineering, this concept is used to fabricate a reproducible 3D structure with specific spatial arrangement of functional and supporting cell types. Bioprinted models have an enormous potential to create customized human tissues on demand since the physical design of constructs can be easily and rapidly manipulated with high fidelity, enabling a better replication of the complex micro-architecture of *in vivo* environments. Typically, the bioprinting process starts by first creating a 3D design of the model structure, which could be virtually any shape generated by a computer design program (CAD). This 3D design is then analyzed by software that determines how the object should be divided into printable layers and is used to control the motions of the mechanical platforms (134).

To reduce shear stress in the extrusion system, which typically results in low cell viability, tissue engineers often encapsulate cells in polymers that possess shear-thinning or thixotropic properties. This involves alignment of the randomly distributed polymer chains and decreased viscosity that allows these materials to flow easily and regain viscosity after deposition. This mixture of biological materials that provide protection to the cells during printing and ultimately creates the tissue structure is commonly referred to as ‘bio-ink’. In addition to favorable rheological properties, an ideal biological material for extrusion bioprinting should possess physicochemical properties such as rapid gelation, low adhesion, and surface tension characteristics. These properties allow the polymer to overcome various forces during material extrusion and retain its shape without deforming after deposition (fidelity) (135,136).

Our laboratory is currently utilizing a proprietary 'RX-1' bioprinter from Aspect Biosystems as a platform for building state-of-the-art models of structurally remodeled tissue. Rather than using a simple syringe or drop extrusion system, this bioprinter uses a unique microfluidic printhead that facilitates precise control of bio-ink flow using pneumatic pressures and valves, providing extremely high accuracy for depositing materials. The printhead features a set of microfluidic channels that support simultaneous printing with multiple materials and a converging point that enables a technique called coaxial flow focusing. This means liquid bio-inks are rapidly cross-linked into a solid fibre in a chaos-less manner by a crosslinking sheath solution. The approach also protects the cells from shear stresses encountered at the printhead nozzle (137,138). Flow focusing enables tight control over bio-ink crosslinking, so that the fidelity and printing resolution of a wide array of materials (including low viscosity bio-inks) can be kept consistent during dispensing.

The RX-1 bioprinter is nominally designed around alginate, a linear anionic copolymer of L-guluronic (G) and D-mannuronic (M) monomers, commonly obtained from brown algae. These monomers can appear in homogenous chains of consecutive G-subunits, consecutive M-subunits, alternating M and G-subunits or randomly organized blocks. The relative amount of each subunit type varies with the specific origin and processing, which subsequently influences the mechanical properties of alginates. The physicochemical properties and printability of alginates are also directly dependent on the method of gelation e.g., ionic, thermal and covalent (139). Ionic gelation with divalent cations (such as Ca^{2+}) is by far the most common method of alginate crosslinking. In the egg-box model of crosslinking, the cations act as a bridge that electrostatically attract negatively charged carboxylic acid groups from adjacent G subunits to form a 3D gel network that structurally replicates the ECM of native tissues (140). Calcium chloride ($CaCl_2$) is the most frequently used alginate crosslinking agent, because of its rapid action and mild crosslinking properties at physiological conditions, which produces zero harmful by-products. However, this fast and uncontrolled gelation typically creates an unorganized 3D network because of the high solubility of $CaCl_2$ in aqueous media. Through real-time adjustments of microfluidic pressures and the controlled gelation offered by flow focusing, alginate crosslinking with $CaCl_2$ can be dynamically regulated directly on the RX-1 printhead, leading to the formation of a highly organized 3D gel network.

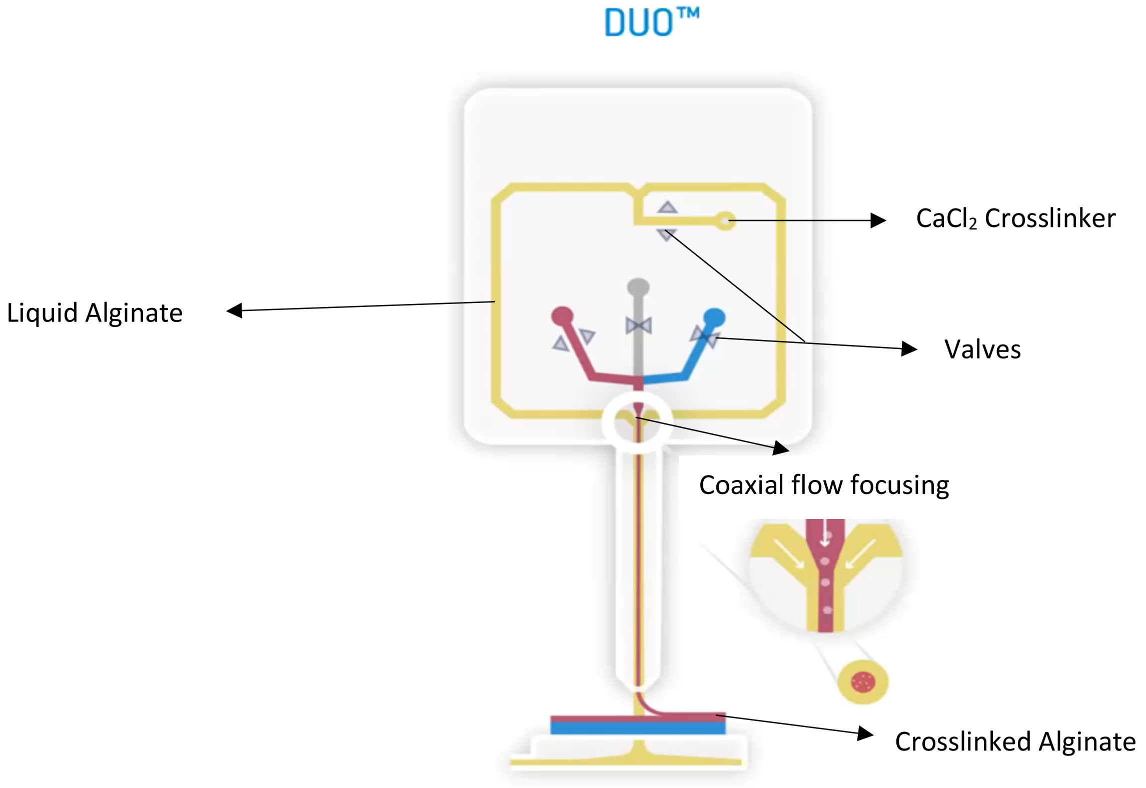

Figure 1.01. Schematic of a microfluidic printhead from Aspect's Biosystem's RX-1 Bioprinter. As the printer moves in X, Y and Z-axes, bio-ink flow is driven by pneumatic pressure and the opening/closing of valves. Coaxial flow focusing is used to sheath the bio-ink in chemical crosslinker, to convert the liquid bio-ink to a solid fibre that is deposited in high fidelity on the print surface.

Depending on the molecular weight (MW), concentration (141,142), and crosslinking strategy (143,144), the mechanical properties of alginate can be fine-tuned to match the elasticity of healthy and diseased airways, making alginate-based matrices an exceptional candidate for ASM mechano-transduction research. Chemical modifications are often required to support cells, as alginate is derived from non-animal sources and inherently lacks signalling molecules essential for cellular differentiation or maturation, and cell adherence proteins are minimally adsorbed onto the hydrophilic alginate residues. Integrating growth factors, biochemical and biophysical cues into constructs is therefore essential to strengthen biocompatibility, foster cell viability and promote cell spreading, cell-cell and cell-matrix interactions. To provide a congenial micro-environment for cells, alginate is often modified with cell attachment peptides. Using aqueous carbodiimide chemistry, an amide linkage is formed between the amine groups in the peptide sequence and the carboxylic acid groups in the alginate backbone (145). The tripeptide RGD (arginine-glycine-aspartate) is a commonly used binding motif that mediates cell adhesion to the ECM and is normally found within a wide range of ECM proteins including fibronectin, laminin and vitronectin (146). Several integrins expressed by ASM bind to RGD motifs, potentially providing excellent biocompatibility (147).

A common addition to alginate-based matrices is collagen-I, the predominant structural protein in connective tissues. Due to its high tensile strength, it mechanically supports and gives cells structure from the outside (148) making collagen ubiquitous in tissue engineering research where it is usually obtained from sustainable animal sources (e.g., rat tail or porcine skin). In addition to providing structural integrity, it also facilitates cell adhesion and growth, due to an abundance of integrin binding domains. Nevertheless, gelation of collagen is an entropy driven process, meaning it remains a liquid at low temperatures, and as the temperature rises (at neutral pH), individual fibrils undergo self-assembly to form a fibrous gel (149). This potentially limits the use of collagen-I as the primary bio-ink component because complete polymerization can take up to 30 minutes, reducing fidelity. Further, the structure may be subject to enzymatic degradation by a wide array of matrix metalloproteinases (150), necessitating the use of supportive materials.

Fibrin is a fibrous and complex polymer commonly used as a support material for collagen. Thrombin forms an insoluble fibrin polymer by cleaving fibrinopeptides in the central region of the soluble fibrinogen glycoprotein. Fibrin is a component of the blood clotting cascade and following tissue injury, it provides the initial scaffold that cells invade to rebuild the damaged tissue (151). This scaffold plays a vital role in supporting adherence, migration, and biochemical interactions for the invading cells. Indeed, by incorporating fibrin into alginate/collagen-based bio-inks, cell viabilities and functionalities of more than 90 percent have been reported (152). However, due to the non-shear-thinning properties of fibrin, it is rarely extruded and results in clogging problems in extrusion bioprinters. Most fibrin-based bio-inks often involve printing with the precursor fibrinogen at low concentrations (<5mg/ml), then performing cleaving/polymerization reactions post-printing (153).

In foundational work, Dickman *et al*., harnessed the unique microfluidic capabilities of the RX-1 to create a functional 3D tissue using primary human ASM cells. Airway myocytes in this model demonstrated a high viability (>90% after 17 days), expressed relevant markers of a 'mature' muscle phenotype, and had pronounced unstimulated reduction in lumen area (i.e., baseline tone) similar to *in vivo* airways. Intriguingly, these tissues displayed acute contractile responses to histamine that were subsequently reversed by the β2-agonist salbutamol. These physiological responses were comparable to human and guinea pig PCLS. Further, adding TGF-β to bioprinted ASM tissues enhanced baseline tone and decreased relaxation responses to the β2-agonist, reminiscent of chronic airway remodeling in asthma, highlighting the relevance of this model in studying vital disease processes (154). However, this model was designed as a simple free-floating ring structure without a biologically relevant mechanical load to oppose muscle contraction and is printed using a fixed proprietary bio-ink. To recapitulate asthmatic airway remodeling and adequately study ASM mechano-transduction pathways, incorporating easily modifiable mechanical loads would be required to create a model with compressive and elastic properties that closely match healthy and diseased airways.

1.2 Knowledge gap and Hypothesis

Asthma is characterized by an aberrant contraction of airway smooth muscle (ASM), which contributes to clinical symptoms by restricting airflow. Numerous studies have demonstrated that characteristic airway remodeling events increase the stiffness properties of airway tissues. However, the precise effects of these mechanical alterations on ASM contractility remain elusive because ASM cell biology is routinely studied in experimental models that fail to properly replicate mechanical factors contributing to excessive airway narrowing. In this regard, I hypothesize that 3D bioprinting technology using an alginate-based bio-ink can be used to create a realistic model of ASM, which would be useful for studying asthma pathogenesis. Moreover, I hypothesize that this model will demonstrate that tissue stiffening enhances ASM contractility.

1.3 Specific objectives

The basic approach I adopted to test this hypothesis was to:

- Optimize the physical design of a three-dimensional construct and the biochemical constituents of an alginate-based bio-ink to support maximal ASM cell maturation, baseline tension development and allow for easy measurement of ASM contraction,
- Modify the biomechanical environment of 3D ASM tissue to simulate the increased stiffening associated with asthmatic airway remodeling,
- Assess ASM morphology, phenotype, and functional responses to a range of contractile and relaxant agents across a stiffness range.

Chapter two: Methodology

2.1 Cell Culture

ASM

Human airway smooth muscle cells immortalized by stable transfection with human telomerase reverse transcriptase were obtained from multiple donors (Table 2.01). The cells had been generated and characterized as described by Burgess *et al.*, (155) and were donated to our laboratory as a generous gift from Dr. Andrew Halayko (Department of Physiology & Pathophysiology, University of Manitoba). Cells were seeded in a 75 cm^2 tissue culture flask (T75; Sarstedt Inc, Nümbrecht, Germany) and maintained in a feeder medium consisting of 89% Dulbecco's Modified Eagle's Medium, Nutrient mixture F-12 (DMEM/F12; #1130-032, Life Technologies, Burlington, ON) supplemented with 10% heat-inactivated fetal bovine serum (FBS; #12483-020, Life Technologies, Burlington, ON) and 1% penicillin-streptomycin (Pen-Strep; #15140-122, Life Technologies, Burlington, ON) adjusted to a pH of 7.3 to 7.5 with a calibrated Orion Star A111 pH meter (ThermoFisher Scientific, Beverly, MA). Cells were maintained in an incubator at 37^oC, 5% CO_2 and 85% relative humidity (RH) until approximately 90% confluent. At confluence, cells were rinsed with 1× phosphate buffered saline (PBS; #70011-044, Life Technologies, Burlington, ON) and treated with a TryplE cell dissociation reagent (#12605036, Life Technologies, Burlington, ON) for 5 minutes at 37^oC to create a single cell suspension. The suspension was then diluted with an equal volume of feeder media and was either reseeded in new flasks, used for experiments, or cryogenically frozen.

Cell Line	Age	Sex	Status	Tissue	hTert
2691MA	25	M	Asthmatic	Biopsy	27-Sep-12
2728M	21	F	NHV	Biopsy (RLL)	28-Mar-13
2929M	69	M	NHV	Biopsy	28-Mar-13
3002MA	33	M	Asthmatic	Biopsy	27-Sep-12
3376MA	44	M	Asthmatic	N/A	14-Mar-13
D12	N/A	N/A	N/A	N/A	N/A

Table 2.01. Characteristics of human airway smooth muscle cell lines used. The hTert column represents the date cells underwent immortalization with human Telomerase reverse transcriptase. NHV and RLL denote normal healthy volunteers and right lower lobe respectively.

Growth curves

ASM cells were seeded at 5×10^3 cells/cm^2 in a 25 cm^2 culture flask (T25; Sarstedt Inc, Nümbrecht, Germany) containing feeder media supplemented with 200µg/mL geneticin (G418; #10131035). After 24 hours, cells were dissociated with TrypLE and diluted with a 1:1 feeder volume, after which a small volume (~50 µL) was taken, mounted on a hemocytometer (#267154, ThermoFisher Scientific, Waltham, MA) and counted using the EVOS imaging system (EVOS® FL, ThermoFisher Scientific, Waltham, MA). Cell counts were repeated daily for up to 10 days.

2.2 Alginate hydrogels

Ultrapure sterile alginates were selected to comprise the base component of a new customizable bio-ink. By selecting different G/M ratios and molecular weights, the viscosity for bioprinting and stiffness of the final hydrogel can be modulated. Before the beginning of each experiment, 3 % (w/v) stock alginate solutions were made by dissolving 100% freeze-dried sterile sodium alginate (SLM-20; #4202221, SLM-100; # 4202301, SLG-20; #4202001 and SLG-100; #4202101, Novamatrix, Sandvika, Norway) in alginate diluent buffer (145mM NaCl, 5mM $NaHCO_3$, pH 7.0-7.4).

To identify candidate bio-inks that supported maximal cell viability and function, I performed initial biocompatibility testing using thin hydrogels, which were prepared via external gelation with our alginate-based matrices and AG-10 (Aspect Biosystems, Vancouver, Canada). Stock alginate solutions were diluted to desired working concentrations, functionalized by adding 1 mg/mL collagen-I (#354236, Corning, NY) and buffered as needed to achieve a physiological pH of 7.4 (tested using a 6.0 – 8.0 pH paper). AG-10 was reconstituted as per the manufacturer's instructions. To prepare hydrogels, ~150µl of each alginate mixture was spread on 0.4 µm ThinCert membranes and was then transferred to a proprietary calcium-based crosslinking solution (CAT-2, Aspect Biosystems, Vancouver, Canada) at 37ºC and 85% RH for 10 minutes. This high temperature facilitates collagen gelation, while calcium diffusion into the alginate creates a functionalized hydrogel ~200µm thick. Cells were then seeded onto the hydrogels at a range of cell densities (1×10^4 to 4×10^4 cells/cm^2) and maintained in standard culture conditions.

Alginate	Appr. Mw [kDa]	G/M Ratio	Viscosity (mPa)s	Expected Hydrogel Stiffness (Arbitrary)
SLM-20	75-150	≤ 1	20-99	*
SLM-100	150-250	≤ 1	100-300	**
SLG-20	75-150	≥ 1.5	20-99	****
SLG-100	150-250	≥ 1.5	100-300	*****
AG-10*	-	-	-	-

Table 2.02. Panel of alginates used. The mechanical properties of alginate matrices are expected to be significantly influenced by alginate concentration, guluronate residue content, and molecular weight of the copolymer chains. *Biochemical properties of AG-10 are uncharacterized.

2.3 3D Bioprinting

Tissue Design

3D models were created within the Aspect Studio software or TinkerCAD (https://www.tinkercad.com) and saved in stereolithography file format (.STL). The STL file was imported into Aspect Studio, print parameters set (infill density, infill pattern, number of perimeters, layer height, print speed) and a tissue design assembly (.tda) file generated. Figure 2.01 shows the standard Aspect Biosystems 15 mm bio-ring design replicated using a cylinder (15 mm diameter, 1.5 mm high), printed with no infill, 1 perimeter and a 0.1 mm layer height.

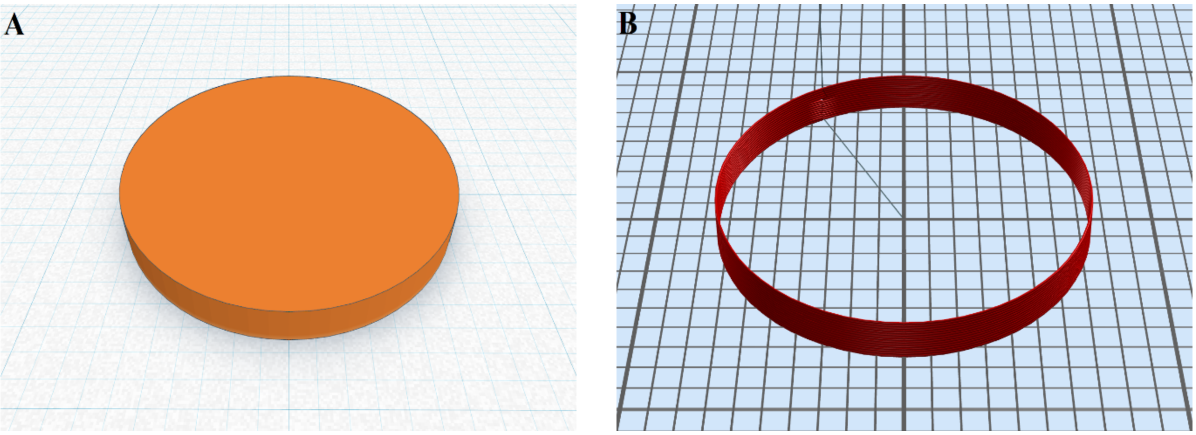

Figure 2.01. Standard bio-ring design. (A) 3D STL model (15mm diameter hollow cylinder) describes the raw, unlayered and triangulated external surface of the object. (B) Schematic of tda model file, which carries information about how the construct is to be divided into printable layers.

Bio-ink Preparation

A bio-ink needs to be formulated to support cell survival during and after the bioprinting process. This includes the usage of bio-compatible matrix components, balancing pH, and maintaining consistent salt/water content to create an isotonic solution. Moreover, it is essential to be able to flexibly mix components from concentrated stock solutions to create bio-inks with different properties. Cellular bio-inks were prepared either by preparing AG-10 as per the manufacturer's instructions, or by using our own custom bio-ink formulations. The three core components of our bio-ink are alginate, collagen, and fibrinogen. Lyophilized alginates were reconstituted in alginate diluent buffer as described in section 2.2. Collagen-I was purchased as a commercial product at >3 mg/mL in 0.02N acetic acid. Fibrinogen (#F8630, Sigma-Aldrich, Saint-Louis, MO) stock solution was created by dissolving >20 mg/mL fibrinogen in alginate diluent buffer and subsequently diluted to working concentrations as needed. An Excel based calculator was developed and used to calculate volumes of each component in the bio-ink. The inputs for the calculator were the desired final volume of bio-ink, and the stock and final concentrations of each matrix component. The calculator then calculated the volume of 7.5% $NaHCO_3$, 1.5 M NaCl, and ddH_2O to precisely neutralise the acid from the collagen and achieve final salt concentrations of 145 mM NaCl and 5 mM $NaHCO_3$. The dilution calculator also corrected for micro-volume errors associated with pipetting viscous alginates by recalculating total volumes based on actual pipetted volumes. This ensured standardization and significantly minimized variations between print runs.

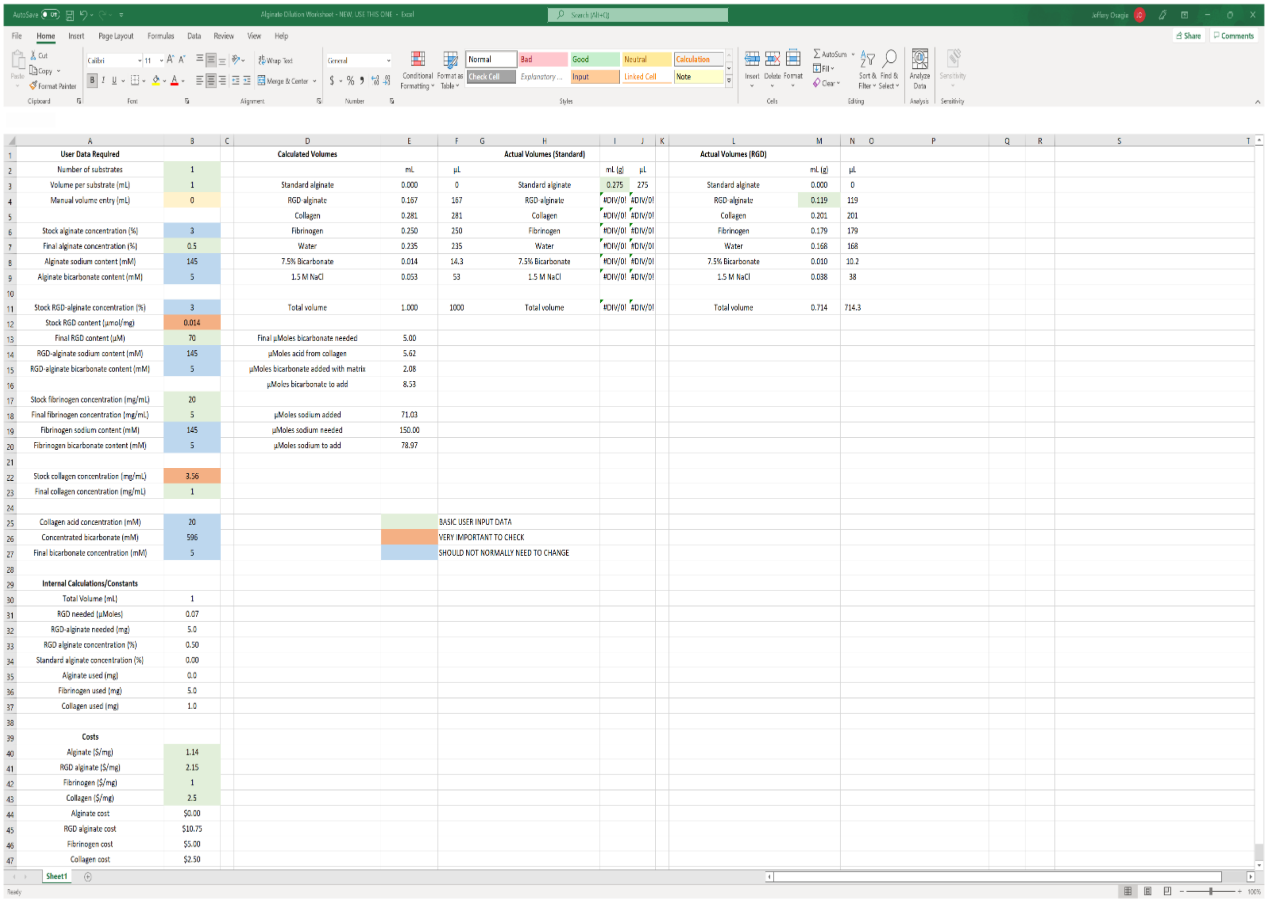

	A	B
1	**User Data Required**	
2	Number of substrates	1
3	Volume per substrate (mL)	1
4	Manual volume entry (mL)	0
5		
6	Stock alginate concentration (%)	3
7	Final alginate concentration (%)	0.5
8	Alginate sodium content (mM)	145
9	Alginate bicarbonate content (mM)	5
10		
11	Stock RGD-alginate concentration (%)	3
12	Stock RGD content (µmol/mg)	0.014
13	Final RGD content (µM)	70
14	RGD-alginate sodium content (mM)	145
15	RGD-alginate bicarbonate content (mM)	5
16		
17	Stock fibrinogen concentration (mg/mL)	20
18	Final fibrinogen concentration (mg/mL)	5
19	Fibrinogen sodium content (mM)	145
20	Fibrinogen bicarbonate content (mM)	5
21		
22	Stock collagen concentration (mg/mL)	3.56
23	Final collagen concentration (mg/mL)	1
24		
25	Collagen acid concentration (mM)	20
26	Concentrated bicarbonate (mM)	596
27	Final bicarbonate concentration (mM)	5
28		
29	**Internal Calculations/Constants**	
30	Total Volume (mL)	1
31	RGD needed (µMoles)	0.07
32	RGD-alginate needed (mg)	5.0
33	RGD alginate concentration (%)	0.50
34	Standard alginate concentration (%)	0.00
35	Alginate used (mg)	0.0
36	Fibrinogen used (mg)	5.0
37	Collagen used (mg)	1.0
38		
39	**Costs**	
40	Alginate ($/mg)	1.14
41	RGD alginate ($/mg)	2.15
42	Fibrinogen ($/mg)	1
43	Collagen ($/mg)	2.5
44	Alginate cost	$0.00
45	RGD alginate cost	$10.75
46	Fibrinogen cost	$5.00
47	Collagen cost	$2.50

	D	E	F
1	**Calculated Volumes**		
2		mL	µL
3	Standard alginate	0.000	0
4	RGD-alginate	0.167	167
5	Collagen	0.281	281
6	Fibrinogen	0.250	250
7	Water	0.235	235
8	7.5% Bicarbonate	0.014	14.3
9	1.5 M NaCl	0.053	53
10			
11	Total volume	1.000	1000
12			
13	Final µMoles bicarbonate needed	5.00	
14	µMoles acid from collagen	5.62	
15	µMoles bicarbonate added with matrix	2.08	
16	µMoles bicarbonate to add	8.53	
17			
18	µMoles sodium added	71.03	
19	µMoles sodium needed	150.00	
20	µMoles sodium to add	78.97	
21			
22			
23			
24			
25		🟩	BASIC USER INPUT DATA
26		🟧	VERY IMPORTANT TO CHECK
27		🟦	SHOULD NOT NORMALLY NEED TO CHANGE

	H	I	J	L	M	N
1	**Actual Volumes (Standard)**			**Actual Volumes (RGD)**		
2		mL (g)	µL		mL (g)	µL
3	Standard alginate	0.275	275	Standard alginate	0.000	0
4	RGD-alginate	#DIV/0!	#DIV/0!	RGD-alginate	0.119	119
5	Collagen	#DIV/0!	#DIV/0!	Collagen	0.201	201
6	Fibrinogen	#DIV/0!	#DIV/0!	Fibrinogen	0.179	179
7	Water	#DIV/0!	#DIV/0!	Water	0.168	168
8	7.5% Bicarbonate	#DIV/0!	#DIV/0!	7.5% Bicarbonate	0.010	10.2
9	1.5 M NaCl	#DIV/0!	#DIV/0!	1.5 M NaCl	0.038	38
10						
11	Total volume	#DIV/0!	#DIV/0!	Total volume	0.714	714.3

Figure 2.02 Alginate dilution calculator. Excel-based dilution calculator estimates precise volumes of buffers required to neutralize excess hydrogen ions from collagen stock solution, ensuring tonicity and pH of bio-inks were within physiological levels.

To create homogenous mixtures, each ingredient was added dropwise with continual mixing over ice to prevent early gelation of collagen. Fibrinogen was added last as we found it formed insoluble precipitates if it was added to the bio-ink before collagen. After mixing, the pH of the mixture was confirmed to be in the range of 7.0 to 7.4 with a 6.0 to 8.0 pH paper. For bio-inks containing cells, cells were detached from culture flasks using TryplE, resuspended, and cell concentration calculated using a hemocytometer. An aliquot of cells was then centrifuged at 150 × RCF for 5 minutes (v5804R, Eppendorf, AG, Germany). After centrifugation the supernatant was removed, and cells were resuspended in ice-cold bio-ink at a density of 2.5×10^7 cells/mL.

Printing

The bioprinter was set up as per the manufacturer instructions. In brief, a DUO (two bio-ink channels) or QUAD (four bio-ink channels) microfluidic printhead was mounted on the Aspect Biosystems RX-1 Bioprinter. Tubes containing bio-inks and bottles containing alginate diluent buffer and CAT-2 crosslinker were sealed with a pneumatic cap and tubing before the tubing was connected to separate material channels on the bioprinter. The pneumatic tubing and printhead were then primed with bio-ink, buffer or crosslinker to remove air bubbles. Tissues were printed onto porous Thincert membranes (PET, 24 mm diameter, 8.0 µm pore size) mounted on a vacuum chuck to capture the printed material and allow excess crosslinker and buffer to flow through. Printed constructs were deposited layer by layer as per the specified tda file, and material pressures and print speeds were varied to account for the different rheological properties of different bio-inks (Table 2.03). All print runs were completed within 30 minutes of adding cells to bio-inks, to minimize variance throughout the print run that can arise from cell sedimentation/clumping and premature precipitation/gelation of bio-ink components.

Material	**Print Pressure (mBar)**	**Print Speed (mm/sec)**
AGC-10	25 — 30	25
0.25% VLVG	18 — 22	32
0.375% VLVG	20 — 28	32
0.5% VLVG	25 — 30	32
0.75% VLVG	30 — 50	30
0.75% SLG-20	55 — 60	23
1% SLG-20	80 — 100	20
1.25% SLG-20	125 — 140	18
1.5% SLG-20	200 — 300	15
2% SLG-20	300 — 500	10
Crosslinker	60 — 70	N/A
Buffer	100	N/A

Table 2.03. Approximate print pressures and speeds. Since fidelity and resolution of constructs are dominated by print pressures and speeds (156), these were monitored constantly to ensure consistency.

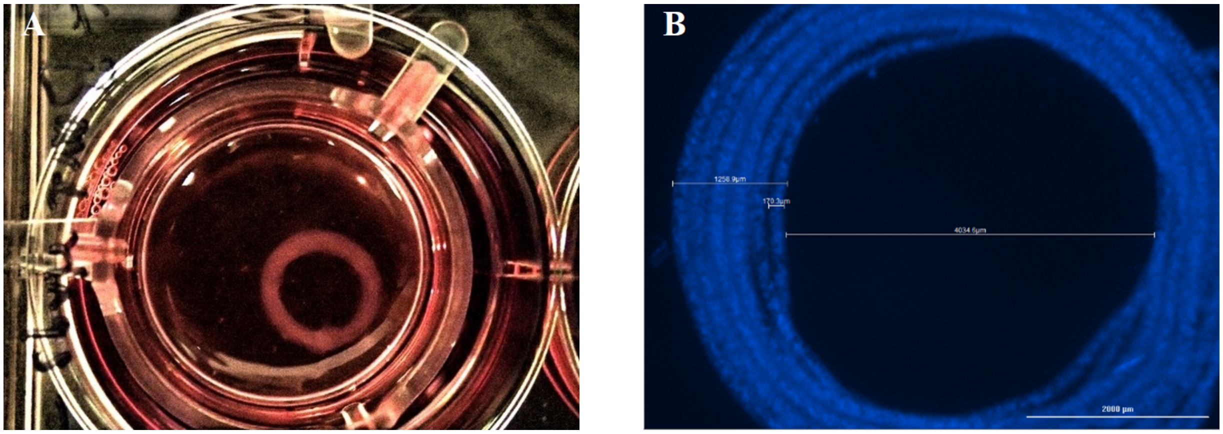

Figure 2.03. Representative image of ASM tissue at day 0. Printed using a one-step bioprinting process following the standard bio-ring design. (A) Gross morphology indicates excellent printing fidelity that closely matches the 3D tda design. (B) DAPI stained 1.25× image of bio-ring shows homogenous distribution of cell nuclei above and below axis of focus, indicating formation of a true 3D structure. Scale bar = 2000 µm

Post-printing

Immediately after printing, Thincert inserts containing tissues were placed into a 6-well plate containing feeder media and maintained under standard culture conditions. For tissues containing fibrinogen, the feeder media was supplemented with 1.25 U/mL thrombin (#T4648, Sigma-Aldrich, Saint-Louis, MO) to cleave and polymerise fibrinogen to fibrin, before switching tissues to regular feeder media after 30 minutes. Culture plates were gently agitated to ensure constructs detached from the inserts and floated freely in the feeder media. Cell health, viability and morphology were tracked daily by live cell microscopy and contractile function was assessed on day 6.

2.4 Cell viability

Live/dead cell counting

On designated days, feeder media was removed, and cells were washed once with 1× Hank's Balanced Salt Solution (HBSS, # 14185052, Life Technologies, Burlington, ON) containing calcium to prevent alginate decrosslinking. ASM tissues were then placed in a 1% serum feeder media containing 1 µg/mL propidium iodide (PI304MP, ThermoFisher Scientific, Waltham, MA) and 1 µg/mL Hoechst 33342 (#H1399, ThermoFisher Scientific, Burlington, ON). Constructs were incubated at 37ºC for 30 minutes, after which they were washed once again with

HBSS and imaged on the Cytation 5 Cell Imaging Multi-Mode Reader and Gen5 Software (Biotek Instruments Inc, Winooski, VT) using DAPI (#1225100, Biotek Instruments Inc, Winooski, VT) and Texas Red (#1225102, Biotek Instruments Inc, Winooski, VT) imaging cubes and 4×, 10×, 20× objective lenses at 37°C and 5% CO_2. Images were captured at multiple focal lengths to visualise live/dead cells at multiple depths through the tissues.

Lactate dehydrogenase (LDH) release assays

At specific time points, culture media was removed from printed constructs and centrifuged at 250 × RCF for 5 minutes. Cell free supernatant was collected and stored at 2 to 8°C until use. Two controls were established, a 1% serum media (media control) and a 100 percent lysis control, obtained by lysing cells with 1% Triton X-100 (#H5141, Promega Corporation, Madison, WI). Roche's Cytotoxicity detection kit (#11644793001, Sigma-Aldrich, Saint-Louis, MO) consisting of a diaphorase and NAD^+ catalyst, as well as an iodotetrazolium chloride (INT) and sodium lactate dye in 1:45 dilution was used for all LDH release experiments. For each experiment, working solutions of the test kits were freshly prepared by mixing the catalyst and dye solutions thoroughly. This was then transferred to an optically clear flat-bottomed 96-well plate containing previously collected supernatant and incubated in the dark for up to 30 minutes. Absorbance readings were taken at 490nm and 620nm (reference wavelength) using the Cytation 5 and the Gen 5 software. Cellular cytotoxicity was calculated using the following equation:

$$\%\ Cytotoxicity = 100 \times \left(\frac{Experimental\ sample — Media\ control}{100\ percent\ lysis\ control — Media\ control} \right)$$

Equation 2.01. Percent Cytotoxicity.

2.5 Immunofluorescence

3D tissues and 2D coverslips were rinsed once with HBSS, then fixed with 4% paraformaldehyde (#P6148, Sigma-Aldrich, Saint-Louis, MO) in HBSS for 10 minutes. Subsequently, tissues and coverslips were permeabilized with 0.1% triton X-100 and 4% paraformaldehyde in HBSS for 5 minutes, after which they were washed three times with HBSS and stored at 4°C prior to staining. Actin filaments were stained with 1U phalloidin (#A12379, ThermoFisher Scientific, Waltham, MA) in HBSS for 1 hour in the dark. Next, constructs and coverslips were rinsed three times with HBSS, and counterstained for nuclei with 0.1 µg/mL Hoechst 33342 in HBSS for 30 minutes in the dark. 3D tissues and coverslips were imaged with Cytation 5 and Gen5 software using the GFP (#1225101, Biotek Instruments Inc, Winooski, VT) and DAPI light cubes for phalloidin and Hoechst respectively.

2.6 3D Contractile Function

Image and video capture

Macroscopic images of printed tissues were captured daily using an Olympus Tough TG-1 iHS digital camera (Olympus Imaging Corp., Tokyo, Japan), equipped with a 12-megapixel lens and mounted on a tripod stand. Camera height and focus were optimized using 6-well plates with Thincert inserts such that the entire plate was in the field of view. Videos of muscle responses to contractile agonists, relaxant agents and alginate decrosslinking/load removal were obtained under a high-quality video mode (1920 × 1080p, 30 fps). I performed all image and video capture on an isolated table to prevent any deflection artifacts. The videos were processed by ffmpegTool to create single image sequences, which were analyzed to determine changes in lumen area.

Image processing

Lumen area reduction was quantified from processed image sequences using Fiji Imaging software. Images were uniformly adjusted for brightness and contrast only, ensuring no details were obscured, and the Canny edge detector plugin (for ImageJ) was used to highlight borders of the construct. The internal area of each ASM tissue was then measured using the manual tracing feature. Measured pixel distance between lines on a millimeter ruler was used to calculate a calibration factor of 0.018 μm^2 per square pixel. Percentage change in lumen area was then calculated with the following formula:

$$\% \; decrease = 100 \times \left(\frac{Initial\ Lumen\ Area - Final\ Lumen\ Area}{Initial\ Lumen\ Area}\right)$$

Equation 2.02. Lumen area reduction calculation.

Drug testing

ASM tissues were serum deprived 48 hours after printing using low serum media consisting of DMEM/F12 supplemented with 1% insulin transferrin selenium (ITS; #41400045, Life Technologies, Burlington, ON), and 0.5% FBS. Tissue health and gross morphology were qualitatively assessed, and one representative ASM tissue from each stiffness range was selected and placed in fresh low serum media. Before the start of each experiment, selected tissues were allowed to adjust to room temperature by placing them on an isolated table for 10 minutes. Video recording was initiated to capture images representing baseline tone, which was used to normalise the contraction data. Supramaximal doses of contractile and tension ablating drugs were prepared and administered as described previously (130). In brief, treatments included 100 µM acetylcholine chloride (#A6625, Sigma-Aldrich, Saint-Louis, MO), isotonic 80 mM KCl and 10µM cytochalasin D (#SC201442, Santa Cruz Biotechnology, Dallas, TX), each prepared in low serum media and added sequentially to ASM tissues for 10-minute treatments. To ensure even drug distribution, approximately one third of the drug dose was added to the interior of the Thincert insert and two-thirds added to the exterior well. Drugs were administered carefully to limit agitation of the muscle tissues.

Alginate decrosslinking

To remove the mechanical load contributed by the acellular alginate layers and characterize shortening dynamics of the unloaded cellular layer, calcium chelation was used to decrosslink alginate (157). Three chelation solutions were trialed; 50mM tri-sodium citrate (#111037, Millipore-Sigma, Oakville, ON), 40mM tri-sodium citrate + 15mM ethylenediaminetetraacetic acid (EDTA; #324503, Millipore-Sigma, Oakville, ON) and 300mM NaCl (#S3014, Sigma-Aldrich, Oakville, ON). These solutions were adapted from Wu *et al* (158) and adjusted where possible to achieve physiological tonicity. Solutions were prepared in DMEM/F-12, buffered to pH 7.3 – 7.4 using 1M NaOH (#CC38215-1, Sigma-Aldrich, Saint-Louis, MO) or 6N HCl (#7647-01-0 Fisher Scientific, Fair Lawn, NJ) and filter sterilized with a 0.22 µm membrane filter (# 635387, Millipore, Oakville ON). On day 6, serum deprived ASM tissues were rinsed once with HBSS, decrosslinking solutions were administered for 10 minutes, and videos captured as described above.

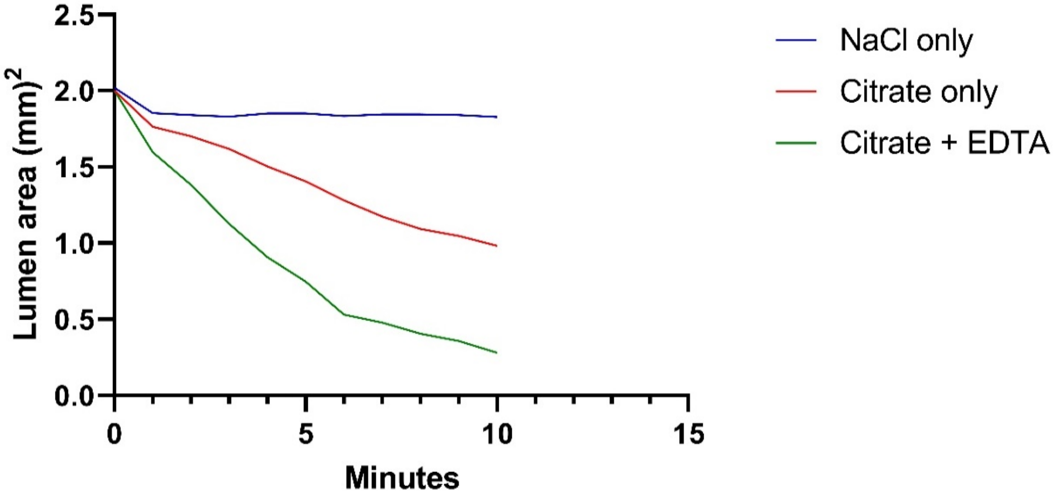

Figure 2.04. Alginate decrosslinking. Citrate + EDTA solution caused a reduction in lumen area by more than 50% within 5 minutes. Thus, it was deemed most potent and used for subsequent experiments.

Concentration-response assays

A dose response curve to acetylcholine was constructed by preparing serial dilutions of a 10mM stock solution in low serum media, to achieve final concentrations of 10nM, 100nM, 1µM, 10µM and 100µM. Working solutions were administered sequentially for 10 minutes, from lowest to highest concentration, while videos were captured. Data were fitted to the Hill equation to calculate EC_{50} values.

2.7 RNA isolation

Alginate is a polysaccharide that forms poorly soluble ionic complexes with nucleic acids, which compromise RNA quality and interfere with the isolation process. Thus, conventional RNA extraction techniques used for mammalian 2D cell cultures that utilize chaotropic agents (e.g., guanidine isothiocyanate) and thiols (e.g., β-mercaptoethanol) are not appropriate (159–161). Due to the structural similarity of alginate to plant polysaccharides, we trialed several commercially available plant-based RNA extraction kits and compared them with conventional mammalian cell methods (Table 2.04) by assessing RNA yield, concentration, and purity. For a detailed description of each technique tested, please refer to table B in the appendix (p. 99).

Kit tested	Principle
PureLink RNA Mini Kit (#12183025, Life Technologies, Burlington, ON)	Cells are first lysed and homogenized in a buffer containing guanidine thiocyanate. Lysates are then mixed with ethanol, which in conjunction with the chaotropic salt facilitates RNA binding to a silica-based spin-cartridge. Impurities are washed out and pure RNA is eluted with nuclease free water.
Tri Reagent (TRIzol; #93289, Sigma-Aldrich, Oakville, ON)	Liquid-liquid extraction involving homogenizing cells in a mono-phasic TRIzol solution. Subsequent addition of chloroform and centrifugation separates the solution into organic and aqueous (which contains the RNA) phases. Pure RNA is recovered by precipitation with isopropanol.
CTAB (#D44026, Millipore-Sigma, Oakville, ON)	An extraction buffer composed of hexadecyltrimethyl ammonium bromide, polyvinylpyrrolidone, and β-mercaptoethanol is used to breakdown polysaccharides and prevent the oxidation of phenolic compounds. Homogenates are then separated into two phases with chloroform and pure RNA is precipitated with isopropanol.
GeneJET Plant RNA Purification Mini Kit (#K0802, ThermoFisher Scientific, Waltham, MA)	Utilizes a solid-phase extraction similar to PureLink but optimized for high-polysaccharide plant tissues.
Plant RNA Reagent (#12322012, Life Technologies, Burlington, ON)	A proprietary RNA isolation reagent that uses phase separation with NaCl and chloroform. RNA is precipitated with isopropanol.

Table 2.04. RNA Isolation Methods**.**

RNA purity and concentration were measured using a 2 µL sample volume and a Take3 microvolume microplate (#11-120-571, Biotek Instruments Inc, Winooski, VT) coupled with the Cytation 5 spectrophotometer. For the CTAB samples, a UV-Vis spectrophotometer (NanoDrop-2000, ThermoFisher Scientific, Waltham, MA) was used. RNA purity was assessed using absorbance ratios (A_{260}/A_{280} and A_{260}/A_{230}) and concentration assessed from A_{260} using the Beer-Lambert Law. Total yield was determined by concentration multiplied by elution volume.

2.8 Reverse transcription and mRNA abundance

RNA was reverse transcribed to complementary DNA (cDNA) using iScript Reverse Transcription Supermix (#1708841, Bio-Rad, Hercules, CA). Samples were prepared following the kit vendor's protocol. In brief, 0.3-0.5 µg total RNA was added to 4 µL of 5× iScript supermix and an appropriate volume of nuclease free water (#10977023, Sigma-Aldrich, Oakville, ON) for a 20 µL reaction volume. Reverse transcription was then carried out by incubating the mix at 25^{o}C for 5 minutes, 42°C for 30 minutes and at 95°C for 1 minute using the Techne Touchgene Programmable Thermal Cycler (#FTG05TP, Conquer Scientific, San Diego, CA). cDNA was diluted with TE-Buffer (TE, pH: 8, AM9849, ThermoFisher Scientific, Waltham, MA) to an equivalent of 10 ng/µL RNA and stored at -20°C.

Relative mRNA abundance was determined using semi-quantitative real time polymerase chain reactions (qPCR). A reaction mix consisting of 10 µL 2× SYBR Green supermix (#1725274, Bio-Rad, Hercules, CA), 300 µM of each forward and reverse primers, 2 µL cDNA template (equivalent to 20 ng RNA) and nuclease free water in a 20 µL reaction volume. Primers for housekeeping and test genes are detailed in table 2.05.

Gene code	***Forward Primer Sequence, 5' – 3'***	***Reverse Primer Sequence, 5' – 3'***	***Accession No. (Amplicon Location)***
GAPDH	CTGACTTCAACAGCGACACC	CGTTGTCATACCAGGAAATGAG	NM_002046.5 (1039-1137)
YHWAZ	TCCCCAGAGAAAGCCTGCTC	ATCCGATGTCCACAATGTCAAG	NM_003406.3 (688-831)
UBC	TGGCACAGCTAGTTCCGTC	CACGAAGATCTGCATTGTCAAGTG	NM_021009.6 (382-473)
MHC	CTGCAGAGACAGCTTCACGA	CTCCCCTTGATGGCAGAGTC	NM_002474.2 (4887–5026)
α-actin	AGCCAAGCACTGTCAGGAATC	CAGAGCCATTGTCACACACC	NM_001613.2 (77-165)
SM22α	AGAACTTCCAAGGAGCTTTCCC	GCCACACTGCACTATGATCC	NM_001001522.1 (492-635)
MMP-3	ACAAAGGATACAACAGGGACC	TGGCTGAGTGAAAGAGACCC	NM_002422 (675-756)

DES	CCAACAAGAACAACGACGCC	ATCAGGGAATCGTTAGTGCCC	NM_001927.3 (1006-1123)
VIM	ATCCAAGTTTGCTGACCTCTC	TCAGTGGACTCCTGCTTTGC	NM_003380.3 (1289-1366)
COL-1	CACCCCACGCTCAGATACAG	ATCACATCCACACGGTAGCC	NM_000088.3 (215-347)
FN-1	CCAAGACGAAGACATCCCACC	GTCATCGCACAACACCTTGC	NM_001306129.1 (2968-3093)

Table 2.05. Primers used for qPCR gene expression analysis. Primers were selected using the Primer-BLAST tool (http://www.ncbi.nlm.nih.gov/tools/primer-blast/) to span exon-exon junctions, which prevented amplification of genomic DNA.

Samples were pipetted in duplicate into 96-well qPCR plates (#HSP9655, Bio-Rad, Hercules, CA), and amplified with the CFX96 Touch Real-Time PCR Detection System (#1855195, Bio-Rad, Hercules, CA). No template controls confirmed an absence of contaminating cDNA in the PCR master mix. Thermal cycling conditions involved an initial 10-minute incubation at 95°C for Taq activation and cDNA template denaturing, followed by 40 cycles of primer annealing and extension at 58°C for 30 seconds and melting at 95°C for 10 seconds. Cycle thresholds (Cq) were determined using Bio-Rad CFX Maestro software, (v4.1.2433.1219, Bio-Rad, Hercules, CA) and reaction efficiency was determined by LinRegPCR (v 2018.0, Academic Medical Center, Amsterdam)(162). Primer specificity was continually assessed by melt curve analysis. Cq inputs for Bestkeeper software (v1, www.wzw.tum.de/genequantification/bestkeeper) and $E^{\Delta Cq}$ inputs for NormFinder (v5 for R, MOMA, Aarhus, Denmark) were used to determine stably expressed housekeeping genes. To achieve linear relative values, the data were analyzed such that the sample with the lowest Cq was used as the calibrator. Relative gene expression was determined by calculating the fold change ratio of efficiency-corrected $^{\Delta}$Cq of target genes to internal control genes with the following equation:

$$Relative\ mRNA\ abundance = \frac{E^{(-minC_q - sampleCq)}{}_{target}}{E^{(-minC_q - sampleCq)}{}_{housekeeping}}$$

Equation 2.03. Formular for calculating relative mRNA abundance.

2.9 Statistical analysis

All statistical tests were performed with the GraphPad Prism 8.4.3.686 software package. Unless otherwise specified, all numerical data are reported as mean ± standard error of mean (SEM). *t*-tests, one- and two-way ANOVA followed by a Tukey's correction for multiple comparisons, were computed to detect significant differences between tested groups. $P < 0.05$ was considered statistically significant.

Chapter three: Results — Optimization of Bio-ink and 3D design

3.1 Cell selection

Bioprinting requires a large number of cells (>2.5×10^7 cells/mL) to closely mimic tissue-like densities and significantly minimize gaps between cells in printed constructs. To better predict timelines and select a cell line capable of reliably generating the large quantities of cells required for this project, I prepared growth curves of several human ASM cell lines (Figure 3.01).

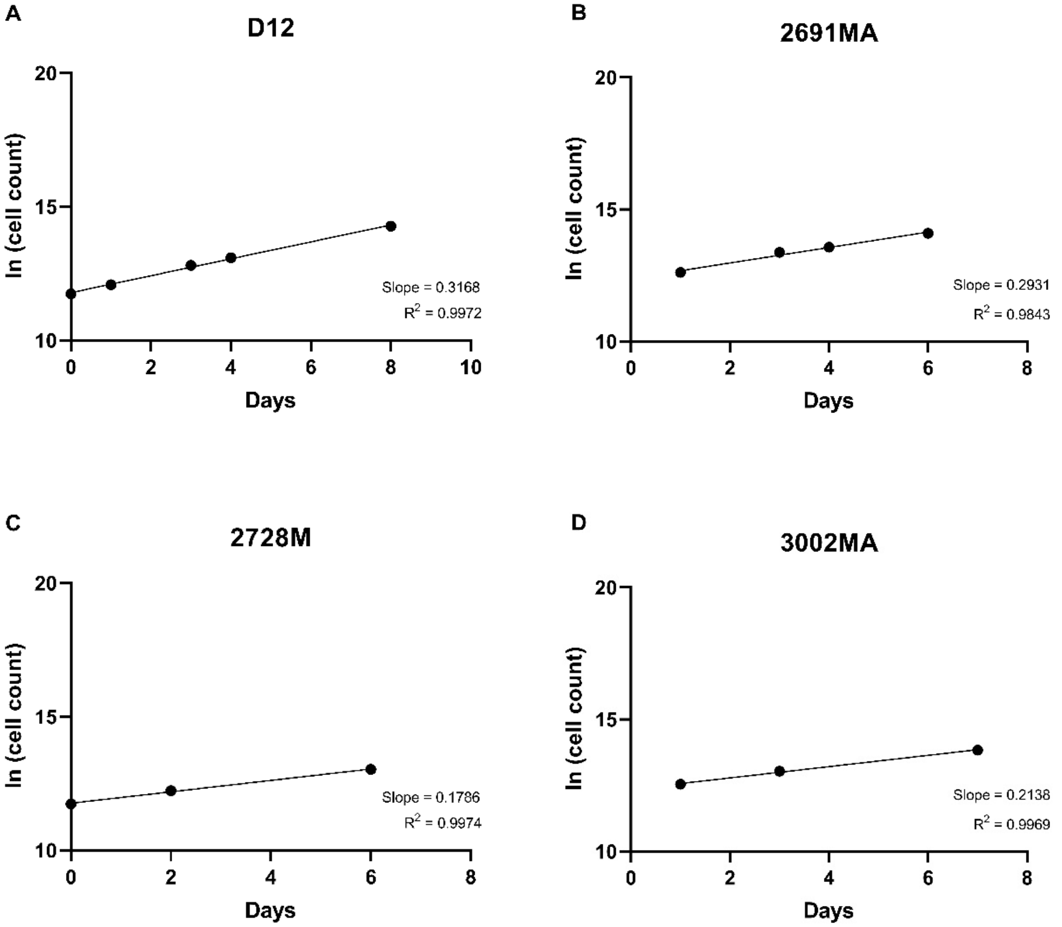

Figure 3.01. Human ASM Growth Curves. Representative images of selected cell lines. Cell counts were transformed to ln (cell count) and results were fitted with linear regression. Early lag and late plateau points that did not correspond to exponential growth were excluded from analysis (R^2 approaching 1 was used as a guide).

Cell line	**Doubling time (Days)**	**Doubling time (Hours)**	**Estimated time to generate 1.0×10^7 cells from 5.0×10^5 cell input (Hours)**
D12	2.19	52.5	228.4
2929M	2.51	59.9	257.0
2728M	3.88	93.1	402.9
3002MA	3.18	76.2	329.9
2691MA	2.36	56.8	243.3
3376MA	5.80	139.2	602.2

Table 3.01. Doubling times of candidate ASM cell lines. Computed as ln (2)/K, where K is the slope of the regression line. The 'time to generate' calculation was based on producing 400 μL of bio-ink at 2.5×10^7 cells/mL

Initially, for bio-ink development and 3D design optimization strategies, I alternated between 2929M, 2728M and 2691MA cell lines based on their growth rates. Ultimately, these cells were supplanted by D12, which consistently and rapidly produced the large number of cells required for bioprinting iterations due to their relatively short doubling times (Table 3.01). Further, since a previous model of ASM (3D microtissues) was developed and characterized using the D12, these cells were chosen to better determine whether the bioprinted model was a direct improvement.

3.2 Alginate pre-screening and bio-ink optimization

The quality of bioprinted constructs is defined by the accuracy of the spatial distribution of materials within deposited layers, termed resolution. The resolution in the x and y axis (lateral resolution), combined with the resolution at z axis (dimensionality) determines the overall shape fidelity of the printed structure (163). While several bioprinter factors such as nozzle diameter and printing toolpath can alter resolution in printed models, intrinsic biomaterial properties including shear-thinning properties, contraction/swelling and crosslinking dynamics are by far the most important determinants of the final shape of constructs (164). To develop an optimal bio-ink formulation that was easy to prepare, easy to print and supported cell survival and maturation in 3D, I created thin alginate hydrogels of varying compositions, determined their practical handling capabilities, and characterized cellular morphology.

Generation of a mature muscle tissue involves multiple distinct steps that require precursor cells to establish significant cell-cell, cell-matrix networks, locally align and fuse to form a functional unit. This process is driven by formation of specialized junctions, containing cell adhesion molecules, which are linked intracellularly by condensed actin fibres. These actin filaments then polymerize to form prominent filamentous networks (f-actin), which maintains and strengthens the contact between cells (165). Visualizing f-actin fibres in ASM cells seeded at 10×10^3 cells/cm^2 using on polymerized AG-10, revealed a rounded cellular morphology and a failure to develop significant cell-cell connections (Figure 3.02). In an attempt to foster cellular crosstalk and promote maturation, I increased cell densities to as high as 40×10^3 cells/cm^2. However, this had no effect on the observed morphology of f-actin. Strikingly, there were no significant changes in cellular proliferation, spreading and alignment (all <10%) after more than 7 days in culture using AG-10 matrix.

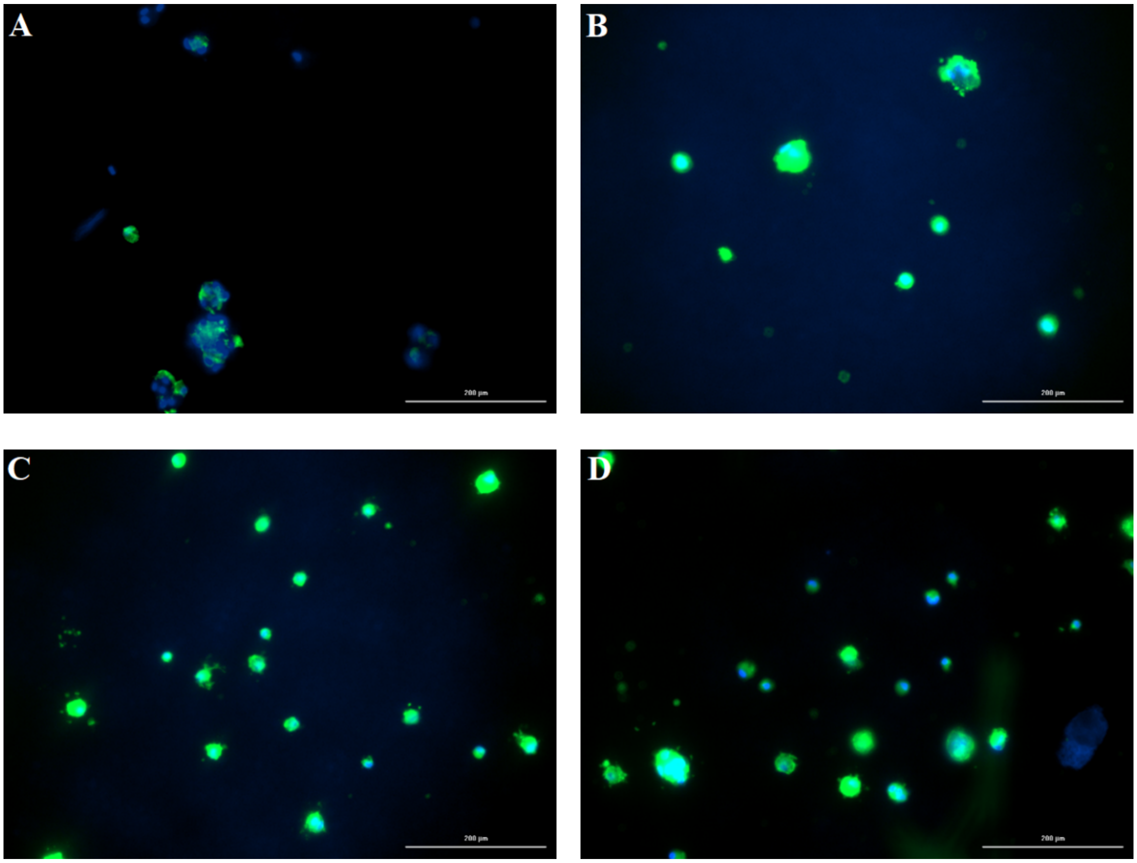

Figure 3.02. 2691MA Human ASM cells seeded on thin AG-10 hydrogels at varying densities (A) and (B) 10×10^3, (C) 20×10^3 and (D) 40×10^3 cells/cm^2. Rounded morphology and an absence of muscle-like filamentous actin network was observed in all cells. Magnification = 10×. Green = F-actin, Blue = Nuclei. Scale bar = 200 µm.

Comparatively, ASM seeded on our custom matrices, formulated using Novamatrix alginates of varying concentrations with 1 mg/mL collagen and 50 µM RGD-coupled-alginate to confer biocompatibility exhibited substantially improved morphology. Cells seeded at a density of 10×10^3 cells/cm^2 displayed conspicuous f-actin fibres, marked cell-cell connections, and a rapid increase in cell number. Further, there was a positive association between increasing collagen (2 mg/mL) and RGD-coupled-alginate (100µM) concentrations on cell-cell network formation (data not shown). Finally, on the stiffer alginates (2% SLG-20 and SLG-100), actin filaments appeared thicker, more prominent and reinforced, demonstrating a mechanical adaptation of subcellular structures to the composition of hydrogels (Figure 3.03).

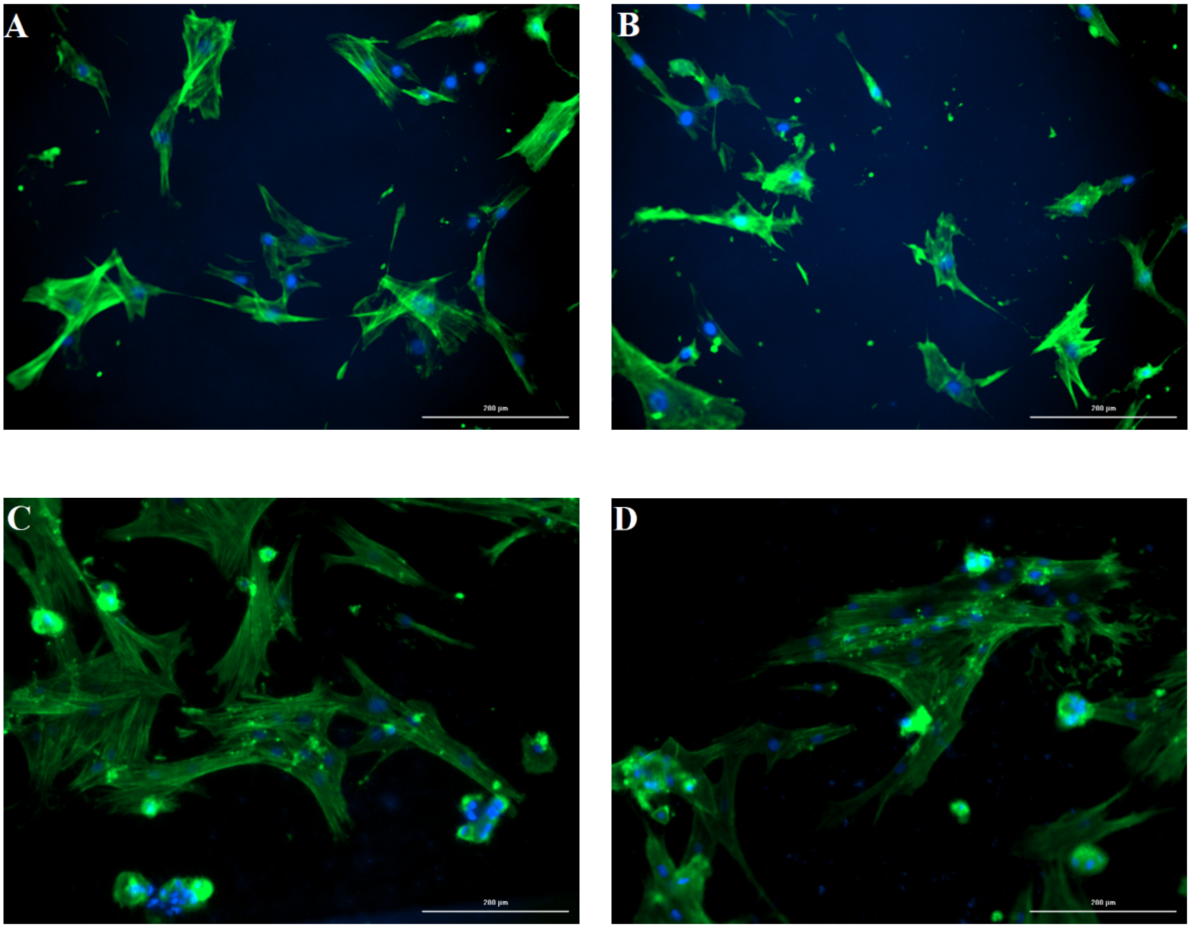

Figure 3.03. 2728M Human ASM cells on thin alginates from Novamatrix. Cells proliferated and spread out rapidly on both soft 0.5% SLM-20 (A & B) and stiff 2% SLG-100 (C & D) alginates. Magnification = 10×, scale bar = 200 µm.

Initial bio-ink characterization

After the initial pre-screening, I sought to characterize the bioprinting properties of different alginates. This was achieved by qualitative visual assessment of printing resolution, mechanical robustness, and fibre diameter of printed structures. I expected the manufacturer-supplied AG-10 matrix to print exceptionally well and/or be used as a supplement in our custom bio-ink formulation. However, consistent with the thin hydrogel results, I found the AG-10 matrix to perform poorly compared with alginates from Novamatrix (Figure 3.04 and 3.05). Specifically, AG-10 based constructs were exceedingly fragile, unravelled as soon as they were deposited on to the Thincert inserts, and exhibited no gross signs of a functional contractile tissue even after 7 days in culture. Microscopically, we observed an uneven distribution of cells and large clumps of matrix material in printed fibres. In addition, Hoeschst (All) and Propidium Iodide (Dead) staining revealed a very low percentage of viable cells (<10%). Finally, f-actin fibres displayed a rounded morphology several days after printing, indicating a lack of cellular maturation in these constructs. It was later discovered that we received several bad vials of AG-10, which are not representative of the typical commercial product (personal communication with Dr. West).

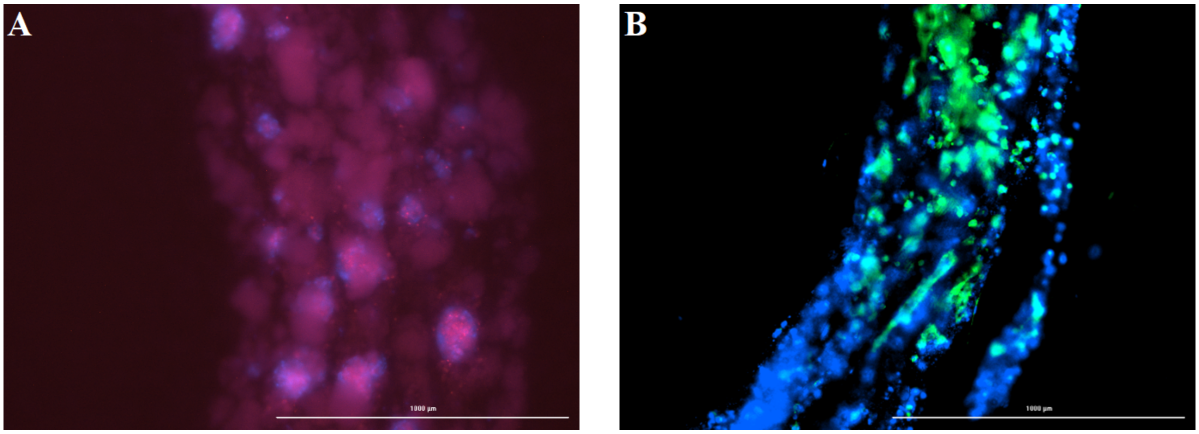

Figure 3.04. 2728M Human ASM cells printed with AG-10 matrix. Highly unorganized distribution of cells after printing. (A) Composite live/dead imaging 24 hours after printing. (B) F-actin staining reveals a lack of development of significant cell-cell connections. Clumps of matrix material and cellular aggregates can be observed. F-actin = Green, Live cell nuclei = Blue, Dead cell nuclei = Purple. Magnification = 4×, scale bar = 1000 µm.

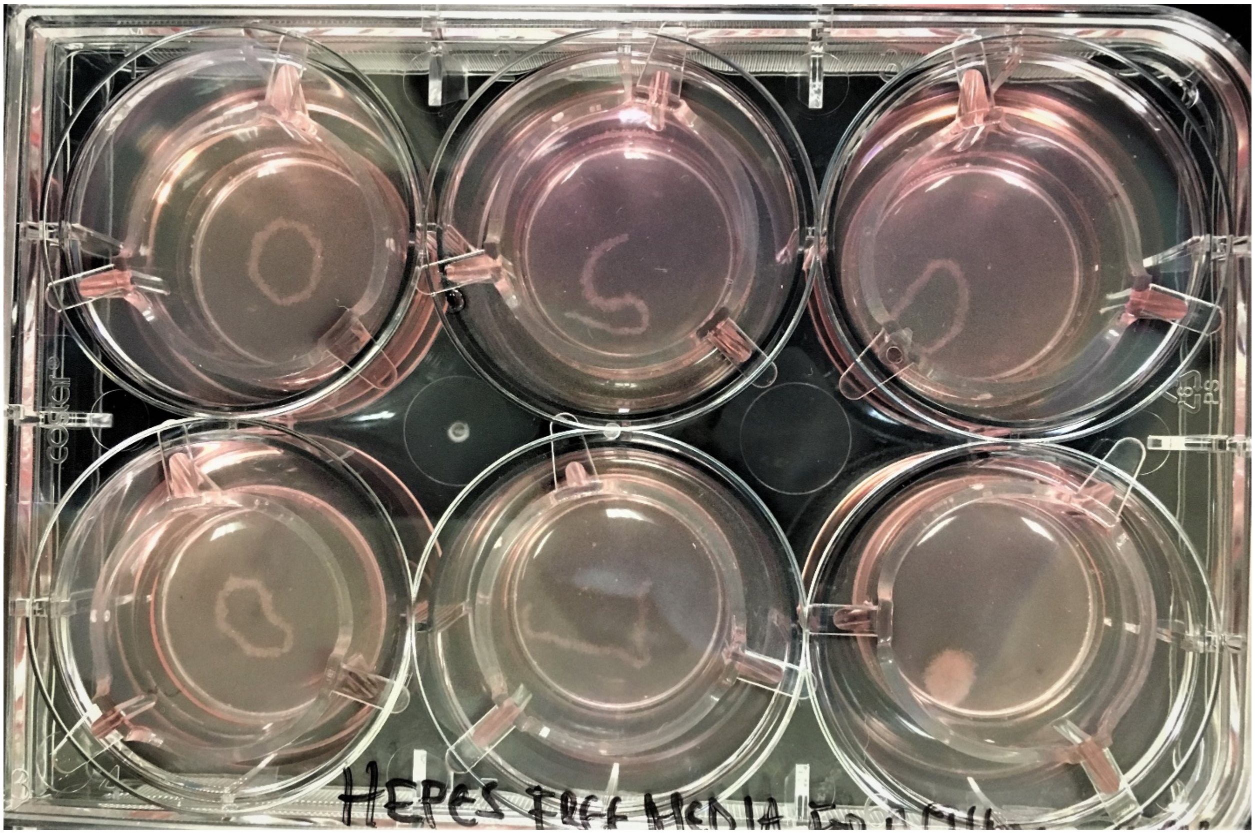

Figure 3.05. Macroscopic morphology of 2728M Human ASM cells printed using the AG-10 matrix. Constructs exhibited poor physical handling characteristics, failed to maintain shape fidelity and rapidly lost structural integrity, sometimes within minutes after printing. Fibre diameter was inconsistent between and within print runs.

Using alginate formulations from Novamatrix, I was able to successfully fabricate cell-free structures. Constructs printed using soft and stiff alginates displayed excellent printing resolution and maintained high material and shape fidelity after deposition. Importantly, the stiffer high-G alginates (SLG-20 and SLG-100) were mechanically robust and easily handled using forceps (Figure 3.06). These features, in conjunction with the promising results from the thin hydrogels, established the alginates from Novamatrix as a suitable platform for subsequent experiments and bio-ink optimization. However, high molecular weight alginates (SLG-100 & SLM-100) were excluded because their ultra-high viscosity made routine print runs problematic. Although the SLM-20 alginate had optimal viscosity properties for printing, it was also ruled out based on its low mechanical strength. Due to fewer crosslinked moieties, the low-G formulations require a very high alginate content to achieve similar mechanical properties as the high-G ones and are less likely to preserve structural integrity over long-term cultures. The SLG-20 alginate became a natural choice for all optimization experiments because of its printability and strength-to-concentration ratio. Further, we confirmed this alginate could easily be substituted by RGD-coupled-alginate to provide a more congenial micro-environment for the cells.

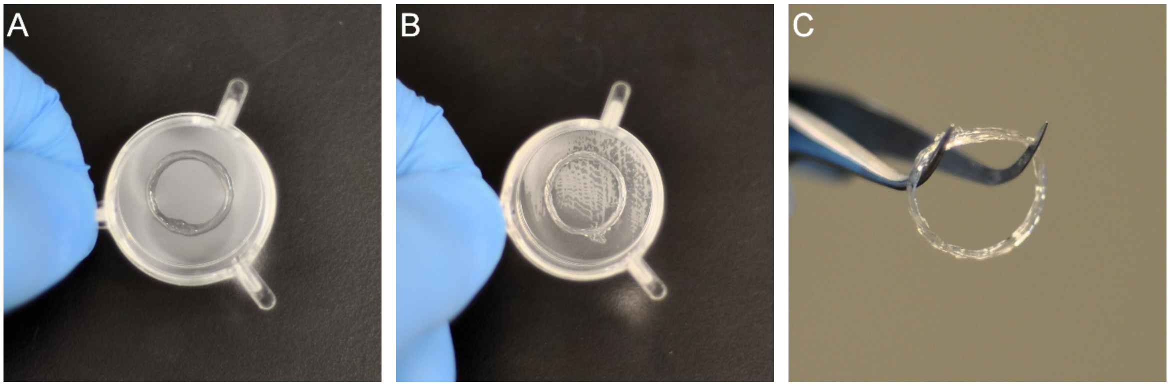

Figure 3.06. Acellular constructs printed using alginates from Novamatrix. (A) 0.5% SLM-20 (very soft), (B) and (C) 2% SLG-100 (very stiff). High resolution structures could be printed with both soft and stiff alginates.

Cellular constructs printed using 1% SLG-20 alginate supplemented with 1 mg/mL collagen exhibited robust mechanical properties and consistent fibre diameters (Figure 3.07). When viewed by brightfield microscopy, cells were organized in a solid and well-defined homogenous 3D ring structure, precisely following the computer aided design, with the profound absence of clumps or cellular aggregates. Dual fluorescent labelling 24 hours after printing with Hoechst/Propidium Iodide revealed a very high percentage of viable cells (>80%) (Figure 3.08A-B). This high cellular viability and mechanical stability was maintained for several weeks in culture.

Figure 3.07. Macroscopic morphology of 2691MA HASM cells printed with 1% SLG-20 alginate supplemented with 1mg/mL collagen. Structures exhibited excellent printing resolution, high shape fidelity and maintained structural integrity for weeks in culture.

Microscopic visualization at day 0 displayed evenly distributed cell nuclei, which were qualitatively present throughout a wide z-axis range, demonstrating the formation of a true 3D structure. Cells assumed a rounded or amorphous morphology, similar to that observed during the trypsinization and subculturing step performed prior to printing. During culture, only a few cells at the edges of constructs showed any morphological changes consistent with smooth muscle differentiation. This was confirmed by immunostaining at day 7, which revealed a highly organized, yet immature tissue (Figure 3.08C-D). F-actin staining revealed cells that appeared rounded and undifferentiated, in stark contrast to the thin hydrogels where extensive cell-cell network formation was observed using the same bio-ink formulation.

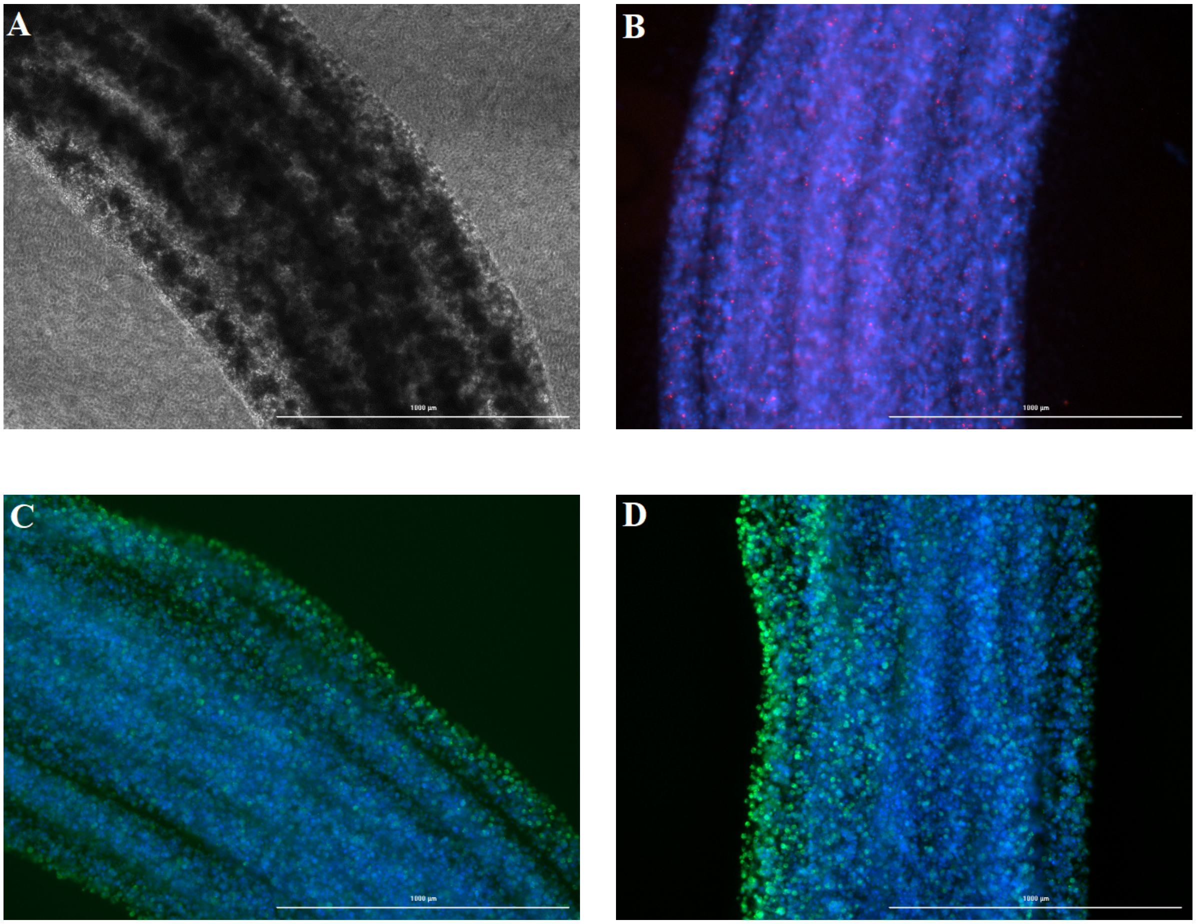

Figure 3.08. Representative microscopic (4×) features of a section of bio-ring printed using 2691MA HASM cells and 1% SLG-20 with 1 mg/mL collagen-I. (A) Brightfield imaging reveals a uniform distribution of cells in a three-dimensional axis (Background noise is 8.0 µm pores of ThinCert membrane). (B) Composite Live/dead imaging 24 hours after printing. (C) F-actin staining at day 0, show cells with a rounded morphology characteristic of smooth muscle after undergoing trypsinization and subculturing. (D) F-actin staining at day 7, cells retain round morphology and do not establish significant cell-cell contacts. Scale bar = 1000 µm.

Serum deprivation is known to induce cell-cycle arrest and drive ASM differentiation to a more contractile phenotype (166). To encourage phenotypic maturation in constructs, I substituted regular feeder with low-serum HEPES free media, with little effect on morphology and differentiation (data not shown). Moreover, we observed very little gross signs of compaction or matrix remodelling, with a notable absence of baseline tension development after several weeks in culture using 1% SLG-20 alginate. Thus, while Novamatrix alginates were capable of generating physically stable constructs that supported cell survival, the bio-ink formulation needed to be optimized to promote cell spreading, phenotypic maturation and contractile tone development.

Bio-ink optimization for ASM maturation in bare rings

High alginate concentrations are known to directly inhibit the ability of cells to spread out and remodel their micro-environment (167). Additionally, proliferation and differentiation of mesenchyme-derived cells has been directly linked to RGD content in alginate based matrices (168). Since I found a correlation between increasing collagen and RGD-coupled-alginate concentrations on cellular differentiation in the thin alginate hydrogels, I optimized our bio-ink formulations further by reducing the total alginate content, increasing the collagen concentration and substituting SLG-20 alginate with an RGD-coupled very low molecular weight alginate.

This strategy improved cell spreading considerably, albeit at the expense of mechanical stability (Figure 3.09). After a few days in culture all ASM tissues exhibited an inward collapse of the ring structure that was distinct from the unravelling and breaking of the ring seen with AG-10. Substantial expression of f-actin fibres was observed, however these were highly disorganized, with ASM cells seemingly remodelling the matrix in all directions without any signs of uniformity or alignment. This is typical of ASM cells developing contractile tone in a soft 3D environment without an opposing mechanical load (Figure 3.10).

Figure 3.09. Evolution of 2691MA HASM cells printed with 0.75% alginate (100µM RGD-alginate + 0.25% SLG-20) + 2mg/mL collagen. (A) After printing. (B) After 7 days.

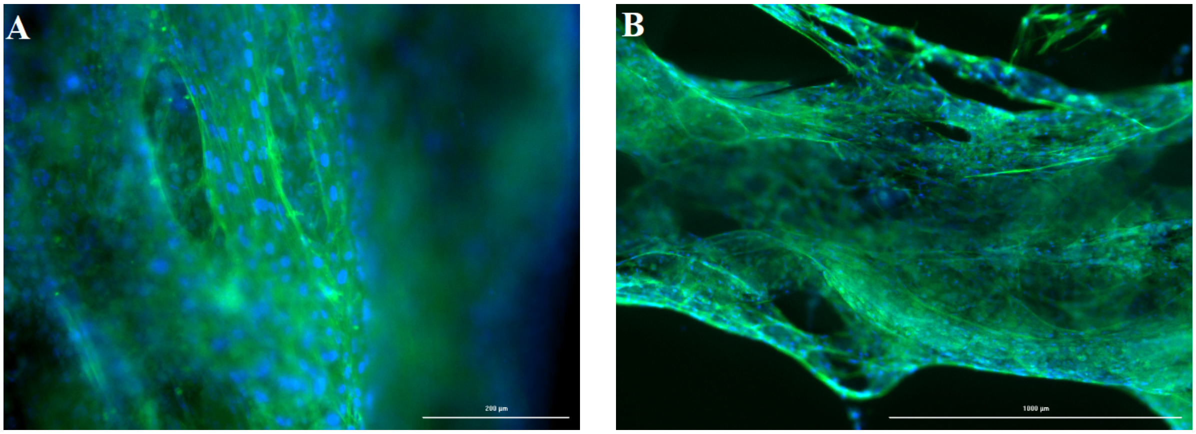

Figure 3.10. F-actin staining at day 7 of a section of 2691MA HASM cells printed with 100µM RGD-alginate + 0.25% SLG-20 + 2mg/mL collagen (A) 10× (B) 4×. Highly misaligned actin filaments can be observed. Scale bar = 200 µm (A) and 1000 µm (B).

3.3 Incorporating mechanical loads into the 3D tissue design

Several strategies were trialed to increase the structural stability of bioprinted constructs and to create a mechanical preload opposing muscle contraction, reminiscent of airway and parenchymal elements in native airways. *In vivo*, these mechanical loads have been implicated in the differentiation and maturation on normal ASM (169). This was achieved using the multi-material printing properties of our microfluidic bioprinter to alternately deposit cellular and acellular structural bio-inks.

The first attempt involved printing with a ‘Janus’ fibre where the cellular and acellular channels in the printhead are opened simultaneously to create a single continuous fibre. Each printed fibre becomes finely compartmentalized into distinct cellular and acellular sections, with the latter intended to provide structural support to the cells. The cellular layers were composed of 0.5% SLG-20, 0.25% RGD-alginate and 1 mg/mL collagen, while the acellular layers were composed of 1% SLG-20 with 1 mg/mL collagen. Aside from being extremely challenging to print, cells constructed with the Janus design did not show any typical signs of ASM maturation (data not shown). The second 'alternating ring’ approach involved optimization of the standard bio-ring design to include layers of acellular alginate fibres interspersed between the cellular layers. Although alternating ring constructs demonstrated enhanced structural integrity compared with bare rings and retained even distribution of cells and a high cell viability, cell maturation was very sparse (Figure 3.11). ASM cells failed to establish significant cell-cell connections with each other, f-actin fibres assumed a rounded morphology and were disorganized, and I found no signs of intrinsic tone development, lumen compaction or matrix remodeling.

A third strategy involved modifying the aspect ratio of the standard bio-ring. Instead of the design comprising 15 concentric layers stacked upwards along the Z-axis (15:1), I tested 5 concentric layers spread around three-axis (5:3). This was intended to make the construct wider and flatter, to give the cells more room to spread out and remodel the matrix, and to increase the compressive load as muscle cells pull inward. In theory, this would also curb any issues with nutrient diffusion to the cells at the innermost portions of the structure. However, this approach yielded similar results to the alternating ring design, with little evidence of cell spreading or network formation in these constructs (data not shown).

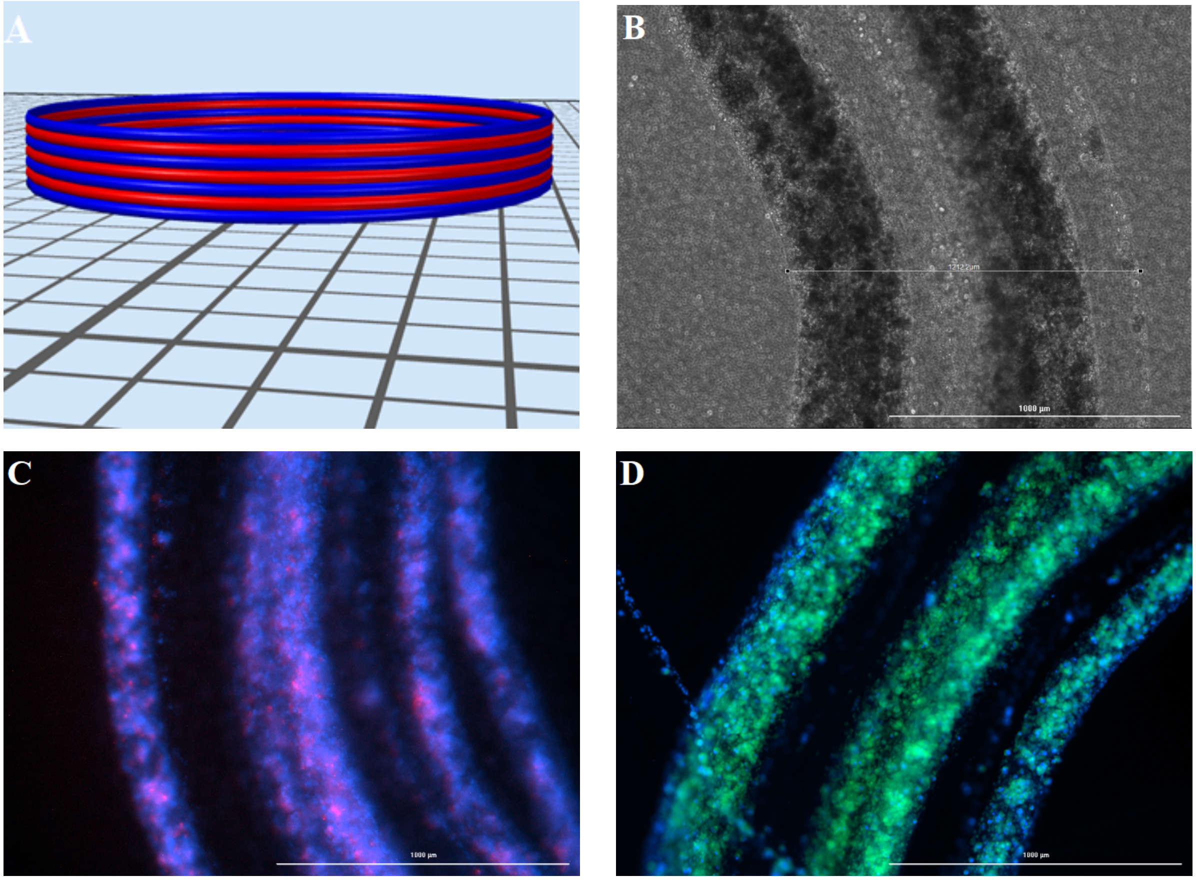

Figure 3.11. 2691MA HASM printed using the alternating ring design. (A) Schematic of tda file of alternating ring design with acellular layers (red) alternated between cellular layers (blue). (B) Brightfield imaging after printing showing cell dense layers visibly separated from acellular, demonstrating high fidelity of printed constructs. (C) Visualizing live/dead cells 24 hours after printing reveals a relatively good cell viability. (D) F-actin fibres had a round morphology after 7 days indicating a lack of cell spreading and poor formation of cell-cell contacts. Magnification = 4×, scale bar = 1000 µm

3D Sandwich

My next approach was to attempt uncoupling the muscle bundle from the structural component, by encapsulating the muscle entirely within an acellular structure. This would allow creation of a muscle bundle with lower concentrations of alginate that may promote tissue remodelling and cell spreading, while creating a strong mechanical framework. This 'sandwich' design consisted of 15 concentric cellular layers as per the original bio-ring, constrained by five top and five bottom layers of acellular alginate. The acellular layers extended beyond the edges of the muscle and were set to have alternating rectilinear and concentric infill patterns to generate a crosshatch pattern to increase contact points on the muscle and allow for easy diffusion of nutrients and waste products (Figure 3.12).

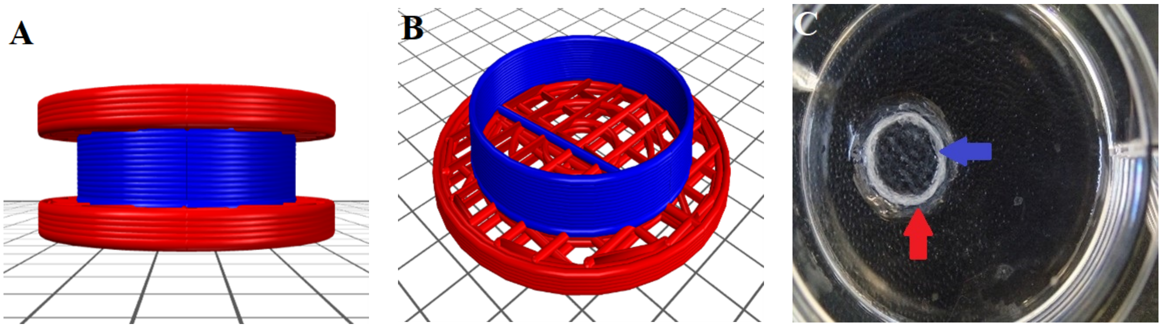

Figure 3.12. The sandwich model. Acellular layers are depicted red and cellular layers blue. (A) side and (B) top view of tda design. (C) Gross morphology of representative sanwiched ASM tissue after printing.

The sandwich design successfully enabled printing of cellular and acellular layers with widely different alginate stiffnesses, while maintaining excellent structural integrity in culture. With an acellular layer fixed at 1% SLG-20, cellular layers of 0.25 to 1.0% RGD-alginate were easily printable. With a cellular layer fixed at 0.25%, acellular layers of 0.5 to 2.0% SLG-20 could be used. Based on the significant mechanical stability and practical flexibility provided by the sandwich, it was used as the basis for all future bio-ink optimizations.

3D design	Objectives	Outcomes
Bare ring	Create a viable and mechanical stable ASM tissue with maximal cell spreading	High cell spreading and baseline tone, poor structural integrity
Janus	Increase mechanical strength of ASM rings	Good cell viability, lack of ASM maturation
Alternating rings	Implement a mechanical pre-load opposing ASM contraction	High cell viability, enhanced structural integrity, lack of ASM maturation
5:3 rings	Increase mechanical preload and curb nutrient diffusion issues	Good cell viability and structural integrity, lack of ASM maturation
Sandwich	Encapsulate cellular layers with top and bottom structural components	Increased cell viability and spreading. Baseline tone and markers of mature ASM phenotype

Table 3.02 Summary comparison of various iterations of the 3D physical design. An ideal design requires a delicate balance between viability, cell-cell network formation and structural integrity.

Sandwich bio-ink optimization

Within the practical constraints of the sandwich design an iterative design process was started to systematically optimize the composition of the cellular and acellular bio-inks (table 3.03 and 3.04). Including the stiff SLG-20 alginate (at any concentration) or high RGD-alginate concentrations (> 0.5%) in the cellular layer yielded results similar to the bare ring design, with an absence of cell spreading and tissue maturation (data not shown). However, using lower concentrations of 0.25 to 0.5% RGD-alginate enabled by the sandwich yielded dramatic improvements. Collagen at 0.5 to 2.0 mg/mL was an essential addition to the bio-ink; thermal gelling of collagen was essential in preventing unravelling of the constructs immediately after printing, improved cell spreading, and was deemed a necessary inclusion to match the natural composition of muscle.

To improve long-term stability of the constructs, inclusion of fibrin was investigated. While many ECM components can be degraded by MMPs secreted by ASM, fibrin breakdown is initiated by plasminogen and tissue plasminogen activator, which are not typically secreted by airway smooth muscle (170) or included in our bio-ink formulation. We systematically trialed fibrinogen concentrations up to 10 mg/mL and found an optimal concentration of 5 mg/mL, which was followed by post-printing treatment with 1.25 U/mL thrombin. Finally, the stiffness range of the acellular layers was set based on the practical limitations of printability. High alginate concentrations increased the viscosity of bio-inks, inevitably requiring higher pressures during the extrusion process than the bioprinter was capable of. Conversely, printing with lower alginate concentrations produced structures with poor resolution and were insufficient in supporting ASM tension development (not shown).

Cellular bio-ink component	**Optimal concentration**	**Effect of higher concentration**	**Effect of lower concentration**
AG-10	None; unsuitable	N/A	N/A
SLG-20	0%	≥ 0.1%, reduced cell spreading	N/A
RGD-alginate	0.375%	> 0.5%, reduced cell spreading	≤ 0.25% Reduced cell viability, poor printability
Collagen	1.0 mg/mL	≥ 1.5 mg/mL; no additional benefit, takes up ‘space’ in bio-ink	0 mg/mL; increased unravelling of constructs after printing
Fibrinogen with thrombin post-treatment	5 mg/mL	≥ 10 mg/mL; no benefit, takes up ‘space’ in bio-ink	0 mg/mL reduced long-term structural integrity

Table 3.03. Summary of tested cellular bio-ink components, and optimal concentration when used within the sandwich design. The standard cellular bio-ink contained 0.375% RGD-alginate, 1.0 mg/mL collagen and 5.0 mg/mL fibrinogen. Constructs were post-treated with thrombin for fibrinogen polymerization to fibrin.

Acellular bio-ink component	Optimal concentration	Effect of higher concentration	Effect of lower concentration
AG-10	None; unsuitable	N/A	N/A
SLG-100	None, poor printability	N/A	N/A
SLG-20	0.75 – 1.25%	≥ 1.5% usable, but difficult to print	≤ 0.50%, poor printability, poor structural integrity
SLM-100	None, poor printability	N/A	N/A
SLM-20	None, poor strength to concentration ratio	N/A	N/A
Collagen	1.0 mg/mL	≥ 1.5 mg/mL; no benefit, takes up 'space' in bio-ink	0 mg/mL; increased unravelling of constructs after printing
Fibrinogen with thrombin post-treatment	5 mg/mL	≥ 10 mg/mL; no benefit, takes up 'space' in bio-ink	0 mg/mL reduced long-term structural integrity

Table 3.04. Summary of tested acellular bio-ink components, and optimal concentration when used within the sandwich design. The standard acellular bio-ink contained 0.75% to 1.25% SLG-20 alginate, 1.0 mg/mL collagen and 5.0 mg/mL fibrinogen and was post-treated with thrombin for fibrinogen polymerization to fibrin.

ASM characteristics within basal bio-ink formulation

After all optimization steps, the default ASM tissue was comprised of: 1) a 3D Sandwich design; 2) Cellular bio-ink: 0.375% RGD-alginate, 1.0 mg/mL collagen, 5.0 mg/mL fibrinogen; 3) Acellular bio-ink: 1.0% SLG-20 alginate, 1.0 mg/mL collagen, 5.0 mg/mL fibrinogen and 4) Thrombin post-treatment.

Using this default tissue design, I characterized ASM behavior and observed spontaneous compaction of constructs, manifesting as an unstimulated reduction in lumen area, beginning a few hours after printing and proceeding over several days. This is suggestive of the development of baseline tension. The top and bottom acellular layers of the sandwich successfully opposed this increasing tension. ASM tissues were switched to low serum ITS media 48 hours after printing, structural integrity was maintained for more than a week in culture. During this time cells markedly remodelled the matrix and established significant cell-cell connections (Figure 3.13). Over time, cells tended to elongate at an almost perfect alignment, parallel to the axis of printing deposition and tension devlopment. The degree of alignment of f-actin fibres was quantified with the directionality plugin for ImageJ, which revealed an exceptionally uniform orientation in filaments. This high degree of alignment was also maintained at different layer-heights in the interior of constructs. LDH assays performed 48 hours after printing suggested a low cellular cytotoxicity, with cells cumulatively releasing an average of 34.3% of the LDH activity of Triton X-100 100% lysis controls (Figure 3.14). Live/dead visualization confirmed a majority of cells (>80%) remained viable for up to 7 days after printing (Figure 3.15).

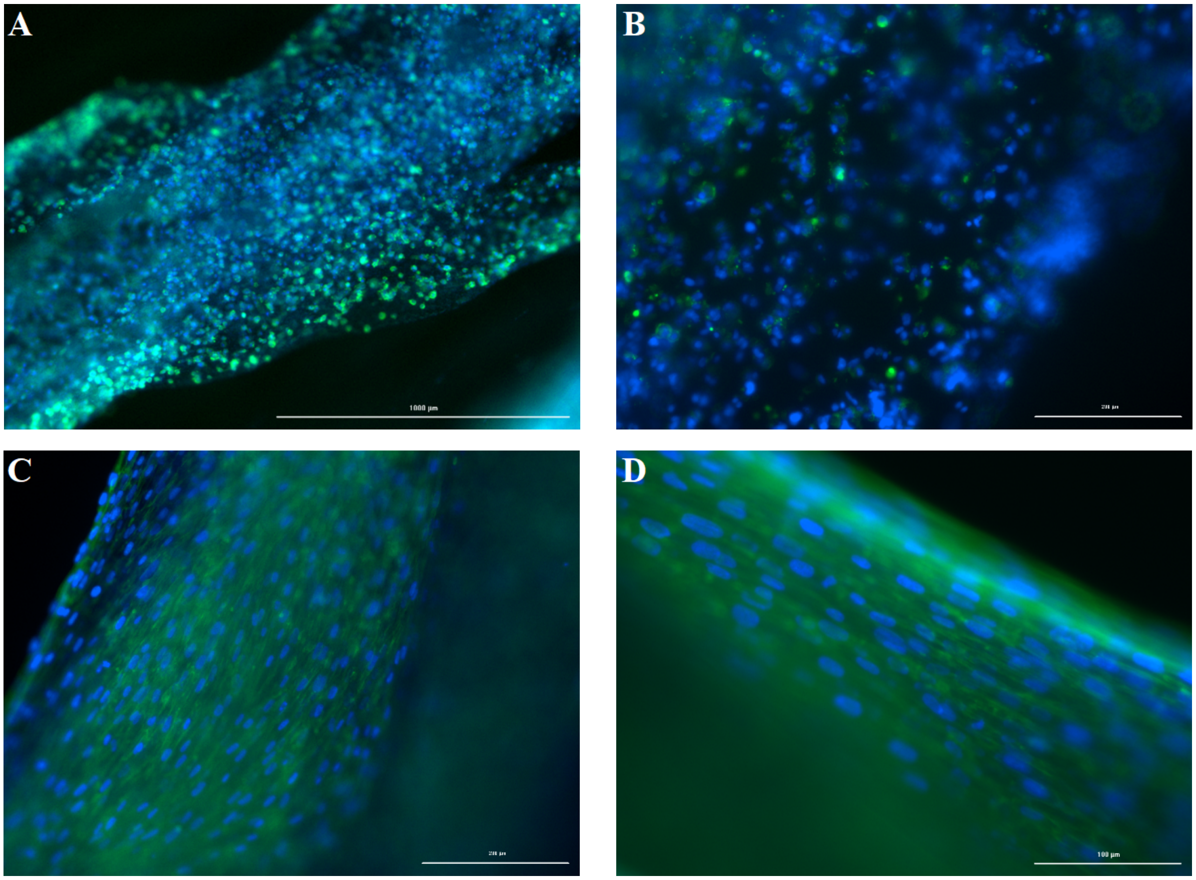

Figure 3.13. Temporal evolution of D12s in 3D sandwich. No significant cell-cell contacts after printing at day 0 (A) 4× (B) 20×. In contrast, after 4 days, prominent and highly organized f-actin expression with homogeneous nuclei distribution can be observed. This syncytial arrangement is essential for force generation (C) 10× and (D) 20×. Scale bar = 1000 µm (A), 200 µm (B-C) and 100 µm (D).

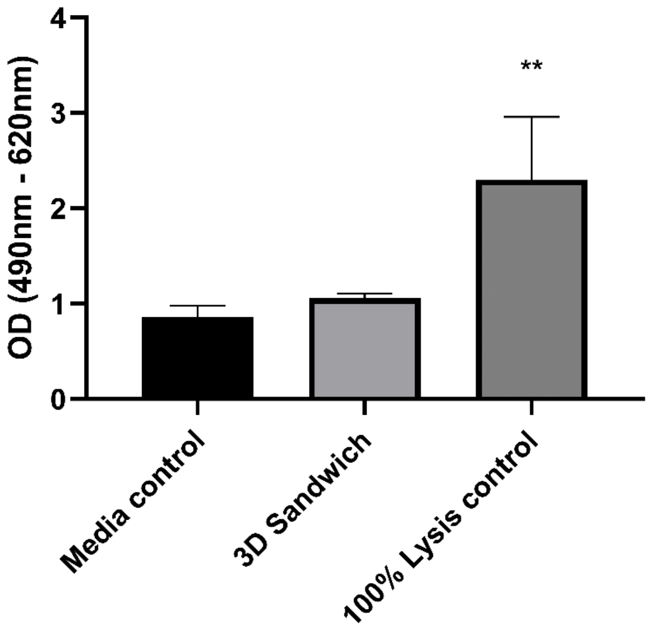

Figure 3.14. Cellular Cytotoxicity. One-way ANOVA revealed statistically significant elevated levels of LDH activity in the 100% lysis control compared with media control and 3D sandwiches (p = 0.0075).

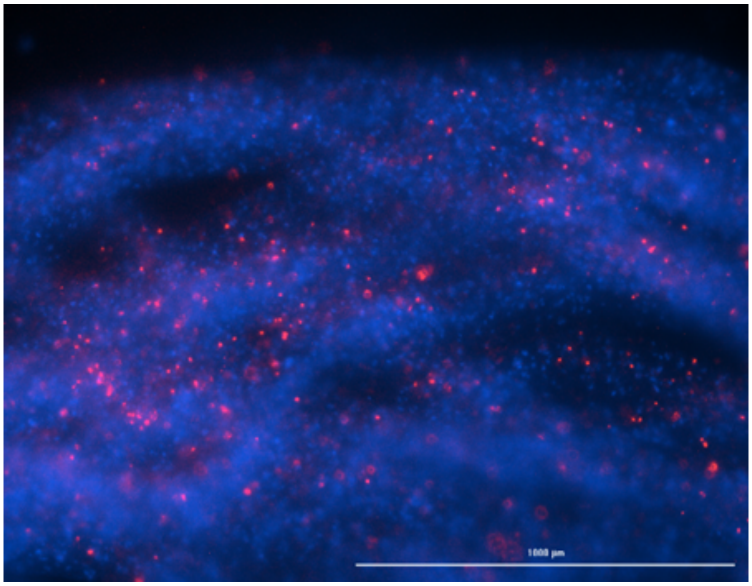

Figure 3.15. Cell viability in sandwich. Representative image of Live (Hoechst, blue) and dead (propidium iodide, red) cell staining at 24 hours indicating most cells remained viable. D12 cells were printed using the basal sandwich design and ink components. Magnification = 4×, scale bar = 1000 µm.

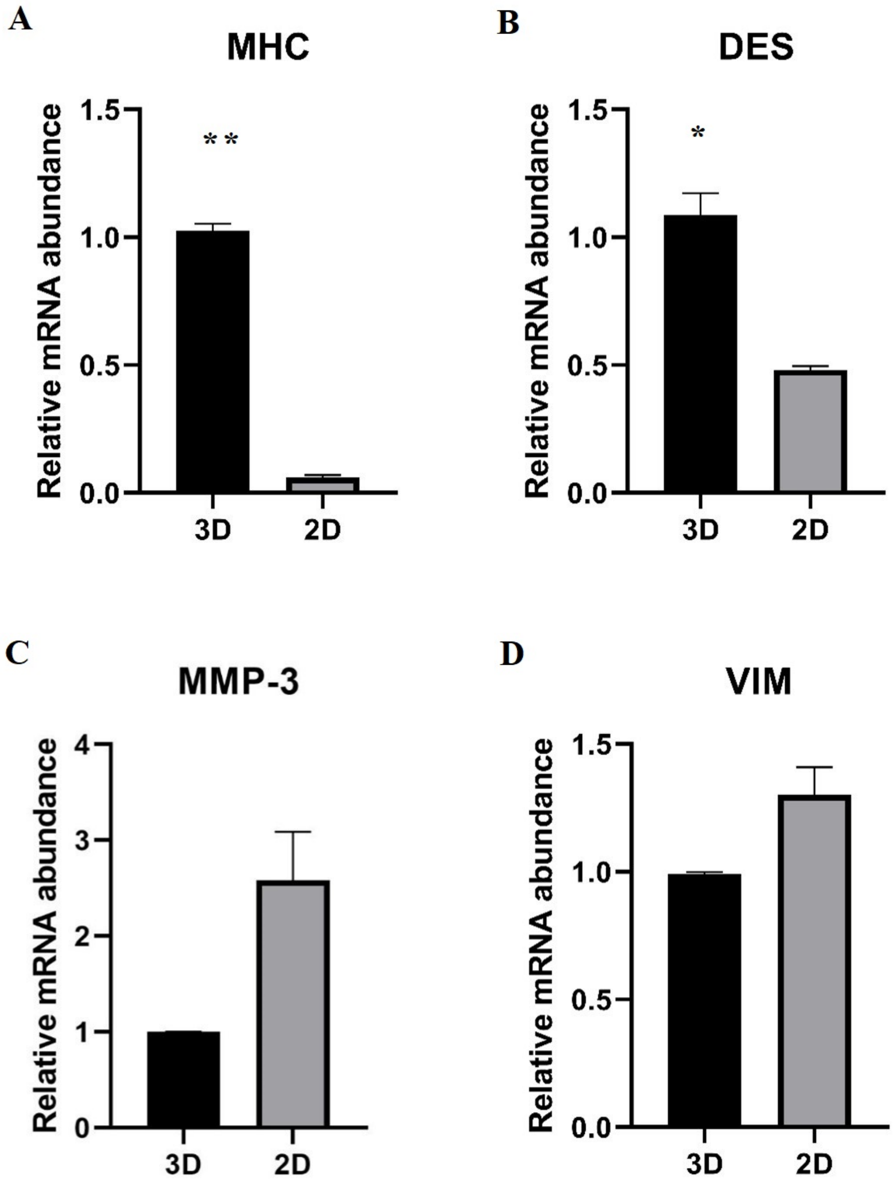

Figure 3.16. mRNA quantification of select genes in 3D sandwich vs 2D cell cultures using 2691MA HASM cells. RNA samples were isolated using the CTAB (3D) and Purelink (2D) techniques, 24 hours after printing or seeding. Data are normalized to the housekeeping gene GAPDH, as mathematical algorithms found it to be the most stable in these cells. Relative mRNA for (A) MHC, (B) DES, (C) MMP-3 and (D) VIM were calculated using Equation 2.03. Statistically significant elevated levels of contractile genes in 3D, however pro-synthetic genes trended lower compared to 2D (n = 2).

Compared with standard 2D cultures, cells in the 3D sandwich had a higher mRNA abundance of pro-contractile genes, including myosin heavy chain (MHC) ($p = 0.0008$) and desmin (DES) ($p = 0.0203$). There was a consistent trend towards lower mRNA levels of pro-remodeling genes vimentin (VIM) ($p = 0.0875$) and matrix metalloproteinase-3 (MMP-3) ($p = 0.1057$) in 3D, although the differences were not statistically significant (Figure 3.16). Collectively, these data suggest ASM phenotype is regulated by substrate geometry, consistent with previous studies (103,130).

Based on these promising results, the sandwich design and optimal bio-ink formulation were deemed suitable for ongoing experimentation to determine the effect of tissue stiffness on ASM function.

Chapter four: Results — Evaluating ASM contractile function in 3D

In asthma, airway remodeling triggers structural and mechanical changes that may contribute to disease pathogenesis/exacerbations by altering ASM contractile function. However, only a few studies have directly examined the precise effects of mechanical factors using viable human tissue. To simulate the mechanical changes seen in asthma, I fabricated realistic ASM tissues of varying stiffnesses by controlling alginate concentrations in acellular layers of 3D sandwiches. ASM physiological responses were evaluated based on baseline tone, contraction/relaxation responses to pharmacological agents, and contractile gene expression.

4.1 Baseline tension

As a measure of baseline tension development, I tracked unstimulated reduction in lumen area in ASM tissues fabricated across a stiffness range (Figure 4.01). Within 24 hours in feeder media, D12 ASM tissues printed with 0.75% acellular alginate contracted without stimulus to an average of 80.0% (± 1.3%) of initial area, while those printed with 1% and 1.25% contracted to an average of 86.7% (± 1.2%) and 86.8% (± 1.5%) respectively. Conversely, ASM tissues printed without acellular supports were excluded from contraction experiments and statistical analysis as they compacted to an average of 22.8% (± 5.6%) after 24 hours and shrunk excessively after that, making accurate lumen area measurements impossible.

In these experiments, regular feeder media was changed to low serum ITS media 48 hours after bioprinting, and the cells were cultured for an additional 4 days. By day 6, the 0.75%, 1% and 1.25% constructs had contracted further without stimulation to 72.3% (± 2.6%), 78.4% (± 1.8%) and 74.0% (± 4.4%) of their initial lumen areas, respectively. Such spontaneous development of baseline tone during ASM maturation is a distinct phenomenon from the agonist-induced contraction seen in mature muscle (171). Two-way ANOVA revealed statistically significant differences in the row (time) and column (stiffness) factors, however Tukey's multiple comparisons test was unable to determine which groups differed specifically.

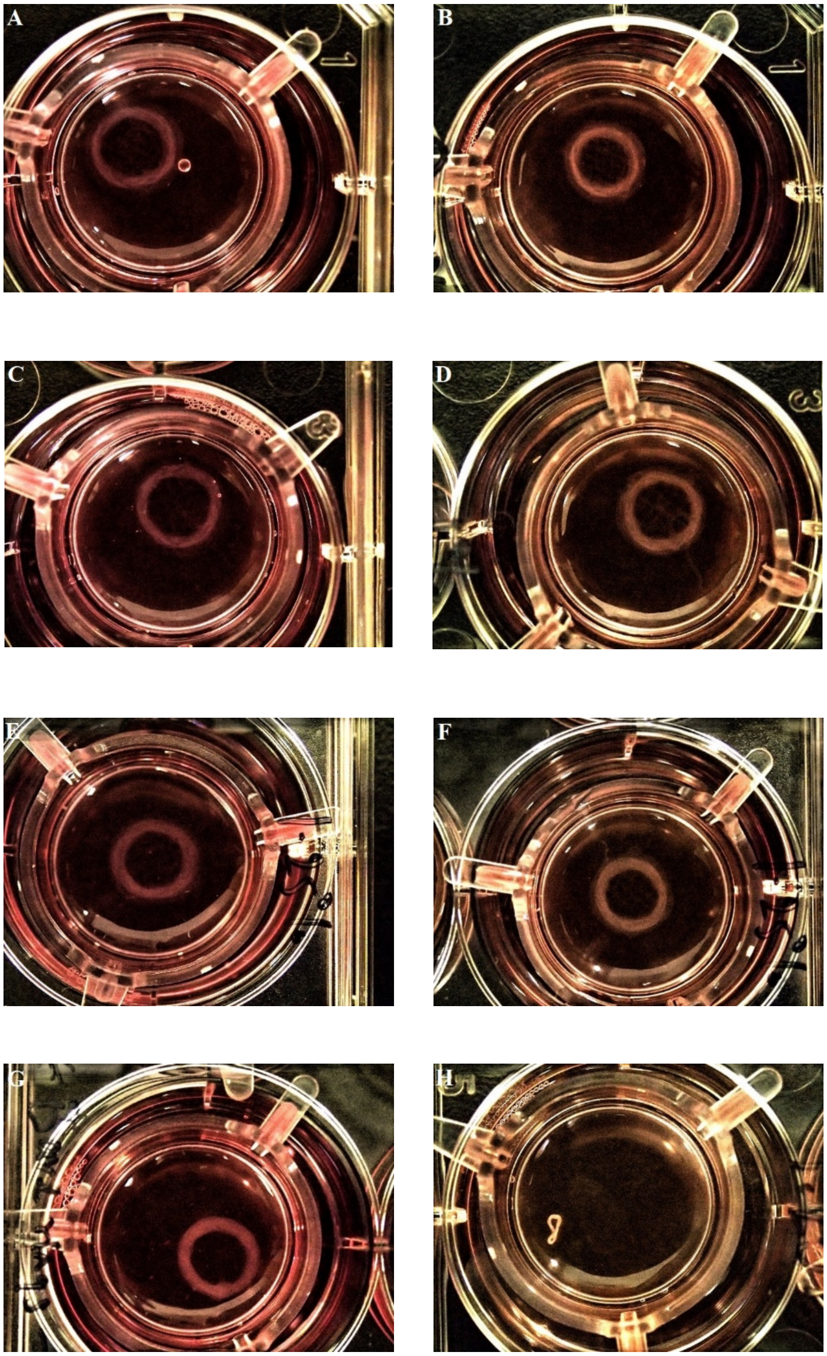

Figure 4.01. ASM tissues fabricated with varying acellular stiffnesses. Constructs with acellular supports maintain structural integrity more than a week after printing: 0.75% (A) After printing, (B) Day 6, 1% (C) After printing, (D) Day 6, 1.25% (E) After printing, (F) Day 6. In contrast, excessive tension development in the bare rings results in a significant reduction in lumen area (>75% after 24 hours) and loss of mechanical stability: Bare ring (G) After printing, (H) 48 hours.

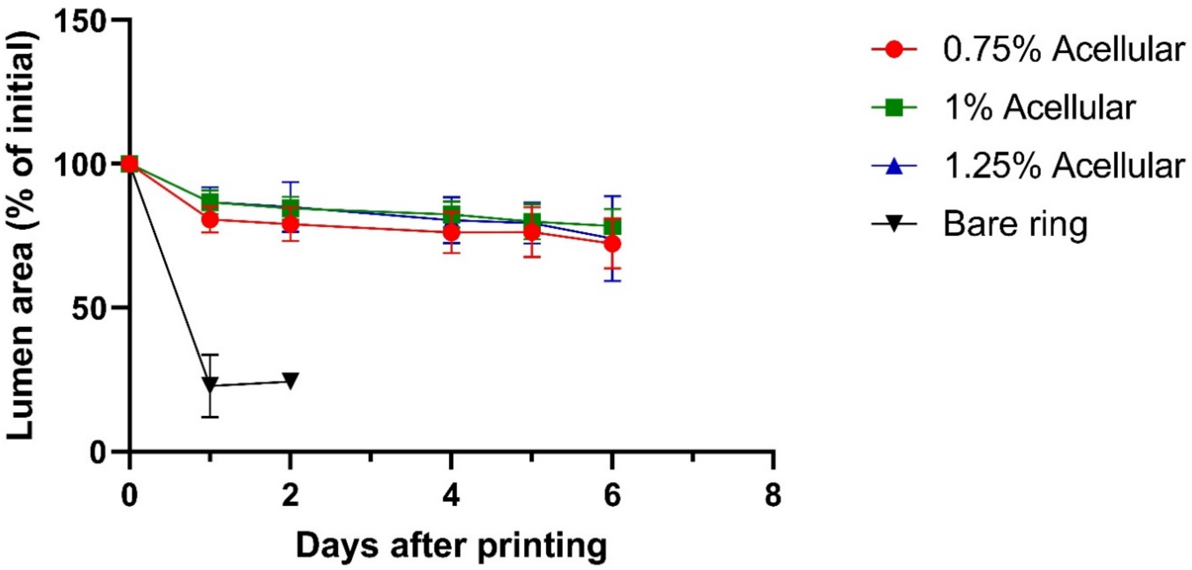

Figure 4.02. Unstimulated contraction of muscle rings from day 0 to day 6 post printing. Two-way ANOVA interaction p = 0.7504, stiffness p <0.0005, time p <0.0001 (n = 12). Tukey-Kramer post-hoc test did not find any statistically significant differences between the stiffness groups trialed. *Bare rings are included for comparative purposes only but are excluded from statistical analysis.

4.2 Drug testing

To assess functionality of ASM tissues and characterize the dynamics of agonist-induced stimulation, a dose-response curve to acetylcholine chloride (10 nM – 100 μM) was created and measured as percent reduction in internal lumen area from pre-treated baseline. Acetylcholine is a well-known bronchoconstrictor that induces ASM contraction by activating M3 muscarinic receptors on the cell surface, leading to an intracellular flux of calcium ions, which subsequently activates the muscle's contractile apparatus (172). Agonist-concentration-response curves were constructed and analyzed using non-linear regression (curve-fit) in GraphPad Prism. I found a concentration-dependent reduction in lumen area in day 7 ASM tissues bioprinted with the basal sandwich design (1% acellular alginate), which contracted to a mean value of 93.9% of pre-treated lumen area after the final 100 μM dose of acetylcholine was administered. This dose was chosen based on previous reported values from mice, guinea pig and human PCLS, which showed maximal ASM stimulation by acetylcholine to occur in the range of 0.1-1 μM (173,174). The reduction in lumen area started at a dose of about 100 nM and best-fit value for the EC_{50} calculated using the Hill's equation was 15.26 μM, demonstrating a lower but comparable sensitivity to reported values from ASM strips isolated from rats and rabbits (175,176). However, it is quite clear that the calculated EC_{50} value would likely be higher since a larger dose would be required to achieve a maximal plateau of ASM contraction in 3D sandwiches. The observed lower sensitivity could also result from the large diffusion barrier constituted by the acellular layers.

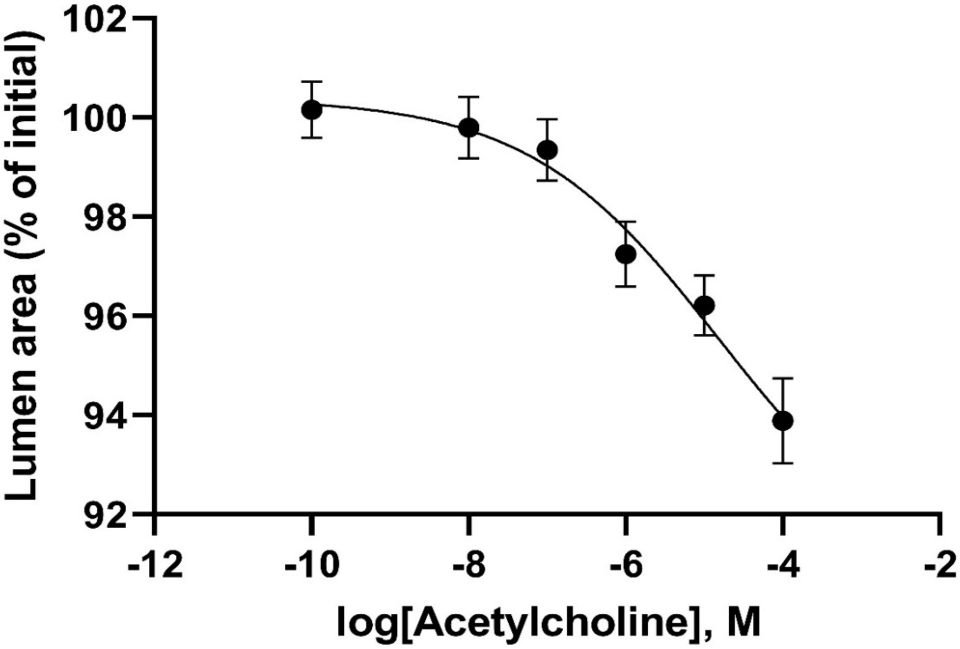

Figure 4.03. Log concentration-response curve for acetylcholine (n = 2, $logEC_{50}$ = -4.816 M).

The physiological responses of ASM tissues to a panel of contractile and relaxant agents were determined by recording lumen area values before and after drug treatments. ASM tissues printed across a stiffness range (n = 10) responded to all drugs tested (two-way ANOVA interaction p = 0.5524, drug responses $p < 0.0001$, stiffness p = 0.0438). An assumed maximal dose of acetylcholine (100 μM) gave a mild contractile response, decreasing lumen areas to an average of 91.5% (± 2.3%), 97.4% (± 1.5%) and 94.8% (± 2.0%) of 100% initial pre-contracted baseline values in ASM tissues printed with 0.75%, 1% and 1.25% acellular layers respectively. KCl caused a much stronger contractile response, decreasing lumen areas of tissues printed with 0.75% to an average of 86.7% (± 3.0%), while the 1% and 1.25% tissues shrunk to 93.0% (± 2.0%) and 86.4% (± 3.2%) of initial area, respectively.

Interestingly, cytochalasin D was able to cause a sharp decrease in lumen area after KCl treatment to 96.1% (± 2.1%), 97.2% (± 1.8%) and 95.7% (± 2.9%) in 0.75%, 1% and 1.25% constructs respectively. However, the failure to completely reverse contraction-linked decreases in lumen area is surprising. Cytochalasin D is known to disrupt the actin cytoskeleton and should cause maximal tension ablation (177), but this was not observed. It may be possible that alternate relaxation agents such as beta-agonists (e.g., formoterol and albuterol), forskolin or ROCK inhibitors may help induce additional relaxation to elucidate the mechanisms underpinning tone development. That said, cytochalasin D data could also indicate that while the mechanical load presented by the acellular matrix can prevent excessive compaction during maturation, it only provides a weak elastic load with limited ability to 'pull back' on tissues.

Nevertheless, the observed relaxation demonstrates a considerable level of actino-myosin dependent force generation after acetylcholine and KCl treatment. Although the maximal responses to acetylcholine were noticeably less than KCl, this is still remarkable because ASM cells are known to express reduced levels of muscarinic receptors *in vitro*, ultimately reducing their responses to acetylcholine (178). The rapid time course of contraction and relaxation is also noteworthy, as bioprinted tissues were able to respond to administered drugs significantly faster than contraction assays using bulk collagen gels that usually take up to 60 minutes to reach maximal contraction (179,180).

Although, post-hoc comparisons did not reveal which stiffness group pairs exhibited the most discrepancy in contractile responses, tissues fabricated with 0.75% and 1.25% acellular layers consistently contracted similarly to and substantially more than those printed with 1% acellular layers. This difference in contractile responses across the stiffness range trialed may provide the first evidence for mechanical regulation of ASM cellular function by the mechanical environment in a 3D model. However, it is important to consider that these results are calculated from baseline levels immediately prior to contraction which are different, and do not account for differential levels of tissue compaction that may have occurred during tissue maturation.

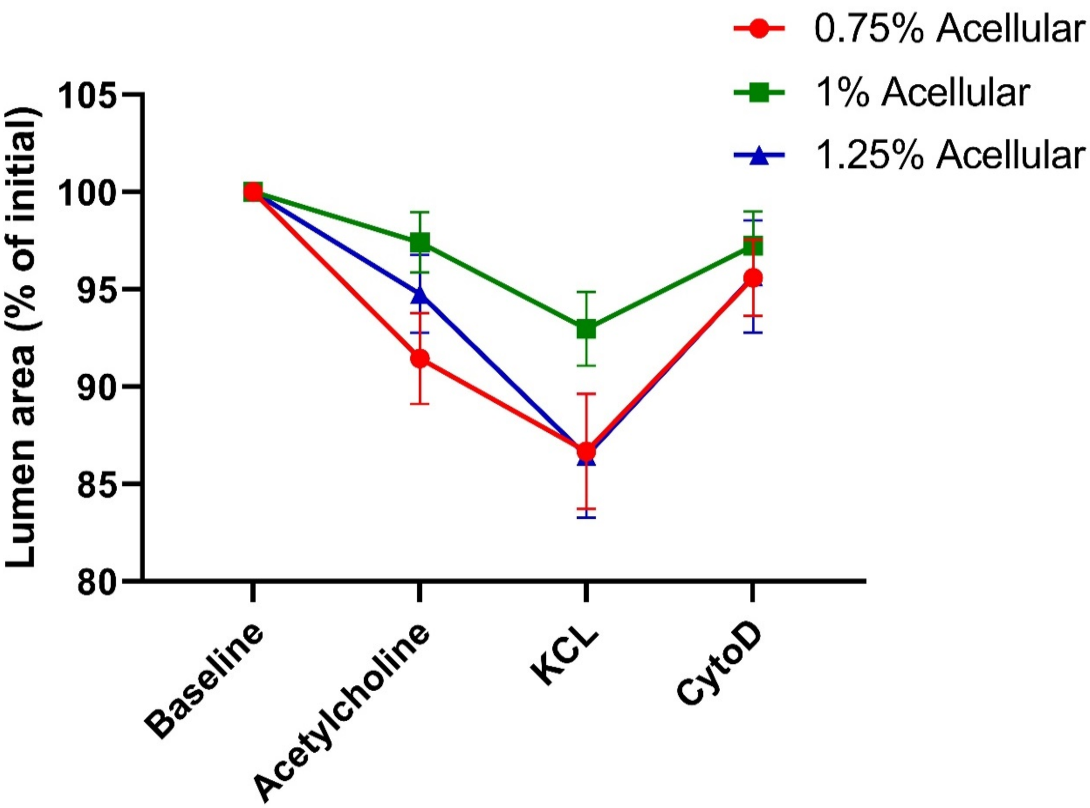

Figure 4.04. Contraction of day 6 ASM tissues. ASM tissues printed across a stiffness range exhibited a mild contractile response to acetylcholine from pre-contracted baseline levels, and a substantially stronger response to KCl. Whereas disruption of the actin cytoskeleton with cytochalasin D increased lumen areas near baseline levels. Stiffness modulation of contraction was statistically significant, although post-tests did not reveal individual group differences (two-way ANOVA interaction $p = 0.5524$, drug responses $p < 0.0001$, stiffness $p = 0.0438$, n=10). *Some error bars overlap due to icon sizes.

4.3 Acellular load removal

The initial length of smooth muscle contractile filaments and consequently its ability to shorten are highly dependent on the mechanical preload (47). In 3D bioprinted tissues, preload is represented by the forces exerted by the acellular structure as it opposes muscle contraction. To evaluate the strength of the preload relative to the baseline tone generated during tissue maturation, I exposed constructs printed with 0.75%, 1% and 1.25% acellular layers to a citrate + EDTA alginate decrosslinking solution. Within the first 5 minutes, I observed a sharp reduction of lumen area in constructs fabricated with 0.75%, 1% and 1.25% alginate. Shortening proceeded slowly thereafter, and by 10 minutes, the 0.75%, 1% and 1.25% tissues had contracted to 44.9% (±

11.8%), 45.3% (± 12.5%) and 51.5% (± 14.0%) of initial lumen areas, respectively. This may be indicative of a typical logarithmic plateau for contraction. It may also represent a biphasic shortening response consistent with previous studies that have identified two subsets of ASM cross-bridges regulating unloaded shortening velocity. These are fast cross-bridges that cycle rapidly and characterize the early phase of muscle contraction, followed by slow cross-bridges, which develop due to latch mechanisms in the muscle and cycle much more slowly (181). Two-way ANOVA revealed significant contraction in the time statistic, however there was no significant difference in the magnitude of contraction between different tissue stiffnesses (interaction $p > 0.9999$, time $p < 0.0001$, stiffness $p = 0.1529$). Collectively with cytochalasin D results from above, this indicates that the acellular structure provides an extremely strong mechanical preload opposing contraction, but the structure is only partially elastic when contractile force is removed.

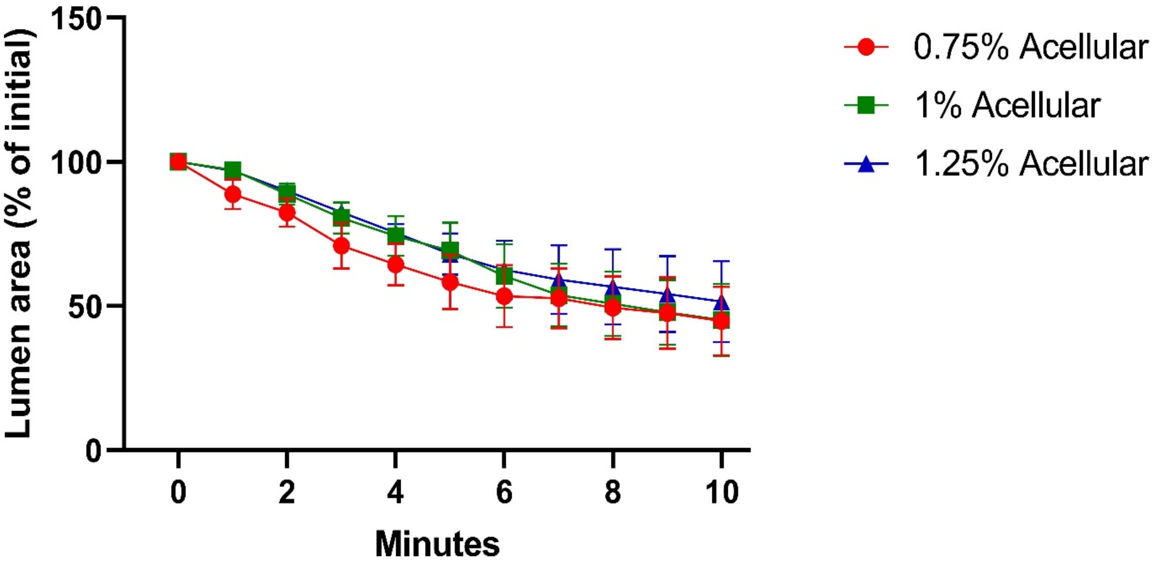

Figure 4.05. Unloaded shortening of ASM tissues. 0.75% ASM tissues shortened consistently faster than those printed with 1% and 1.25% acellular layers at every time point measured, although this effect was not statistically significant. Any increased contraction in the 0.75% constructs may be a result of the acellular layers being able to depolymerise faster, or an intrinsic property of the muscle (two-way ANOVA interaction $p > 0.9999$, time $p < 0.0001$, stiffness $p = 0.1529$ $n \geq 3$). *Some error bars overlap due to icon sizes.

4.4 RNA isolation

To characterize the phenotype of airway myocytes in bioprinted constructs, extraction of sufficient quantities of high-quality RNA from the alginate-based matrix was required. This is typically challenging, because alginate can be co-isolated with the RNA, which ultimately affects the quality of the sample. I evaluated recovered RNA from several commercially available isolation techniques in terms of purity (from A_{260}/A_{280}), and total RNA yield (from A_{260}).

Overall, the TRIzol extraction technique yielded the highest apparent total RNA yield (38.7 ± 10.1µg, n = 12). However, RNA purity assessed by A_{260}/A_{280} ratios was poor (1.4 ± 0.1), indicating high contamination with either alginate, residual phenol, or other organic solvents associated with the extraction, so yield was likely over-estimated (Figure 4.06). The Plant RNA Isolation Reagent returned a good yield (5.3 ± 0.9µg, n = 12) and purity (2.1 ± 0.2) but was excluded based on its cumbersome method and because recovered RNA exhibited a significant amount of variance, with only about 50% of samples having A_{260}/A_{280} ratios at acceptable levels. RNA yield was lowest (0.5 ± 0.1µg) using the Purelink technique. Although purity was slightly better than the previous methods (1.9 ± 0.1), this technique was also excluded because it consistently failed to return enough RNA material required for downstream qRT-PCR reactions. Importantly, the GeneJET Kit and CTAB techniques yielded ratios in the desired range (2.0 ± 0.1), suggesting these samples were consistently less contaminated by salts and/or polysaccharides.

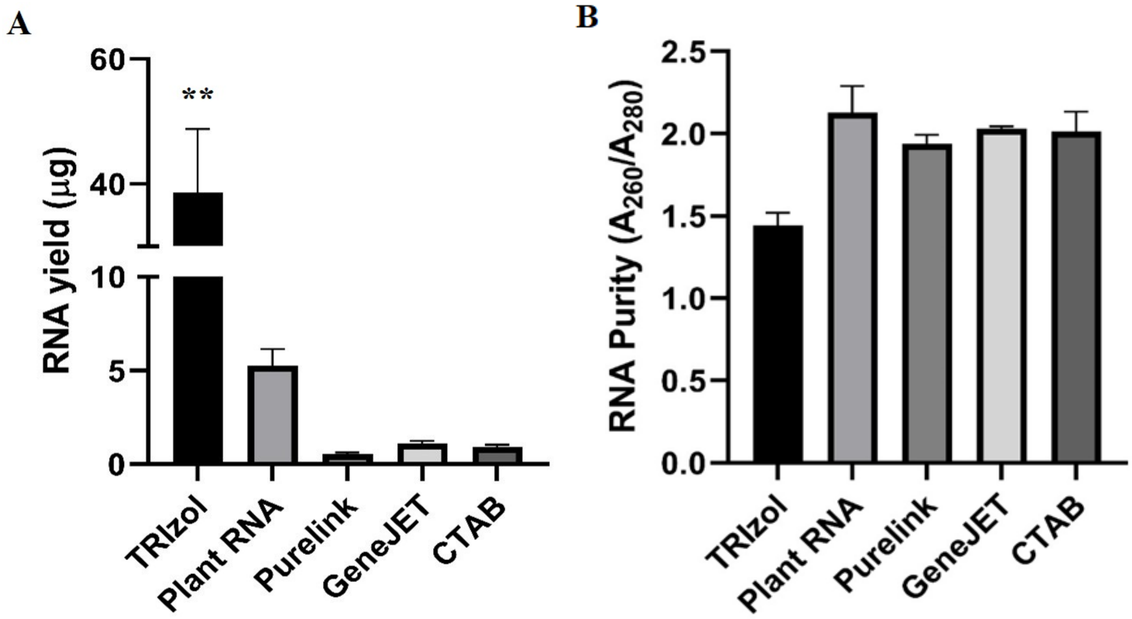

Figure 4.06. Summary of various RNA isolation techniques trialed. (A) RNA yield. RNA was extracted from samples 48 hours after bioprinting with various isolation techniques. RNA yield was calculated by multiplying RNA concentration with total eluted volume. (B) Purity of isolated RNA. One-way ANOVA revealed significant differences in RNA yield between TRIzol and the other methods trialed ($p < 0.0001$) (n=12).

It is worth mentioning that the inclusion of a purification step using Purelink spin columns after the TRIzol protocol was able to increase sample purity, but with compromised yields (data not shown) and increased complexity and cost. Collectively, these results show that GeneJET and CTAB methods perform well on our alginate-based samples, with similar or better outcomes than conventional 3D-RNA isolation techniques (182). However, due to the laborious and time-consuming nature of the CTAB technique, I ultimately chose to isolate RNA samples using the GeneJET kit for evaluating ASM contractile phenotype. In addition to consistency, the latter method offered an easy-to-use spin column format.

4.5 Phenotypic assessment

To evaluate the phenotype of D12 cells within bare rings and across the stiffness range of 3D bioprinted constructs, I quantified the relative mRNA abundance for several phenotypic marker genes. All three of our candidate housekeeping genes (GAPDH, YWHAZ, UBC) were mathematically stable, however, UBC was chosen for data normalization based on a higher Bestkeeper Pearson correlation coefficient and a stronger Normfinder stability value (Table 4.01).

	GAPDH	**YWHAZ**	**UBC**
Cq Arithmetic Mean (± SD)	17.25 ± 0.65	20.15 ± 0.42	24.77 ± 1.05
Bestkeeper Pearson correlation coefficient	0.967	0.904	0.978
Bestkeeper p-value	0.001	0.001	0.001
NormFinder stability value	0.369	0.466	0.180

Table 4.01. Selection of housekeeping genes in D12 sandwiches. Candidate housekeeping control genes exhibited consistent mRNA levels across the various conditions tested. Pooled data analyzed using Bestkeeper and Normfinder ranked UBC as the most stably expressed candidate, thus it was selected as the reference gene for data analysis.

I observed significant differences in MHC mRNA levels between ASM tissues constructed with 0.75% acellular and bare rings (2.21 times higher, one way-ANOVA $p = 0.0231$), however, no significant differences were found between 1% and 1.25% tissues versus the bare rings (all $p > 0.05$). Acellular matrix stiffness had no statistically significant impact on mRNA levels of SM22α, but it was found to be significantly higher in ASM tissues fabricated with 1.25% compared with bare rings (2.5 times higher, one-way ANOVA $p = 0.0165$). Although COL-1 and A-ACT mRNA levels trended higher in bare rings, there were no statistically significant differences (One-way ANOVA $p = 0.1153$ and $p= 0.7127$) across the conditions tested. Finally, relative mRNA abundance of fibronectin was not significantly different in 0.75%, 1% and 1.25% ASM tissues (One-way ANOVA $p = 0.8073$). Bare rings were excluded in the qPCR reactions for fibronectin because they did not generate the required amount of RNA samples. These combined data indicate a mild phenotypic modulation of ASM by the different acellular stiffnesses within 3D bioprinted constructs.

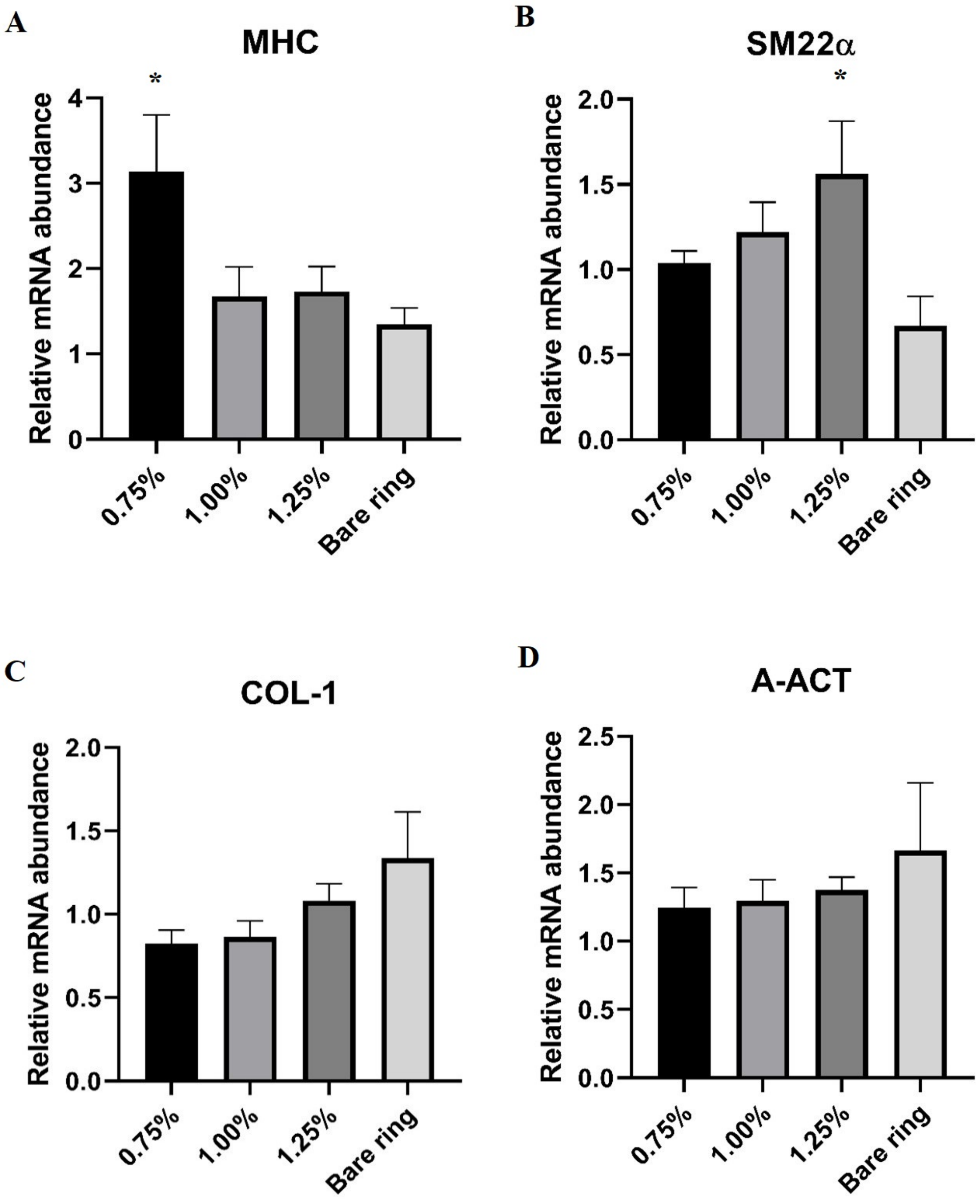
A
MHC
*
Relative mRNA abundance
0
1
2
3
4
0.75%
1.00%
1.25%
Bare ring
B
SM22α
*
Relative mRNA abundance
0.0
0.5
1.0
1.5
2.0
0.75%
1.00%
1.25%
Bare ring
C
COL-1
Relative mRNA abundance
0.0
0.5
1.0
1.5
2.0
0.75%
1.00%
1.25%
Bare ring
D
A-ACT
Relative mRNA abundance
0.0
0.5
1.0
1.5
2.0
2.5
0.75%
1.00%
1.25%
Bare ring

E

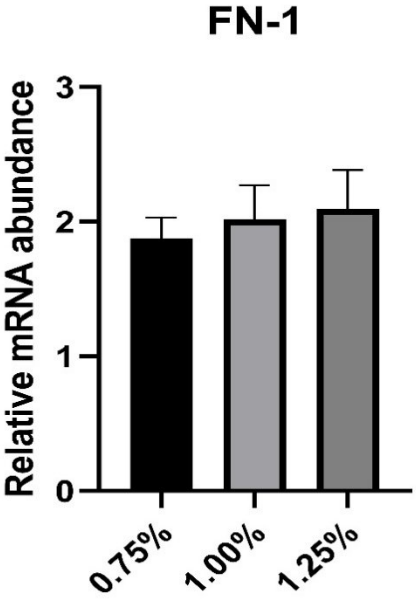

Figure 4.07. Comparison of relative mRNA abundance (n = 8). Data are reported as fold change difference between target genes and the housekeeping gene UBC. Significantly higher levels of (A) MHC and (B) SM22α were detected in the 0.75% and 1.25% ASM tissues compared with bare rings. However, no significant differences were found across the 3D stiffness range trialed. (C) Collagen-1, (D) Alpha Actin and (E) Fibronectin-1 mRNA abundance was not significantly different in all conditions tested (all $p > 0.05$).

Chapter five: Discussion, conclusion, and relevance

5.1 Discussion

Development of 3D bioprinted model

A major pathological feature of asthma is airway wall remodelling, which may contribute to excessive contraction of airway smooth muscle through altered extracellular matrix signalling and mechano-transduction events. However, as ASM physiology has traditionally been studied in flat and rigid 2D plastic models that inadequately recreate *in vivo* micro-environments, the precise effects of mechanical factors are still poorly understood. Even though *ex vivo* ASM tissues and decellularized lung matrices provide biologically relevant 3D structures, difficulties with sourcing these tissues and fine tuning them to recreate the chronic effects of airway remodeling invariably hampers their routine use in research.

The development of various tissue engineering techniques has enabled the creation of experimental models to study cellular function in a more physiologically relevant mechanical environment. Specifically, 3D bioprinting technology with precision extrusion systems can precisely control the physical architecture of fabricated constructs to mimic the structural complexity of *in vivo* tissues more closely. This enables high-throughput production of organotypic models that can be easily and rapidly customized. In this thesis, I utilized 3D bioprinting to develop a novel, stiffness-modifiable, cell culture model of ASM and characterized its suitability for studying the effects of airway biomechanics on ASM phenotype and function.

Optimization of a 3D bioprinted tissue design and bio-ink formulation is essential to drive tissue maturation and support maximal cellular function (183). It was also essential to design our model to allow tissue stiffness to be modified and contractile function to be measured, while creating a construct that could be easily manufactured and handled for routine experimentation. Alginate was chosen as the core component of our custom bio-ink formulation because the RX-1 bioprinter is nominally designed to work with this polysaccharide. Further, since the stiffness of alginates can easily be tuned based on concentration, MW and G:M ratio, it became an ideal choice for our target ASM mechanobiology application. I excluded high MW alginates from print runs because their high viscosities resulted in slow print speeds with inconsistent extrusion quality. Low

G:M alginates were also excluded for their low strength to weight ratio. A low MW, high G:M alginate offered the ideal balance between the two extremes and was ultimately selected for its high printing fidelity at both very high and low concentrations, producing an extremely wide qualitative stiffness range.

The alginate composition of the cellular bio-ink proved to be critical, with alginate concentrations of >0.5% ultimately preventing the formation of cell-cell networks and tissue maturation. This may be expected, as previous studies have reported that increasing alginate concentrations negatively impact cell functionality due to poor diffusivity, low porosity and non-recognizability of standard alginate by cellular receptors (139,167,184). However, I experienced practical limitations when printing with low alginate concentrations of ≤0.75%. Although these fostered cell-cell network formation, tissues rapidly generated baseline tone, which caused ring structures to collapse. Several strategies were unsuccessfully trialed to increase the structural integrity of the ring, including Janus fibres, alternating cellular and acellular rings, and altering the aspect ratio of the construct. Ultimately, only the sandwich physical design, which encapsulates the cellular muscle bundle within a stiff acellular frame, was able to successfully prevent ring collapse. This allowed the alginate concentration of the cellular layers to be set at an intermediate level of 0.375% alginate, while reinforcing this with acellular layers printed at much higher alginate concentrations. Further, the use of collagen-I to make the tissue more realistic and incorporating fibrinogen as an extra layer of biochemical and mechanical support created a model that was highly printable and suitable for ongoing experimentation.

Assessment of vital morphological and functional properties including f-actin expression, cell viability and generation of baseline tone, revealed the sandwich provided an optimal structure that supported ASM survivability. These printed tissues exhibited many features consistent with a well-organized 3D structure, including a homogenous distribution of cell nuclei across a range of z-heights, alignment of f-actin fibres along the axis of tension development and superior mechanical stability for up to 7 days after printing. This tissue-level arrangement is a stark improvement over free-floating rings and bulk hydrogels, which are characterized by poor cellular organization, insufficient structural integrity and a lack of biologically relevant mechanical load opposing muscle contraction (129,154,180,185). When compared with 2D cultures, cells in 3D sandwiches demonstrated a higher abundance of ‘mature’ contractile markers including MHC and

Desmin, confirming the adoption of a physiologically relevant phenotype (Figure 3.16, p. 51). ASM cells were able to remodel their 3D micro-environment and generate substantial baseline tension, evident as an unstimulated reduction in lumen areas beginning just a few hours after printing and continuing over several days. Baseline tension development was matched by an opposing force provided by the acellular layers, effectively limiting excessive compaction and loss of structural integrity. The sandwich design also allowed us to easily control the composition and physical properties of the micro-environment surrounding the cells, establishing the 3D sandwich model as a suitable platform to simulate the effects of chronic airway remodeling on ASM contractility. In addition to mimicking the elastic attachments of parenchymal tethers and compressive luminal elements of native airways, the improved mechanical loads are also a plausible mechanism for the improved cell differentiation and fibre alignment observed in our sandwich model, as bare ASM rings generated f-actin fibres with no signs of uniformity. This finding is in line with previous studies that have identified the crucial roles mechanical cues play in regulating focal adhesion, adherens junction formation, cell alignment and maturation of both smooth (130) and cardiac muscle tissues (186).

An alternative approach that may enable usage of bare cellular rings without an acellular structural component would be the use of very low MW alginates in which the co-polymer chain is further shortened by treatment with alginate lyases (187). In discussions with other Aspect Biosystems RX-1 users, these extremely low MW alginates can be used at concentrations as high as 5% and may facilitate both mechanical stability and cell spreading. The idea that alginate chain length may specifically regulate cell spreading is consistent with previous studies (188) and unpublished observations from our laboratory, where low and high MW alginate, even at very low concentrations (0.1%) in the cellular layers, can completely inhibit spreading of smooth, cardiac and skeletal muscle cells. The use of extremely low molecular weight alginates in bare rings was not pursued in this thesis, due to the capability of the sandwich to completely uncouple the cellular and acellular components, which provides a greater freedom for tissue optimization.

Evaluations of cell viability did reveal some evidence of cell stress (LDH release) and cell death (propidium iodide staining) in the sandwich model. This may indicate a lower degree of cell survival compared with very high cell viabilities of up to 95% that have previously been reported using 3D bioprinting technology (189). However, these constructs are usually fabricated with more complex components including decellularized matrices (190), addition of stem cells (191) and a cocktail of several ECM proteins (152) that are exceptionally expensive, potentially limiting their use in routine research. Further, as these extra components are known to modulate the cellular phenotype (100), including them as a core component of our methodology would inevitably introduce confounding variables. While this might not be an issue when integrated responses are being evaluated, it would make characterizing ASM response(s) to a specific disease-relevant ECM component problematic. Conversely, the reported cell viability in this study is significantly higher than those reported by Berg *et al* (192) and Mestre *et al* (193) using simple bio-inks formulated with 50% Matrigel.

It is also worth noting that cell mortality in our constructs was likely over-estimated using Hoechst/Propidium Iodide staining. Our creation of dense tissues with a significant structural component means that dead cells are retained within the matrix for a significant but indeterminate time. The fluorophores used have been shown to induce phototoxicity in cells and these could also be entrapped in the alginate matrix and cause background fluorescence that interferes with the evaluation of fluorescent signals (194). The laboratory is presently working on establishing protocols to confirm absolute cell viability in our constructs, including dissociating the structure to a single cell suspension that would allow analysis with flow cytometry. Ultimately, when producing a mature contractile tissue, the best metric for success is contractile function rather than the absolute value of cell viability.

Contractile phenotype and function

The overarching goal of this thesis was to produce a contractile ASM tissue and use this to determine if changes in tissue stiffness associated with airway wall remodelling enhances the contractile phenotype and function of ASM. This would allow me to address the hypothesis that increased tissue stiffness is a mechanism for developing airway hyper-responsiveness in asthma. I found that ASM tissues fabricated across a range of acellular stiffnesses displayed significantly different levels of baseline shortening and differentially responded to biologically relevant contractile/relaxant mediators. Although there were statistically significant differences in the physiologic responses across stiffness groups, post-tests were unable to determine which group comparisons showed the most disparity.

Inferences about the effects of increasing tissue stiffness on ASM contractility were complex due to our inability to precisely estimate the Young's moduli (a measure of the tensile and compressive stiffness properties of a material in response to uniaxial forces) of the different acellular mechanical loads. To quantify cellular and acellular stiffness, constructing quasi-static length-tension curves using a wire myograph was considered. However, the size of our bioprinted structures far exceeded the dimensions of what the myograph was capable of measuring and there were practical difficulties with handling and mounting tissues. Attempts to reduce the size of constructs were confounded by bioprinter capabilities and physical handling characteristics. Presently, rheometry is being investigated as a method to quantify alginate stiffness, which would enable measurement of the compressive and shear properties of the sandwich constructs without size, mounting or handling concerns. If the mechanical properties of the alginate can be accurately quantified, this will allow for muscle shortening to become a direct measure of active force generation by the muscle cells, enabling a more direct comparison of physiological responses with other models of ASM, including *ex vivo* tissues and microtissues. Until these experiments are completed, the magnitude of the stiffness differences, the biological relevance of the acellular loads, and how they translate to asthmatic airways, remains an open question. Nevertheless, numerous studies have correlated the Young's moduli of alginate hydrogels to increasing alginate concentrations (195,196), and the variance in contractile responses observed provides strong evidence for the regulation of cellular function by the mechanical micro-environment.

It was expected that any enhancement of contractile function would be modulated through an altered contractile phenotype. Although varying degrees of mRNA abundance were observed in some target genes, there were no statistically significant differences between the sandwich stiffness groups tested. However, there were significantly higher mRNA levels of contractile proteins MHC and SM22α in ASM tissues fabricated with 0.75% and 1.25% acellular alginate compared with bare ASM rings. Since these genes are known to be upregulated specifically in adult smooth muscle, this further lends credence to the idea that appropriate mechanical loads opposing contraction are essential for tissue maturation.

Caution should be exercised when interpreting these results, as statistical significance does not necessarily translate to biological significance, and there may still be stiffness regulation occurring that remains undetectable at this time. A post-hoc statistical power calculation performed using the ‘pwr’ package for R studio, revealed my experiments had an 80% power in detecting significant differences only if the effect sizes were greater than 55% with the sample size used (see Appendix A p. 98). This would mean the probability of detecting medium or small statistically significant changes in mRNA abundance between groups was low. Similarly, mRNA abundance may not be an accurate representation of the cell phenotype as many studies have demonstrated the functional properties of ASM are regulated at levels beyond gene expression, namely protein expression and phosphorylation (197). Even more so, the time point at which RNA samples were isolated could be a confounding factor in correlating mRNA abundance to contractility. Contractile function was assessed at day 6, because at this time the cells had fully compacted and remodelled the matrix into a mature functional tissue. In contrast, RNA was collected 48 hours after printing because RNA yields were highest at this time point, and it was assumed that this stage would be most representative of the molecular processes underpinning tissue maturation and phenotype. However, it is unlikely that mRNA abundance measurements taken at a single timepoint can completely capture processes related to chronic phenotypic regulation, warranting further inquiry.

5.2 Limitations and Mitigations

In this thesis, I have used a physical design that ‘uncouples’ the muscle bundle from acellular structural components and I have relied exclusively on stiffness modification by tuning the mechanical properties of these acellular layers. In asthma however, airway remodeling events result in mechanical changes in each of the ASM bundles, lung parenchymal elements and the bulk of the airway wall. Although keeping the stiffness of the muscle bundle constant was an inherent methodological limitation in creating a functional tissue, it precludes us from replicating structural remodeling events occurring within the muscle layers, and as a result, the disease implications of our approach remain unclear. Despite this, the acellular stiffness does create a mechanical load that simulates increased density of the airway wall from parenchymal tethers, or increased bulk within the luminal layers. There are several additional strategies that could augment the disease relevance of our constructs. For example, ASM tissues can be crosslinked post-printing by glycation with non-reducing sugars like ᴅ-ribose and ultraviolet light exposure (198,199). Another strategy would be to partly or completely substitute the collagen and fibrinogen components of our bio-inks with pathological matrix proteins or decellularized matrices. It would also be possible to treat these tissues with TGF-β to stimulate ECM secretion by the ASM cells. In these contexts, this model would be a valuable tool in comparing and contrasting the specific effects of different ECM and fibrotic mediators in regulating ASM function.

Another important consideration with the sandwich design is that the mechanical load constituted by the acellular alginate layers holds the muscle bundle in such a way that it behaves like an imperfect spring. Even though this load is enough to limit excessive compaction and can hold a significant amount of tension (evidenced by the citrate/EDTA results), a true elastic structure would allow the muscle layers to 'spring back' to baseline levels after the tension ablation experiments with cytochalasin D, as observed in ASM microtissues. Our laboratory is currently working on an evolution of the sandwich design that increases the elastic properties of constructs. From personal communications with Dr. West, it does appear that a more elastic design is able to revert lumen areas back to baseline levels after cytochalasin D treatment. An additional concern with the sandwich design is that the physical size and free-floating nature of the constructs limited my ability to perform live cell microscopy during all contraction experiments. This introduces the possibility of artefactual observations from evaluating cellular responses outside a non-physiological environment. The most likely effect of measuring contraction at room temperature versus 37°C would be a slower and less complete contraction, which might also be a plausible explanation for the tension ablation results (cytochalasin D was the last drug administered after the cells had been at room temperature for about 20 minutes). As part of the sandwich evolution process, tissues can be held firmly in place, allowing for rapid montage imaging of the whole structure at physiological conditions in the Cytation 5.

Finally, in this thesis I have first focused on re-creating tissue mechanics, mainly due to the limitations of other experimental models, and because it is the disease-relevant component most needed to be solved by a 3D model. Moving forward, the ease with which the model can be made multicellular will be exploited to fabricate a more physiologically relevant construct. Such a multicellular 3D bioprinted tissue would be a significant improvement over common techniques including Transwell co-culture systems, conditioned media, and microfluidic organ-on-chip models, as it allows physical interaction between cells that may be especially important to cellular function. Since the 3D micro-environment naturally supresses proliferation to the more realistic *in vivo* condition (200), 3D models dramatically reduce the risk of one fast-growing cell type 'taking over' the culture in the timespan of a normal experiment. Our laboratory has already proven fibroblasts can survive when co-cultured with printed smooth, cardiac and skeletal muscle tissues (unpublished data). However, unlike the microtissue model, fibroblasts are not a necessary requirement for bioprinted tissue formation. Separate bioprinting projects have also proven the feasibility of epithelial cell bioprinting, with A549 and Calu-3 cells both working at optimal capacities. Next, an emphasis will be placed on evaluating the fundamental mechanisms of tissue remodeling by incorporating immune cells and immune modulators in our constructs with a goal to highlight the synergistic relationship between these inflammatory mediators and mechanical factors driving asthma pathogenesis.

5.3 Conclusions and Significance

I have used novel 3D bioprinting technology to create a flagship research model of ASM that has been optimized and validated for mechano-transduction and contraction research. My model exhibited the essential features of a physiologically relevant mature ASM tissue. These include cells compacting and remodeling the matrix, cells arranging into a well-patterned and highly organized 3D tissue construct, and cells expressing higher levels of contractile genes compared with those in standard 2D cultures. Critically, the tissues generated substantial baseline tension during maturation, and responded appropriately to contractile and relaxant stimuli. This represents a high-throughput and convenient alternative to current 3D models with improved physiological relevance versus standard 2D cell cultures.

Further, stiffness modulation of ASM tissues using the sandwich design resulted in a differential display of functional responses to contractile and relaxant agents. This supports the idea that mechanical cues may have profound effects on cellular function, although direct disease relevance to asthma has not yet been established. Thus, I have created an important tool that will help unmask factors driving disease pathogenesis, which will be essential for the ongoing development and pre-clinical screening of next generation therapeutic strategies targeting the structural defects found in asthma.

REFERENCES

1. Connors C, Millar WJ. Changes in children's hospital use. Health Rep [Internet]. 1999;11(2):9-19(Eng); 9-21(Fre). Available from: https://www.ncbi.nlm.nih.gov/pubmed/10618739

2. Masoli M, Fabian D, Holt S, Beasley R. The global burden of asthma: executive summary of the GINA Dissemination Committee report. Allergy. 2004 May;59(5):469–78.

3. Dharmage SC, Perret JL, Custovic A. Epidemiology of Asthma in Children and Adults. Frontiers in pediatrics [Internet]. 2019 Jun 18;7:246. Available from: https://pubmed.ncbi.nlm.nih.gov/31275909

4. Nunes C, Pereira AM, Morais-Almeida M. Asthma costs and social impact. Asthma research and practice [Internet]. 2017 Jan 6;3:1. Available from: https://pubmed.ncbi.nlm.nih.gov/28078100

5. Zervas E, Samitas K, Papaioannou AI, Bakakos P, Loukides S, Gaga M. An algorithmic approach for the treatment of severe uncontrolled asthma. ERJ Open Research [Internet]. 2018 Jan 6;4(1):125–2017. Available from: http://www.ncbi.nlm.nih.gov/pmc/articles/PMC5838355/

6. Edwards MR, Saglani S, Schwarze J, Skevaki C, Smith JA, Ainsworth B, et al. Addressing unmet needs in understanding asthma mechanisms: From the European Asthma Research and Innovation Partnership (EARIP) Work Package (WP)2 collaborators. The European respiratory journal. 2017 May;49(5).

7. Pembrey L, Barreto ML, Douwes J, Cooper P, Henderson J, Mpairwe H, et al. Understanding asthma phenotypes: the World Asthma Phenotypes (WASP) international collaboration. ERJ open research [Internet]. 2018 Aug 22;4(3):13–2018. Available from: https://pubmed.ncbi.nlm.nih.gov/30151371

8. Kuruvilla ME, Lee FE-H, Lee GB. Understanding Asthma Phenotypes, Endotypes, and Mechanisms of Disease. Clinical reviews in allergy & immunology [Internet]. 2019 Apr;56(2):219–33. Available from: https://pubmed.ncbi.nlm.nih.gov/30206782

9. Braman SS. The global burden of asthma. Chest. 2006 Jul;130(1 Suppl):4S-12S.

10. Woolcock AJ. What is bronchial hyperresponsiveness from the clinical standpoint. Airway hyperresponsiveness: is it really important for asthma. 1993;1–9.

11. Xu X, Rijcken B, Schouten JP, Weiss ST. Airways responsiveness and development and remission of chronic respiratory symptoms in adults. The Lancet [Internet]. 1997 Nov 15;350(9089):1431–4. Available from: https://doi.org/10.1016/S0140-6736(97)10041-1

12. Fardon TC, Currie G, Lee DKC, Lipworth BJ. Lower thresholds for bronchial challenge testing. Vol. 59, Allergy. Denmark; 2004. p. 1125–6.

13. Ramsdell JW, Nachtwey FJ, Moser KM. Bronchial hyperreactivity in chronic obstructive bronchitis. The American review of respiratory disease. 1982 Nov;126(5):829–32.

14. Eggleston PA, Rosenstein BJ, Stackhouse CM, Alexander MF. Airway Hyperreactivity in Cystic Fibrosis: Clinical Correlates and Possible Effects on the Course of the Disease. CHEST [Internet]. 1988 Aug 1;94(2):360–5. Available from: https://doi.org/10.1378/chest.94.2.360

15. WEISS ST, VAN NATTA ML, ZEIGER RS. Relationship between Increased Airway Responsiveness and Asthma Severity in the Childhood Asthma Management Program. American Journal of Respiratory and Critical Care Medicine [Internet]. 2000 Jul 1;162(1):50–6. Available from: https://doi.org/10.1164/ajrccm.162.1.9811005

16. Cockcroft DW. Methacholine Challenge. PD20 versus PC20. Annals of the American Thoracic Society [Internet]. 2015 Mar 1;12(3):291–2. Available from: https://doi.org/10.1513/AnnalsATS.201501-049ED

17. de Jongste JC, Kerrebijn KF. Is bronchial hyperresponsiveness in humans a smooth muscle abnormality? Progress in clinical and biological research [Internet]. 1988;263:255–65. Available from: http://europepmc.org/abstract/MED/3289012

18. Ijpma G, Matusovsky O, Lauzon A-M. Accumulating Evidence for Increased Velocity of Airway Smooth Muscle Shortening in Asthmatic Airway Hyperresponsiveness. Bossé Y, editor. Journal of Allergy [Internet]. 2012;2012:156909. Available from: https://doi.org/10.1155/2012/156909

19. Black JL, Marthan R, Armour CL, Johnson PR. Sensitization alters contractile responses and calcium influx in human airway smooth muscle. The Journal of allergy and clinical immunology. 1989 Oct;84(4 Pt 1):440–7.

20. Barnes PJ. Immunology of asthma and chronic obstructive pulmonary disease. Nature Reviews Immunology [Internet]. 2008 Feb 15;8:183. Available from: http://dx.doi.org/10.1038/nri2254

21. Borish L. The immunology of asthma: Asthma phenotypes and their implications for personalized treatment. Annals of allergy, asthma & immunology : official publication of the American College of Allergy, Asthma, & Immunology [Internet]. 2016 Aug;117(2):108–14. Available from: https://pubmed.ncbi.nlm.nih.gov/27499537

22. CRIMI E, SPANEVELLO A, NERI M, IND PW, ROSSI GA, BRUSASCO V. Dissociation between Airway Inflammation and Airway Hyperresponsiveness in Allergic Asthma. American Journal of Respiratory and Critical Care Medicine [Internet]. 1998 Jan 1;157(1):4–9. Available from: https://doi.org/10.1164/ajrccm.157.1.9703002

23. Djukanović R, Wilson SJ, Kraft M, Jarjour NN, Steel M, Chung KF, et al. Effects of treatment with anti-immunoglobulin E antibody omalizumab on airway inflammation in allergic asthma. American journal of respiratory and critical care medicine. 2004 Sep;170(6):583–93.

24. McGrath KW, Icitovic N, Boushey HA, Lazarus SC, Sutherland ER, Chinchilli VM, et al. A large subgroup of mild-to-moderate asthma is persistently noneosinophilic. American journal of respiratory and critical care medicine [Internet]. 2012/01/20. 2012 Mar 15;185(6):612–9. Available from: https://pubmed.ncbi.nlm.nih.gov/22268133

25. Leckie MJ, ten Brinke A, Khan J, Diamant Z, O'Connor BJ, Walls CM, et al. Effects of an interleukin-5 blocking monoclonal antibody on eosinophils, airway hyper-responsiveness, and the late asthmatic response. Lancet (London, England). 2000 Dec;356(9248):2144–8.

26. Gabehart KE, Royce SG, Maselli DJ, Miyasato SK, Davis EC, Tang MLK, et al. Airway hyperresponsiveness is associated with airway remodeling but not inflammation in aging Cav1-/- mice. Respiratory research. 2013 Oct;14(1):110.

27. Poynter ME, Irvin CG. Interleukin-6 as a biomarker for asthma: hype or is there something else? European Respiratory Journal [Internet]. 2016 Oct 1;48(4):979 LP – 981. Available from: http://erj.ersjournals.com/content/48/4/979.abstract

28. Chung KF. Targeting the interleukin pathway in the treatment of asthma. Lancet (London, England). 2015 Sep;386(9998):1086–96.

29. Piyadasa H, Altieri A, Basu S, Schwartz J, Halayko AJ, Mookherjee N. Biosignature for airway inflammation in a house dust mite-challenged murine model of allergic asthma. Biology open. 2016 Jan;5(2):112–21.

30. Grainge CL, Lau LCK, Ward JA, Dulay V, Lahiff G, Wilson S, et al. Effect of Bronchoconstriction on Airway Remodeling in Asthma. New England Journal of Medicine [Internet]. 2011 May 25;364(21):2006–15. Available from: https://doi.org/10.1056/NEJMoa1014350

31. Pascoe CD, Green FHY, Elliot JG, James AL, Noble PB, Donovan GM. Airway remodelling with spatial correlations: Implications for asthma pathogenesis. Respiratory Physiology & Neurobiology [Internet]. 2020;279:103469. Available from: http://www.sciencedirect.com/science/article/pii/S1569904820301270

32. Nayak AP, Deshpande DA, Penn RB. New targets for resolution of airway remodeling in obstructive lung diseases. F1000Research [Internet]. 2018 May 30;7:F1000 Faculty Rev-680. Available from: https://pubmed.ncbi.nlm.nih.gov/29904584

33. Pepe C, Foley S, Shannon J, Lemiere C, Olivenstein R, Ernst P, et al. Differences in airway remodeling between subjects with severe and moderate asthma. Journal of Allergy and Clinical Immunology [Internet]. 2018 Jan 12;116(3):544–9. Available from: http://dx.doi.org/10.1016/j.jaci.2005.06.011

34. Locke NR, Royce SG, Wainewright JS, Samuel CS, Tang ML. Comparison of airway remodeling in acute, subacute, and chronic models of allergic airways disease. American journal of respiratory cell and molecular biology. 2007 May;36(5):625–32.

35. Hellings PW, Steelant B. Epithelial barriers in allergy and asthma. The Journal of allergy and clinical immunology [Internet]. 2020 Jun;145(6):1499–509. Available from: https://pubmed.ncbi.nlm.nih.gov/32507228

36. Tilley AE, Walters MS, Shaykhiev R, Crystal RG. Cilia dysfunction in lung disease. Annual review of physiology [Internet]. 2014/10/29. 2015;77:379–406. Available from: https://pubmed.ncbi.nlm.nih.gov/25386990

37. Li X, Wilson JW. Increased vascularity of the bronchial mucosa in mild asthma. Am J Respir Crit Care Med [Internet]. 1997;156(1):229–33. Available from: http://dx.doi.org/10.1164/ajrccm.156.1.9607066

38. Benayoun L, Druilhe A, Dombret M-C, Aubier M, Pretolani M. Airway structural alterations selectively associated with severe asthma. American journal of respiratory and critical care medicine. 2003 May;167(10):1360–8.

39. Bossé Y, Paré PD, Seow CY. Airway wall remodeling in asthma: from the epithelial layer to the adventitia. Current allergy and asthma reports. 2008 Jul;8(4):357–66.

40. Parameswaran K, Willems-Widyastuti A, Alagappan VKT, Radford K, Kranenburg AR, Sharma HS. Role of extracellular matrix and its regulators in human airway smooth muscle biology. Cell Biochemistry and Biophysics. 2006;44(1):139–46.

41. Araujo BB, Dolhnikoff M, Silva LFF, Elliot J, Lindeman JHN, Ferreira DS, et al. Extracellular matrix components and regulators in the airway smooth muscle in asthma. European Respiratory Journal [Internet]. 2008 Jul 1;32(1):61 LP – 69. Available from: http://erj.ersjournals.com/content/32/1/61.abstract

42. Fehrenbach H, Wagner C, Wegmann M. Airway remodeling in asthma: what really matters. Cell and tissue research [Internet]. 2017/02/11. 2017 Mar;367(3):551–69. Available from: https://pubmed.ncbi.nlm.nih.gov/28190087

43. Baldwin L, Roche WR. Does remodelling of the airway wall precede asthma? Paediatric Respiratory Reviews [Internet]. 2018 Jan 12;3(4):315–20. Available from: http://dx.doi.org/10.1016/S1526054202002610

44. Shiba K, Kasahara K, Nakajima H, Adachi M. Structural Changes of the Airway Wall Impair Respiratory Function, Even in Mild Asthma. Chest [Internet]. 2002;122(5):1622–6. Available from: http://www.sciencedirect.com/science/article/pii/S0012369215499490

45. WARD C, JOHNS DP, BISH ROS, PAIS M, REID DW, INGRAM C, et al. Reduced Airway Distensibility, Fixed Airflow Limitation, and Airway Wall Remodeling in Asthma. American Journal of Respiratory and Critical Care Medicine [Internet]. 2001 Nov 1;164(9):1718–21. Available from: https://doi.org/10.1164/ajrccm.164.9.2102039

46. An SS, Bai TR, Bates JHT, Black JL, Brown RH, Brusasco V, et al. Airway smooth muscle dynamics: a common pathway of airway obstruction in asthma. European Respiratory Journal [Internet]. 2007 May 1;29(5):834 LP – 860. Available from: http://erj.ersjournals.com/content/29/5/834.abstract

47. STEPHENS NL, LI W, WANG Y, MA X. The Contractile Apparatus of Airway Smooth Muscle. American Journal of Respiratory and Critical Care Medicine [Internet]. 1998 Nov 1;158(supplement_2):S80–94. Available from: https://doi.org/10.1164/ajrccm.158.supplement_2.13tac300

48. Stephens NL, van Niekerk W. Isometric and isotonic contractions in airway smooth muscle. Canadian journal of physiology and pharmacology. 1977 Aug;55(4):833–8.

49. Bossé Y, Riesenfeld EP, Paré PD, Irvin CG. It's not all smooth muscle: non-smooth-muscle elements in control of resistance to airflow. Annual review of physiology. 2010;72:437–62.

50. Paré PD, Mitzner W. Airway-parenchymal interdependence. Comprehensive Physiology [Internet]. 2012 Jul;2(3):1921–35. Available from: https://pubmed.ncbi.nlm.nih.gov/23723029

51. BRACKEL HJL, PEDERSEN OF, MULDER PGH, OVERBEEK SE, KERREBIJN KF, BOGAARD JM. Central Airways Behave More Stiffly during Forced Expiration in Patients with Asthma. American Journal of Respiratory and Critical Care Medicine [Internet]. 2000 Sep 1;162(3):896–904. Available from: https://doi.org/10.1164/ajrccm.162.3.9905034

52. Oliver MN, Fabry B, Marinkovic A, Mijailovich SM, Butler JP, Fredberg JJ. Airway hyperresponsiveness, remodeling, and smooth muscle mass: right answer, wrong reason? American journal of respiratory cell and molecular biology. 2007 Sep;37(3):264–72.

53. Lambert RK, Wiggs BR, Kuwano K, Hogg JC, Paré PD. Functional significance of increased airway smooth muscle in asthma and COPD. Journal of applied physiology (Bethesda, Md : 1985). 1993 Jun;74(6):2771–81.

54. Niimi A, Matsumoto H, Takemura M, Ueda T, Chin K, Mishima M. Relationship of Airway Wall Thickness to Airway Sensitivity and Airway Reactivity in Asthma. American Journal of Respiratory and Critical Care Medicine [Internet]. 2003 Oct 15;168(8):983–8. Available from: https://doi.org/10.1164/rccm.200211-1268OC

55. McParland BE, Macklem PT, Paré PD. Airway wall remodeling: friend or foe? Journal of Applied Physiology [Internet]. 2003 Jul 1;95(1):426–34. Available from: https://doi.org/10.1152/japplphysiol.00159.2003

56. Paré PD. Airway Hyperresponsiveness in Asthma. American Journal of Respiratory and Critical Care Medicine [Internet]. 2003 Oct 15;168(8):913–4. Available from: https://doi.org/10.1164/rccm.2307005

57. Noble PB, Pascoe CD, Lan B, Ito S, Kistemaker LEM, Tatler AL, et al. Airway smooth muscle in asthma: Linking contraction and mechanotransduction to disease pathogenesis and remodelling. Pulmonary Pharmacology & Therapeutics [Internet]. 2014;29(2):96–107. Available from: http://www.sciencedirect.com/science/article/pii/S1094553914000868

58. Noble PB, Turner DJ, Mitchell HW. Relationship of airway narrowing, compliance, and cartilage in isolated bronchial segments. Journal of applied physiology (Bethesda, Md : 1985). 2002 Mar;92(3):1119–24.

59. Noble PB, McFawn PK, Mitchell HW. Responsiveness of the isolated airway during simulated deep inspirations: effect of airway smooth muscle stiffness and strain. Journal of applied physiology (Bethesda, Md : 1985). 2007 Sep;103(3):787–95.

60. Fabry B, Fredberg JJ. Mechanotransduction, asthma, and airway smooth muscle. Drug discovery today Disease models [Internet]. 2007;4(3):131–7. Available from: https://pubmed.ncbi.nlm.nih.gov/18836522

61. Chen KD, Li YS, Kim M, Li S, Yuan S, Chien S, et al. Mechanotransduction in response to shear stress. Roles of receptor tyrosine kinases, integrins, and Shc. The Journal of biological chemistry. 1999 Jun;274(26):18393–400.

62. Szafranski JD, Grodzinsky AJ, Burger E, Gaschen V, Hung H-H, Hunziker EB. Chondrocyte mechanotransduction: effects of compression on deformation of intracellular organelles and relevance to cellular biosynthesis. Osteoarthritis and cartilage. 2004 Dec;12(12):937–46.

63. Dunn GA, Brown AF. Alignment of fibroblasts on grooved surfaces described by a simple geometric transformation. Journal of cell science. 1986 Jul;83:313–40.

64. Xiao Y, Truskey GA. Effect of receptor-ligand affinity on the strength of endothelial cell adhesion. Biophysical journal. 1996 Nov;71(5):2869–84.

65. Hartman CD, Isenberg BC, Chua SG, Wong JY. Vascular smooth muscle cell durotaxis depends on extracellular matrix composition. Proceedings of the National Academy of Sciences of the United States of America [Internet]. 2016 Oct 4;113(40):11190–5. Available from: http://www.ncbi.nlm.nih.gov/pmc/articles/PMC5056055/

66. Eyckmans J, Boudou T, Yu X, Chen CS. A Hitchhiker's Guide to Mechanobiology. Developmental cell [Internet]. 2011 Jul 19;21(1):35–47. Available from: http://www.ncbi.nlm.nih.gov/pmc/articles/PMC3155761/

67. Ingber DE. Cellular Basis of Mechanotransduction. The Biological Bulletin [Internet]. 1998 Jun 1;194(3):323–7. Available from: https://doi.org/10.2307/1543102

68. Holle AW, Engler AJ. More than a feeling: discovering, understanding, and influencing mechanosensing pathways. Current opinion in biotechnology. 2011 Oct;22(5):648–54.

69. Trepat X, Deng L, An SS, Navajas D, Tschumperlin DJ, Gerthoffer WT, et al. Universal physical responses to stretch in the living cell. Nature [Internet]. 2007 May 31;447(7144):592–5. Available from: https://pubmed.ncbi.nlm.nih.gov/17538621

70. Pelham RJ, Wang Y. Cell locomotion and focal adhesions are regulated by substrate flexibility. Proceedings of the National Academy of Sciences [Internet]. 1997 Dec 9;94(25):13661. Available from: http://www.pnas.org/content/94/25/13661.abstract

71. Vogel V, Sheetz M. Local force and geometry sensing regulate cell functions. Nature Reviews Molecular Cell Biology [Internet]. 2006;7(4):265–75. Available from: https://doi.org/10.1038/nrm1890

72. Johnson CP, Tang H-Y, Carag C, Speicher DW, Discher DE. Forced Unfolding of Proteins Within Cells. Science [Internet]. 2007 Aug 3;317(5838):663 LP – 666. Available from: http://science.sciencemag.org/content/317/5838/663.abstract

73. Shivashankar G v. Mechanosignaling to the cell nucleus and gene regulation. Annual review of biophysics. 2011;40:361–78.

74. Trappmann B, Gautrot JE, Connelly JT, Strange DGT, Li Y, Oyen ML, et al. Extracellular-matrix tethering regulates stem-cell fate. Nature Materials [Internet]. 2012;11(7):642–9. Available from: https://doi.org/10.1038/nmat3339

75. Engler AJ, Sen S, Sweeney HL, Discher DE. Matrix Elasticity Directs Stem Cell Lineage Specification. Cell [Internet]. 2018 Jan 12;126(4):677–89. Available from: http://dx.doi.org/10.1016/j.cell.2006.06.044

76. Maksym GN, Deng L, Fairbank NJ, Lall CA, Connolly SC. Beneficial and harmful effects of oscillatory mechanical strain on airway smooth muscle. Canadian journal of physiology and pharmacology. 2005 Oct;83(10):913–22.

77. Ito S, Kume H, Naruse K, Kondo M, Takeda N, Iwata S, et al. A Novel Ca2+ Influx Pathway Activated by Mechanical Stretch in Human Airway Smooth Muscle Cells. American Journal of Respiratory Cell and Molecular Biology [Internet]. 2008 Apr 1;38(4):407–13. Available from: https://doi.org/10.1165/rcmb.2007-0259OC

78. West AR, Connolly S, Mih JD, Billiar KL, Tschumperlin D, Maksym GN. Increased Extracellular Matrix Stiffness Enhances Airway Smooth Muscle Contractile Phenotype And Contractile Function. In: C18 NOVEL MECHANISMS DRIVING AIRWAY REMODELING IN ASTHMA [Internet]. American Thoracic Society; 2011. p. A4052–

A4052. (American Thoracic Society International Conference Abstracts). Available from: https://doi.org/10.1164/ajrccm-conference.2011.183.1_MeetingAbstracts.A4052

79. Polio SR, Stasiak SE, Jamieson RR, Balestrini JL, Krishnan R, Parameswaran H. Extracellular matrix stiffness regulates human airway smooth muscle contraction by altering the cell-cell coupling. Scientific Reports [Internet]. 2019;9(1):9564. Available from: https://doi.org/10.1038/s41598-019-45716-9

80. Shkumatov A, Thompson M, Choi KM, Sicard D, Baek K, Kim DH, et al. Matrix stiffness-modulated proliferation and secretory function of the airway smooth muscle cells. American journal of physiology Lung cellular and molecular physiology. 2015 Jun;308(11):L1125-35.

81. Halayko AJ, Solway J. Molecular mechanisms of phenotypic plasticity in smooth muscle cells. Journal of applied physiology (Bethesda, Md : 1985). 2001 Jan;90(1):358–68.

82. Bossé Y, Sobieszek A, Paré PD, Seow CY. Length Adaptation of Airway Smooth Muscle. Proceedings of the American Thoracic Society [Internet]. 2008 Jan 1;5(1):62–7. Available from: https://www.atsjournals.org/doi/abs/10.1513/pats.200705-056VS

83. Hill MR, Philp CJ, Billington CK, Tatler AL, Johnson SR, O'Dea RD, et al. A theoretical model of inflammation- and mechanotransduction-driven asthmatic airway remodelling. Biomechanics and modeling in mechanobiology [Internet]. 2018/07/02. 2018 Oct;17(5):1451–70. Available from: https://pubmed.ncbi.nlm.nih.gov/29968161

84. Ojiaku CA, Yoo EJ, Panettieri RA. Transforming Growth Factor β1 Function in Airway Remodeling and Hyperresponsiveness. The Missing Link? American Journal of Respiratory Cell and Molecular Biology [Internet]. 2016 Nov 17;56(4):432–42. Available from: https://doi.org/10.1165/rcmb.2016-0307TR

85. Chen G, Khalil N. TGF-beta1 increases proliferation of airway smooth muscle cells by phosphorylation of map kinases. Respiratory research [Internet]. 2006 Jan 3;7(1):2. Available from: https://pubmed.ncbi.nlm.nih.gov/16390551

86. Xie S, Sukkar MB, Issa R, Khorasani NM, Chung KF. Mechanisms of induction of airway smooth muscle hyperplasia by transforming growth factor-beta. American journal of

physiology Lung cellular and molecular physiology [Internet]. 2007/04/27. 2007 Jul;293(1):L245–53. Available from: https://pubmed.ncbi.nlm.nih.gov/17468136

87. Ji H, Tang H, Lin H, Mao J, Gao L, Liu J, et al. Rho/Rock cross-talks with transforming growth factor-β/Smad pathway participates in lung fibroblast-myofibroblast differentiation. Biomedical reports [Internet]. 2014/07/31. 2014 Nov;2(6):787–92. Available from: https://pubmed.ncbi.nlm.nih.gov/25279146

88. Wright D, Sharma P, Ryu M-H, Rissé P-A, Ngo M, Maarsingh H, et al. Models to study airway smooth muscle contraction in vivo, ex vivo and in vitro: Implications in understanding asthma. Pulmonary Pharmacology & Therapeutics [Internet]. 2013;26(1):24–36. Available from: http://www.sciencedirect.com/science/article/pii/S109455391200123X

89. Stephens NL. Airway smooth muscle. Lung [Internet]. 2001;179(6):333–73. Available from: http://dx.doi.org/10.1007/s004080000073

90. Tschumperlin DJ, Boudreault F, Liu F. Recent advances and new opportunities in lung mechanobiology. Journal of biomechanics [Internet]. 2009/10/04. 2010 Jan 5;43(1):99–107. Available from: https://pubmed.ncbi.nlm.nih.gov/19804885

91. Chapman DG, Tully JE, Nolin JD, Janssen-Heininger YM, Irvin CG. Animal models of allergic airways disease: where are we and where to next? Journal of cellular biochemistry [Internet]. 2014 Dec;115(12):2055–64. Available from: https://pubmed.ncbi.nlm.nih.gov/25043224

92. Woo LN, Guo WY, Wang X, Young A, Salehi S, Hin A, et al. A 4-Week Model of House Dust Mite (HDM) Induced Allergic Airways Inflammation with Airway Remodeling. Scientific Reports [Internet]. 2018;8(1):6925. Available from: https://doi.org/10.1038/s41598-018-24574-x

93. Rydell-Törmänen K, Johnson JR. The Applicability of Mouse Models to the Study of Human Disease. Methods in molecular biology (Clifton, NJ) [Internet]. 2019;1940:3–22. Available from: https://pubmed.ncbi.nlm.nih.gov/30788814

94. van Hove CL, Maes T, Joos GF, Tournoy KG. Prolonged Inhaled Allergen Exposure Can Induce Persistent Tolerance. American Journal of Respiratory Cell and Molecular Biology [Internet]. 2007 May 1;36(5):573–84. Available from: https://doi.org/10.1165/rcmb.2006-0385OC

95. Johnson JR, Wiley RE, Fattouh R, Swirski FK, Gajewska BU, Coyle AJ, et al. Continuous Exposure to House Dust Mite Elicits Chronic Airway Inflammation and Structural Remodeling. American Journal of Respiratory and Critical Care Medicine [Internet]. 2004 Feb 1;169(3):378–85. Available from: https://doi.org/10.1164/rccm.200308-1094OC

96. Panettieri RA, Murray RK, DePalo LR, Yadvish PA, Kotlikoff MI. A human airway smooth muscle cell line that retains physiological responsiveness. The American journal of physiology. 1989 Feb;256(2 Pt 1):C329-35.

97. Zhou L, Li J, Goldsmith AM, Newcomb DC, Giannola DM, Vosk RG, et al. Human bronchial smooth muscle cell lines show a hypertrophic phenotype typical of severe asthma. American journal of respiratory and critical care medicine. 2004 Mar;169(6):703–11.

98. Tran T, McNeill KD, Gerthoffer WT, Unruh H, Halayko AJ. Endogenous laminin is required for human airway smooth muscle cell maturation. Respiratory research. 2006 Sep;7(1):117.

99. An SS, Kim J, Ahn K, Trepat X, Drake KJ, Kumar S, et al. Cell stiffness, contractile stress and the role of extracellular matrix. Biochemical and biophysical research communications [Internet]. 2009/03/25. 2009 May 15;382(4):697–703. Available from: https://pubmed.ncbi.nlm.nih.gov/19327344

100. Hirst SJ, Twort CH, Lee TH. Differential effects of extracellular matrix proteins on human airway smooth muscle cell proliferation and phenotype. American journal of respiratory cell and molecular biology. 2000 Sep;23(3):335–44.

101. Walker M, Rizzuto P, Godin M, Pelling AE. Structural and mechanical remodeling of the cytoskeleton maintains tensional homeostasis in 3D microtissues under acute dynamic

stretch. Scientific Reports [Internet]. 2020;10(1):7696. Available from: https://doi.org/10.1038/s41598-020-64725-7

102. Carlson AL, Florek CA, Kim JJ, Neubauer T, Moore JC, Cohen RI, et al. Microfibrous substrate geometry as a critical trigger for organization, self-renewal, and differentiation of human embryonic stem cells within synthetic 3-dimensional microenvironments. FASEB journal : official publication of the Federation of American Societies for Experimental Biology [Internet]. 2012/04/27. 2012 Aug;26(8):3240–51. Available from: https://pubmed.ncbi.nlm.nih.gov/22542683

103. West A, Cole D, Cowley E, Maksym G. Substrate stiffness and geometry differentially regulate proliferation in airway smooth muscle cells. European Respiratory Journal [Internet]. 2013 Sep 1;42(Suppl 57):P569. Available from: http://erj.ersjournals.com/content/42/Suppl_57/P569.abstract

104. Chin LYM, Bossé Y, Pascoe C, Hackett TL, Seow CY, Paré PD. Mechanical properties of asthmatic airway smooth muscle. European Respiratory Journal [Internet]. 2012 Jul 1;40(1):45. Available from: http://erj.ersjournals.com/content/40/1/45.abstract

105. Jamieson RR, Stasiak SE, Polio SR, Parameswaran H. Increasing Stiffness of Collagen Fibers Can Lead to Excessive Constriction of Airways. Biophysical Journal [Internet]. 2020 Feb 7;118(3):122a. Available from: https://doi.org/10.1016/j.bpj.2019.11.805

106. Roberts JA, Raeburn D, Rodger IW, Thomson NC. Comparison of in vivo airway responsiveness and in vitro smooth muscle sensitivity to methacholine in man. Thorax [Internet]. 1984 Nov 1;39(11):837. Available from: http://thorax.bmj.com/content/39/11/837.abstract

107. Liu G, Betts C, Cunoosamy DM, Åberg PM, Hornberg JJ, Sivars KB, et al. Use of precision cut lung slices as a translational model for the study of lung biology. Respiratory Research [Internet]. 2019;20(1):162. Available from: https://doi.org/10.1186/s12931-019-1131-x

108. Bryson KJ, Garrido D, Esposito M, McLachlan G, Digard P, Schouler C, et al. Precision cut lung slices: a novel versatile tool to examine host–pathogen interaction in the chicken

lung. Veterinary Research [Internet]. 2020;51(1):2. Available from: https://doi.org/10.1186/s13567-019-0733-0

109. Martin C, Uhlig S, Ullrich V. Videomicroscopy of methacholine-induced contraction of individual airways in precision-cut lung slices. Eur Respir J [Internet]. 1996;9(12):2479–87. Available from: http://dx.doi.org/10.1183/09031936.96.09122479

110. Li G, Cohen JA, Martines C, Ram-Mohan S, Brain JD, Krishnan R, et al. Preserving Airway Smooth Muscle Contraction in Precision-Cut Lung Slices. Scientific Reports [Internet]. 2020;10(1):6480. Available from: https://doi.org/10.1038/s41598-020-63225-y

111. Maarsingh H, Bidan CM, Brook BS, Zuidhof AB, Elzinga CRS, Smit M, et al. Small airway hyperresponsiveness in COPD: relationship between structure and function in lung slices. American Journal of Physiology-Lung Cellular and Molecular Physiology [Internet]. 2019 Jan 10;316(3):L537–46. Available from: https://doi.org/10.1152/ajplung.00325.2018

112. Hiorns JE, Bidan CM, Jensen OE, Gosens R, Kistemaker LEM, Fredberg JJ, et al. Airway and Parenchymal Strains during Bronchoconstriction in the Precision Cut Lung Slice. Frontiers in Physiology [Internet]. 2016;7:309. Available from: https://www.frontiersin.org/article/10.3389/fphys.2016.00309

113. Sanderson MJ. Exploring lung physiology in health and disease with lung slices. Pulmonary pharmacology & therapeutics [Internet]. 2011/05/12. 2011 Oct;24(5):452–65. Available from: https://pubmed.ncbi.nlm.nih.gov/21600999

114. Noble PB, McFawn PK, Mitchell HW. Responsiveness of the isolated airway during simulated deep inspirations: effect of airway smooth muscle stiffness and strain. Journal of Applied Physiology [Internet]. 2007 Sep 1;103(3):787–95. Available from: https://doi.org/10.1152/japplphysiol.00314.2007

115. Olson JL, Atala A, Yoo JJ. Tissue engineering: current strategies and future directions. Chonnam medical journal [Internet]. 2011/04/26. 2011 Apr;47(1):1–13. Available from: https://pubmed.ncbi.nlm.nih.gov/22111050

116. Niklason LE, Gao J, Abbott WM, Hirschi KK, Houser S, Marini R, et al. Functional arteries grown in vitro. Science (New York, NY). 1999 Apr;284(5413):489–93.

117. Gooch KJ, Blunk T, Courter DL, Sieminski AL, Vunjak-Novakovic G, Freed LE. Bone morphogenetic proteins-2, -12, and -13 modulate in vitro development of engineered cartilage. Tissue engineering. 2002 Aug;8(4):591–601.

118. Bryant SJ, Vernerey FJ. Programmable Hydrogels for Cell Encapsulation and Neo-Tissue Growth to Enable Personalized Tissue Engineering. Advanced healthcare materials [Internet]. 2017/10/04. 2018 Jan;7(1):10.1002/adhm.201700605. Available from: https://pubmed.ncbi.nlm.nih.gov/28975716

119. Ozbolat IT. Scaffold-Based or Scaffold-Free Bioprinting: Competing or Complementing Approaches? Journal of Nanotechnology in Engineering and Medicine [Internet]. 2015 Sep 29;6(2). Available from: https://doi.org/10.1115/1.4030414

120. Fonseca AC, Melchels FPW, Ferreira MJS, Moxon SR, Potjewyd G, Dargaville TR, et al. Emulating Human Tissues and Organs: A Bioprinting Perspective Toward Personalized Medicine. Chemical Reviews [Internet]. 2020 Oct 14;120(19):11093–139. Available from: https://doi.org/10.1021/acs.chemrev.0c00342

121. Singh MR, Patel S, Singh D. Chapter 9 - Natural polymer-based hydrogels as scaffolds for tissue engineering. In: Grumezescu AM, editor. Nanobiomaterials in Soft Tissue Engineering [Internet]. William Andrew Publishing; 2016. p. 231–60. Available from: https://www.sciencedirect.com/science/article/pii/B978032342865100009X

122. Booth AJ, Hadley R, Cornett AM, Dreffs AA, Matthes SA, Tsui JL, et al. Acellular normal and fibrotic human lung matrices as a culture system for in vitro investigation. American journal of respiratory and critical care medicine. 2012 Nov;186(9):866–76.

123. Gilbert TW, Sellaro TL, Badylak SF. Decellularization of tissues and organs. Biomaterials. 2006 Jul;27(19):3675–83.

124. Reddy MSB, Ponnamma D, Choudhary R, Sadasivuni KK. A Comparative Review of Natural and Synthetic Biopolymer Composite Scaffolds. Polymers [Internet]. 2021;13(7). Available from: https://www.mdpi.com/2073-4360/13/7/1105

125. Morris GE, Bridge JC, Eltboli OMI, Lewis MP, Knox AJ, Aylott JW, et al. Human airway smooth muscle maintain in situ cell orientation and phenotype when cultured on aligned electrospun scaffolds. American Journal of Physiology-Lung Cellular and Molecular Physiology [Internet]. 2014 May 2;307(1):L38–47. Available from: https://doi.org/10.1152/ajplung.00318.2013

126. Tran TT, Hamid ZA, Cheong KY. A Review of Mechanical Properties of Scaffold in Tissue Engineering: Aloe Vera Composites. Journal of Physics: Conference Series [Internet]. 2018;1082:012080. Available from: http://dx.doi.org/10.1088/1742-6596/1082/1/012080

127. Bueno EM, Laevsky G, Barabino GA. Enhancing cell seeding of scaffolds in tissue engineering through manipulation of hydrodynamic parameters. J Biotechnol [Internet]. 2007;129(3):516–31. Available from: http://dx.doi.org/10.1016/j.jbiotec.2007.01.005

128. Melchels FPW, Barradas AMC, van Blitterswijk CA, de Boer J, Feijen J, Grijpma DW. Effects of the architecture of tissue engineering scaffolds on cell seeding and culturing. Acta Biomaterialia [Internet]. 2010;6(11):4208–17. Available from: https://www.sciencedirect.com/science/article/pii/S1742706110002783

129. Matsumoto H, Moir LM, Oliver BGG, Burgess JK, Roth M, Black JL, et al. Comparison of gel contraction mediated by airway smooth muscle cells from patients with and without asthma. Thorax [Internet]. 2007 Oct 1;62(10):848 LP – 854. Available from: http://thorax.bmj.com/content/62/10/848.abstract

130. West AR, Zaman N, Cole DJ, Walker MJ, Legant WR, Boudou T, et al. Development and characterization of a 3D multicell microtissue culture model of airway smooth muscle. American Journal of Physiology - Lung Cellular and Molecular Physiology [Internet]. 2013 Jan 1;304(1):L4–16. Available from: http://www.ncbi.nlm.nih.gov/pmc/articles/PMC3543643/

131. Shahrubudin N, Lee TC, Ramlan R. An Overview on 3D Printing Technology: Technological, Materials, and Applications. Procedia Manufacturing [Internet].

2019;35:1286–96. Available from: http://www.sciencedirect.com/science/article/pii/S2351978919308169

132. Murphy S v, Atala A. 3D bioprinting of tissues and organs. Nature Biotechnology [Internet]. 2014 Aug 5;32:773. Available from: http://dx.doi.org/10.1038/nbt.2958

133. Ozbolat IT, Hospodiuk M. Current advances and future perspectives in extrusion-based bioprinting. Biomaterials [Internet]. 2016;76:321–43. Available from: http://www.sciencedirect.com/science/article/pii/S0142961215008868

134. Shafiee A, Atala A. Printing Technologies for Medical Applications. Trends in Molecular Medicine [Internet]. 2016;22(3):254–65. Available from: https://www.sciencedirect.com/science/article/pii/S1471491416000149

135. Hospodiuk M, Dey M, Sosnoski D, Ozbolat IT. The bioink: A comprehensive review on bioprintable materials. Biotechnology Advances [Internet]. 2017;35(2):217–39. Available from: http://www.sciencedirect.com/science/article/pii/S0734975016301719

136. Jungst T, Smolan W, Schacht K, Scheibel T, Groll J. Strategies and Molecular Design Criteria for 3D Printable Hydrogels. Chemical reviews. 2016 Feb;116(3):1496–539.

137. du Chatinier DN, Figler KP, Agrawal P, Liu W, Zhang YS. The potential of microfluidics-enhanced extrusion bioprinting. Biomicrofluidics [Internet]. 2021 Jul 1;15(4):041304. Available from: https://doi.org/10.1063/5.0033280

138. Beyer ST, Bsoul A, Ahmadi A, Walus K. 3D alginate constructs for tissue engineering printed using a coaxial flow focusing microfluidic device. In: 2013 Transducers & Eurosensors XXVII: The 17th International Conference on Solid-State Sensors, Actuators and Microsystems (TRANSDUCERS & EUROSENSORS XXVII). 2013. p. 1206–9.

139. Lee KY, Mooney DJ. Alginate: properties and biomedical applications. Progress in polymer science [Internet]. 2012 Jan;37(1):106–26. Available from: http://www.ncbi.nlm.nih.gov/pmc/articles/PMC3223967/

140. Andersen T, Auk-Emblem P, Dornish M. 3D Cell Culture in Alginate Hydrogels. Lornejad-Schäfer MR, Schäfer C, editors. Microarrays [Internet]. 2015 Jun 24;4(2):133–61. Available from: http://www.ncbi.nlm.nih.gov/pmc/articles/PMC4996398/

141. Pebworth M-P, Cismas SA, Asuri P. A Novel 2.5D Culture Platform to Investigate the Role of Stiffness Gradients on Adhesion-Independent Cell Migration. PLOS ONE [Internet]. 2014 Oct 13;9(10):e110453. Available from: https://doi.org/10.1371/journal.pone.0110453

142. Nunamaker EA, Otto KJ, Kipke DR. Investigation of the material properties of alginate for the development of hydrogel repair of dura mater. Journal of the mechanical behavior of biomedical materials. 2011 Jan;4(1):16–33.

143. Kaklamani G, Cheneler D, Grover LM, Adams MJ, Bowen J. Mechanical properties of alginate hydrogels manufactured using external gelation. Journal of the mechanical behavior of biomedical materials. 2014 Aug;36:135–42.

144. Freeman FE, Kelly DJ. Tuning Alginate Bioink Stiffness and Composition for Controlled Growth Factor Delivery and to Spatially Direct MSC Fate within Bioprinted Tissues. Scientific Reports [Internet]. 2017;7(1):17042. Available from: https://doi.org/10.1038/s41598-017-17286-1

145. Kang S-W, Cha B-H, Park H, Park K-S, Lee KY, Lee S-H. The Effect of Conjugating RGD into 3D Alginate Hydrogels on Adipogenic Differentiation of Human Adipose-Derived Stromal Cells. Macromolecular Bioscience [Internet]. 2011 May 12;11(5):673–9. Available from: https://doi.org/10.1002/mabi.201000479

146. Felding-Habermann B, Cheresh DA. Vitronectin and its receptors. Current Opinion in Cell Biology [Internet]. 1993;5(5):864–8. Available from: http://www.sciencedirect.com/science/article/pii/095506749390036P

147. Ruoslahti E. FIBRONECTIN AND ITS RECEPTORS. Annual Review of Biochemistry [Internet]. 1988 Jun 1;57(1):375–413. Available from: https://doi.org/10.1146/annurev.bi.57.070188.002111

148. Dong C, Lv Y. Application of Collagen Scaffold in Tissue Engineering: Recent Advances and New Perspectives. Polymers [Internet]. 2016 Feb 4;8(2):42. Available from: https://pubmed.ncbi.nlm.nih.gov/30979136

149. de Wild M, Pomp W, Koenderink GH. Thermal memory in self-assembled collagen fibril networks. Biophysical journal [Internet]. 2013 Jul 2;105(1):200–10. Available from: https://pubmed.ncbi.nlm.nih.gov/23823240

150. Visse R, Nagase H. Matrix Metalloproteinases and Tissue Inhibitors of Metalloproteinases. Circulation Research [Internet]. 2003 May 2;92(8):827–39. Available from: https://doi.org/10.1161/01.RES.0000070112.80711.3D

151. Weisel JWBT-A in PC. Fibrinogen and Fibrin. In: Fibrous Proteins: Coiled-Coils, Collagen and Elastomers [Internet]. Academic Press; 2005. p. 247–99. Available from: http://www.sciencedirect.com/science/article/pii/S0065323305700085

152. Sharma R, Smits IPM, de La Vega L, Lee C, Willerth SM. 3D Bioprinting Pluripotent Stem Cell Derived Neural Tissues Using a Novel Fibrin Bioink Containing Drug Releasing Microspheres. Frontiers in bioengineering and biotechnology [Internet]. 2020 Feb 11;8:57. Available from: https://pubmed.ncbi.nlm.nih.gov/32117936

153. de Melo BAG, Jodat YA, Cruz EM, Benincasa JC, Shin SR, Porcionatto MA. Strategies to use fibrinogen as bioink for 3D bioprinting fibrin-based soft and hard tissues. Acta Biomater [Internet]. 2020;117:60–76. Available from: http://dx.doi.org/10.1016/j.actbio.2020.09.024

154. Dickman CTD, Russo V, Thain K, Pan S, Beyer ST, Walus K, et al. Functional characterization of 3D contractile smooth muscle tissues generated using a unique microfluidic 3D bioprinting technology. The FASEB Journal [Internet]. 2020 Jan 1;34(1):1652–64. Available from: https://doi.org/10.1096/fj.201901063RR

155. Burgess JK, Ketheson A, Faiz A, Limbert Rempel KA, Oliver BG, Ward JPT, et al. Phenotype and Functional Features of Human Telomerase Reverse Transcriptase Immortalized Human Airway Smooth Muscle Cells from Asthmatic and Non-Asthmatic Donors. Scientific reports [Internet]. 2018 Jan 16;8(1):805. Available from: https://pubmed.ncbi.nlm.nih.gov/29339735

156. Gillispie GJ, Han A, Uzun-Per M, Fisher J, Mikos AG, Niazi MKK, et al. The Influence of Printing Parameters and Cell Density on Bioink Printing Outcomes. Tissue Engineering

Part A [Internet]. 2020 Sep 14;26(23–24):1349–58. Available from: https://doi.org/10.1089/ten.tea.2020.0210

157. Iskandar L, Rojo L, di Silvio L, Deb S. The effect of chelation of sodium alginate with osteogenic ions, calcium, zinc, and strontium. Journal of Biomaterials Applications [Internet]. 2019 Jul 19;34(4):573–84. Available from: https://doi.org/10.1177/0885328219861904

158. Wu Z, Su X, Xu Y, Kong B, Sun W, Mi S. Bioprinting three-dimensional cell-laden tissue constructs with controllable degradation. Scientific Reports [Internet]. 2016;6(1):24474. Available from: https://doi.org/10.1038/srep24474

159. Wang L, Stegemann JP. Extraction of high quality RNA from polysaccharide matrices using cetyltrimethylammonium bromide. Biomaterials [Internet]. 2009/12/03. 2010 Mar;31(7):1612–8. Available from: https://pubmed.ncbi.nlm.nih.gov/19962190

160. Burgess KA, Workman VL, Elsawy MA, Miller AF, Oceandy D, Saiani A. RNA extraction from self-assembling peptide hydrogels to allow qPCR analysis of encapsulated cells. PLOS ONE [Internet]. 2018 Jun 4;13(6):e0197517-. Available from: https://doi.org/10.1371/journal.pone.0197517

161. Yu C, Young S, Russo V, Amsden BG, Flynn LE. Techniques for the isolation of high-quality RNA from cells encapsulated in chitosan hydrogels. Tissue engineering Part C, Methods [Internet]. 2013/03/29. 2013 Nov;19(11):829–38. Available from: https://pubmed.ncbi.nlm.nih.gov/23448167

162. Taylor SC, Nadeau K, Abbasi M, Lachance C, Nguyen M, Fenrich J. The Ultimate qPCR Experiment: Producing Publication Quality, Reproducible Data the First Time. Trends in Biotechnology [Internet]. 2019 Jul 1;37(7):761–74. Available from: https://doi.org/10.1016/j.tibtech.2018.12.002

163. Lee JM, Ng WL, Yeong WY. Resolution and shape in bioprinting: Strategizing towards complex tissue and organ printing. Applied Physics Reviews. 2019 Mar 1;6:11307.

164. Gungor-Ozkerim PS, Inci I, Zhang YS, Khademhosseini A, Dokmeci MR. Bioinks for 3D bioprinting: an overview. Biomaterials science [Internet]. 2018 May 1;6(5):915–46. Available from: https://pubmed.ncbi.nlm.nih.gov/29492503

165. Meng W, Takeichi M. Adherens junction: molecular architecture and regulation. Cold Spring Harbor perspectives in biology [Internet]. 2009/08/05. 2009 Dec;1(6):a002899–a002899. Available from: https://pubmed.ncbi.nlm.nih.gov/20457565

166. Halayko AJ, Salari H, Ma X, Stephens NL. Markers of airway smooth muscle cell phenotype. Vol. 270, Am.J.Physiol. 1996. p. L1040--L1051.

167. Zhang J, Wehrle E, Vetsch JR, Paul GR, Rubert M, Müller R. Alginate dependent changes of physical properties in 3D bioprinted cell-laden porous scaffolds affect cell viability and cell morphology. Biomed Mater [Internet]. 2019;14(6):065009. Available from: http://dx.doi.org/10.1088/1748-605X/ab3c74

168. Rowley JA, Mooney DJ. Alginate type and RGD density control myoblast phenotype. Journal of biomedical materials research. 2002 May;60(2):217–23.

169. Yang Y, Beqaj S, Kemp P, Ariel I, Schuger L. Stretch-induced alternative splicing of serum response factor promotes bronchial myogenesis and is defective in lung hypoplasia. The Journal of clinical investigation [Internet]. 2000 Dec;106(11):1321–30. Available from: https://pubmed.ncbi.nlm.nih.gov/11104785

170. Schuliga M, Harris T, Stewart AG. Plasminogen activation by airway smooth muscle is regulated by type I collagen. Am J Respir Cell Mol Biol [Internet]. 2010;44(6):831–9. Available from: http://dx.doi.org/10.1165/rcmb.2009-0469OC

171. Panitch HB, Deoras KS, Wolfson MR, Shaffer TH. Maturational Changes in Airway Smooth Muscle Structure-Function Relationships. Pediatric Research [Internet]. 1992;31(2):151–6. Available from: https://doi.org/10.1203/00006450-199202000-00012

172. FRYER AD, JACOBY DB. Muscarinic Receptors and Control of Airway Smooth Muscle. American Journal of Respiratory and Critical Care Medicine [Internet]. 1998 Nov 1;158(supplement_2):S154–60. Available from: https://doi.org/10.1164/ajrccm.158.supplement_2.13tac120

173. Ressmeyer AR, Larsson AK, Vollmer E, Dahlèn SE, Uhlig S, Martin C. Characterisation of guinea pig precision-cut lung slices: comparison with human tissues. European Respiratory Journal [Internet]. 2006 Sep 1;28(3):603. Available from: http://erj.ersjournals.com/content/28/3/603.abstract

174. Bergner A, Sanderson MJ. Acetylcholine-induced calcium signaling and contraction of airway smooth muscle cells in lung slices. The Journal of general physiology [Internet]. 2002 Feb;119(2):187–98. Available from: https://pubmed.ncbi.nlm.nih.gov/11815668

175. Coulson FR, Jacoby DB, Fryer AD. Increased function of inhibitory neuronal M2 muscarinic receptors in trachea and ileum of diabetic rats. British journal of pharmacology [Internet]. 2002 Mar;135(6):1355–62. Available from: https://pubmed.ncbi.nlm.nih.gov/11906948

176. Fujiwara T, Itoh T, Kuriyama H. Regional differences in the mechanical properties of rabbit airway smooth muscle. British journal of pharmacology [Internet]. 1988 Jun;94(2):389–96. Available from: https://pubmed.ncbi.nlm.nih.gov/3395783

177. Schliwa M. Action of cytochalasin D on cytoskeletal networks. The Journal of cell biology [Internet]. 1982 Jan;92(1):79–91. Available from: https://pubmed.ncbi.nlm.nih.gov/7199055

178. Widdop S, Daykin K, Hall IP. Expression of Muscarinic M2 Receptors in Cultured Human Airway Smooth Muscle Cells. American Journal of Respiratory Cell and Molecular Biology [Internet]. 1993 Nov 1;9(5):541–6. Available from: https://doi.org/10.1165/ajrcmb/9.5.541

179. Kitamura N, Kaminuma O, Kobayashi N, Mori A. A Contraction Assay System Using Established Human Bronchial Smooth Muscle Cells. International Archives of Allergy and Immunology [Internet]. 2008;146(suppl(Suppl. 1):36–9. Available from: https://www.karger.com/DOI/10.1159/000126059

180. Sakota Y, Ozawa Y, Yamashita H, Tanaka H, Inagaki N. Collagen gel contraction assay using human bronchial smooth muscle cells and its application for evaluation of

inhibitory effect of formoterol. Biological & pharmaceutical bulletin. 2014;37(6):1014–20.

181. Stephens NL, Kroeger E, Mehta JA. Force-velocity characteristics of respiratory airway smooth muscle. Journal of Applied Physiology [Internet]. 1969 Jun 1;26(6):685–92. Available from: https://doi.org/10.1152/jappl.1969.26.6.685

182. Köster N, Schmiermund A, Grubelnig S, Leber J, Ehlicke F, Czermak P, et al. Single-Step RNA Extraction from Different Hydrogel-Embedded Mesenchymal Stem Cells for Quantitative Reverse Transcription–Polymerase Chain Reaction Analysis. Tissue Engineering Part C: Methods [Internet]. 2016 Apr 19;22(6):552–60. Available from: https://doi.org/10.1089/ten.tec.2015.0362

183. Zhang J, Wehrle E, Rubert M, Müller R. 3D Bioprinting of Human Tissues: Biofabrication, Bioinks, and Bioreactors. International journal of molecular sciences [Internet]. 2021 Apr 12;22(8):3971. Available from: https://pubmed.ncbi.nlm.nih.gov/33921417

184. Shi P, Laude A, Yeong WY. Investigation of cell viability and morphology in 3D bio-printed alginate constructs with tunable stiffness. Journal of Biomedical Materials Research Part A [Internet]. 2017 Apr 1;105(4):1009–18. Available from: https://doi.org/10.1002/jbm.a.35971

185. Wadsworth SJ, Pan S, Mohamed T, Beyer S. Validation of the 3DBioRingTM Airway; a 3D-Bioprinted Contractile Airway Tissue. In: A109 REMODELING AND THE MATRIX [Internet]. American Thoracic Society; 2016. p. A2837–A2837. (American Thoracic Society International Conference Abstracts). Available from: https://doi.org/10.1164/ajrccm-conference.2016.193.1_MeetingAbstracts.A2837

186. Boudou T, Legant WR, Mu A, Borochin MA, Thavandiran N, Radisic M, et al. A microfabricated platform to measure and manipulate the mechanics of engineered cardiac microtissues. Tissue engineering Part A. 2012 May;18(9–10):910–9.

187. Cheng D, Jiang C, Xu J, Liu Z, Mao X. Characteristics and applications of alginate lyases: A review. International Journal of Biological Macromolecules [Internet]. 2020;164:1304–

20. Available from: https://www.sciencedirect.com/science/article/pii/S0141813020339593

188. Lueckgen A, Garske DS, Ellinghaus A, Mooney DJ, Duda GN, Cipitria A. Enzymatically-degradable alginate hydrogels promote cell spreading and in vivo tissue infiltration. Biomaterials [Internet]. 2019;217:119294. Available from: https://www.sciencedirect.com/science/article/pii/S014296121930393X

189. Liu P, Shen H, Zhi Y, Si J, Shi J, Guo L, et al. 3D bioprinting and in vitro study of bilayered membranous construct with human cells-laden alginate/gelatin composite hydrogels. Colloids and Surfaces B: Biointerfaces [Internet]. 2019;181:1026–34. Available from: https://www.sciencedirect.com/science/article/pii/S0927776519304746

190. Pati F, Cho D-W. Bioprinting of 3D Tissue Models Using Decellularized Extracellular Matrix Bioink. Methods in molecular biology (Clifton, NJ). 2017;1612:381–90.

191. Kim JH, Kim I, Seol Y-J, Ko IK, Yoo JJ, Atala A, et al. Neural cell integration into 3D bioprinted skeletal muscle constructs accelerates restoration of muscle function. Nature Communications [Internet]. 2020;11(1):1025. Available from: https://doi.org/10.1038/s41467-020-14930-9

192. Berg J, Hiller T, Kissner MS, Qazi TH, Duda GN, Hocke AC, et al. Optimization of cell-laden bioinks for 3D bioprinting and efficient infection with influenza A virus. Scientific Reports [Internet]. 2018;8(1):13877. Available from: https://doi.org/10.1038/s41598-018-31880-x

193. Mestre R, Patiño T, Barceló X, Anand S, Pérez-Jiménez A, Sánchez S. Force Modulation and Adaptability of 3D-Bioprinted Biological Actuators Based on Skeletal Muscle Tissue. Advanced Materials Technologies [Internet]. 2019 Feb 1;4(2):1800631. Available from: https://doi.org/10.1002/admt.201800631

194. Icha J, Weber M, Waters JC, Norden C. Phototoxicity in live fluorescence microscopy, and how to avoid it. BioEssays [Internet]. 2017 Aug 1;39(8):1700003. Available from: https://doi.org/10.1002/bies.201700003

195. Aarstad O, Heggset EB, Pedersen IS, Bjørnøy SH, Syverud K, Strand BL. Mechanical Properties of Composite Hydrogels of Alginate and Cellulose Nanofibrils. Polymers [Internet]. 2017 Aug 19;9(8):378. Available from: https://pubmed.ncbi.nlm.nih.gov/30971055

196. Patino C. Alginate Hydrogel as a Three-dimensional Extracellular Matrix for In Vitro Models of Development. 2013 Nov 1;

197. Woodruff PG. Gene expression in asthmatic airway smooth muscle. Proceedings of the American Thoracic Society [Internet]. 2008 Jan 1;5(1):113–8. Available from: https://pubmed.ncbi.nlm.nih.gov/18094093

198. Heo J, Koh RH, Shim W, Kim HD, Yim H-G, Hwang NS. Riboflavin-induced photo-crosslinking of collagen hydrogel and its application in meniscus tissue engineering. Drug delivery and translational research [Internet]. 2016;6(2):148–58. Available from: http://europepmc.org/abstract/MED/25809935

199. Girton TS, Oegema TR, Tranquillo RT. Exploiting glycation to stiffen and strengthen tissue equivalents for tissue engineering. J Biomed Mater Res [Internet]. 1999;46(1):87–92. Available from: http://dx.doi.org/10.1002/(sici)1097-4636(199907)46:1<87::aid-jbm10>3.0.co

200. Edmondson R, Broglie JJ, Adcock AF, Yang L. Three-dimensional cell culture systems and their applications in drug discovery and cell-based biosensors. Assay and drug development technologies [Internet]. 2014 May;12(4):207–18. Available from: https://pubmed.ncbi.nlm.nih.gov/24831787

Appendix A: Statistical Power Analysis

Post hoc balanced one-way analysis of variance power calculations were performed using the ‘pwr’ package 1.3-0 for R studio (version 3.6.2).

Balanced one-way analysis of variance power calculation:

k = 4

n = 10

f = 0.5513278

significance level = 0.05

power = 0.8

Where k is the number of groups and n is the common sample size in each group.

For a one-way ANOVA, effect size is measured by the f value, which is calculated using:

$$\boldsymbol{f = \sqrt{\frac{\sum_{i=1}^{k} p_i * (\mu_i - \mu)^2}{\sigma^2}}}$$

Where $p_i = n_i / N$

n_i = number of observations in group i

N = total number of observations

μ_i = mean of group i

μ = population mean

σ^2 = error variance within groups

Appendix B: RNA isolation methods

Purelink	TRIzol	CTAB	GeneJET	Plant RNA
1. Culture media was discarded and 600µl of freshly prepared lysis buffer supplemented with 1% β-ME was added to tissues	1. ASM tissues were lysed by adding 1mL of Trizol reagent. This was homogenized by mixing up and down and incubated for 5 minutes at room temperature	1. 1 mL of the CTAB buffer was added to each sample, this was mixed thoroughly and incubated for 5 minutes at 65°C	1. After removing culture media, 500µl of Plant RNA lysis solution supplemented with 2% DTT was added to the tissues	1. RNase free microcentrifuges were cooled in ice before adding ASM tissues and 0.5 mL cold (4°C) Plant RNA Reagent
2. Lysates were transferred to RNase free tubes and homogenized by vigorous pipetting	2. 200µl of chloroform per mL of Trizol reagent was added to lysates. Mixed vigorously and incubated at room temperature for 3 minutes	2. An equal volume of 24:1 chloroform-isoamyl alcohol mixture was added and vortexed thoroughly. This was centrifuged at room temperature for 5 minutes at 15,000 x g	2. Lysates were incubated for 5 minutes at 56°C, after which they were spun at 20,000 x g for 5 minutes	2. Samples were mixed by briefly vortexing and incubated for 5 minutes at room temperature, after which they were centrifuged for 12,000 x g for 2 minutes
3. One volume of 70% ethanol was added to each volume of cell homogenate and mixed thoroughly to	3. Colorless upper phase was mixed with an equal volume of 70% ethanol then mixed thoroughly by vortexing	3. The upper aqueous phase was mixed with an equal volume of 24:1 chloroform-isoamyl alcohol,	3. The supernatant was collected and added to 250µl of 96% Ethanol, this was mixed	3. 100µl of 5M NaCl and 300µl of chloroform was added to the supernatant. This was mixed

disperse visible precipitates		mixed thoroughly and centrifuged for 15,000 x g for 5 minutes	thoroughly by vortexing	thoroughly by inverting the tube
4. Samples were centrifuged at 12,000 x g for 15 seconds at room temperature	4. Samples were centrifuged for 12,000 x g for 15 seconds at room temperature and steps 5 -7 in the Purelink column was repeated.	4. An equal volume of 99.9% isopropanol was added and centrifuged as above	4. The mixture was transferred to a purification column inserted in a collection tube and centrifuged for 1 min at 12,000 × g	4. Samples were centrifuged for 12,000 x g for 10 minutes at 4ºC and the aqueous upper phase was mixed with an equal volume of isopropyl alcohol
5. Flow-through was discarded and 700µl of wash buffer 1 was added and centrifuged as above, after which 500 µl of wash buffer 2 was added and centrifuged twice		5. Supernatant was discarded, and pellet was resuspended in 50µl RNase free water	5. Flow-through was discarded and 700µl of wash buffer 1 was added to the purification column and centrifuged at 12,000 x g for 1 minute	5. After incubating for 10 minutes at room temperature, samples were centrifuged for another 10 minutes at 12,000 x g at 4ºC
6. The spin cartridge membrane was dried by centrifuging for 2 minutes at 12,000 x g		6. Samples were cleaned up using the protocol in the Purelink column	6. After discarding flow-through, 500µl of wash buffer 2 was added and centrifuged as above, this step was repeated twice, and the spin membrane was dried by	6. Supernatant was discarded and 1mL of 75% Ethanol was added to the pellet, this was centrifuged for 1 minute at 12,000 x g at room temperature

			centrifuging at 12,000 x g for 2 min	
7. 50µl of RNase free water was added to the membrane and was spun for 12,000 x g for 2 minutes to elute RNA. RNA was stored in -80^{o}C until use.			7. 50µl of RNase free water was added to the membrane which was spun for 12,000 x g for 2 minutes to elute RNA. RNA was stored in -80^{o}C until use.	7. Supernatant was discarded and 30µl of RNase free water was added to the pellet. Mixed thoroughly and stored in -80^{o}C until use.

Table A. RNA isolation methods. Methods were adapted from the manufacturer's recommendations.